BOSTON UNIVERSITY

GRADUATE SCHOOL OF ARTS AND SCIENCES

Dissertation

A SEARCH FOR TECHNICOLOR AT THE LARGE HADRON COLLIDER

by

JEREMY R. LOVE

B.S., Carnegie Mellon University, 2004
M.A., Boston University, 2008

Submitted in partial fulfillment of the

requirements for the degree of

Doctor of Philosophy

2012

Approved by

First Reader

John M. Butler, Ph.D.
Professor of Physics

Second Reader

Kevin M. Black, Ph.D.
Assistant Professor of Physics

Right now, theorists are in the driver's seat, and will be for the next 30 years. But then, we have no idea what comes next, and we'll absolutely need experimental guidance.

Martinus J. G. Veltman (1980)

If it were easy everyone would do it.

John M. Butler

Acknowledgments

This thesis is not the work of an isolated individual acting alone, but instead a culmination of the efforts of many teachers and collaborators whose contributions I would like to humbly recognize. I would like to thank my adviser John Butler for giving me the unique and wonderful opportunity to work on such an exciting and challenging project, and for all his assistance and patience in helping me achieve my goals. To Ken Lane I would like to say thank you for helping me and I'm sorry. Thank you to everyone in the Boston University Physics Department for their support during my time as a Graduate Student.

I would also like to thank my Boston University ATLAS colleagues specifically Steve Ahlen, Jim Shank, Saul Youssef, Kevin Black, Rob Harrington, Zhen Yan, Nigel Nation, Marta Lewandowska, Mike Kruskal, Clare Bernard, and Alex Long for all their help. While on ATLAS I was privileged to work along side and be helped by many talented collaborators. Thank you to the entire ATLAS Collaboration. I would also like to thank a few individuals for their collaboration and considerable contributions to my training Frank Taylor, Jack Fowler, Teisheng Dai, Agostino Lanza, Tetiana Hryn'ova, and Ludovica Aperio Bella.

Before my arrival at Boston University two individuals played an enormous role in setting me on this path Prof. Kunal Ghosh and Patricia Somers without whose support I never would have been in this position. Nicole, thank you for the motivation to actually write and finish this thesis. Finally, I would like to thank my parents and family for their continued support throughout my long academic career.

Thank you all.

A SEARCH FOR TECHNICOLOR AT THE LARGE HADRON COLLIDER

(Order No.)

JEREMY R. LOVE

Boston University Graduate School of Arts and Sciences, 2012

Major Professor: John M. Butler, Professor of Physics

ABSTRACT

The Standard Model of particle physics provides an accurate description of all experimental data to date. The only unobserved piece of the Standard Model is the Higgs boson, a consequence of the spontaneous breaking of electroweak symmetry by the Higgs mechanism. An alternative to the Higgs mechanism is proposed by Technicolor theories which break electroweak symmetry dynamically through a new force. Technicolor predicts many new particles, called Technihadrons, that could be observed by experiments at hadron colliders. This thesis presents a search for two of the lightest Technihadrons, the ρ_T and ω_T.

The Low-Scale Technicolor model predicts the phenomenology of these new states. The ρ_T and ω_T are produced through $q\bar{q}$ annihilation and couple to Standard Model fermions through the Drell-Yan process, which can result in the dimuon final state. The ρ_T and ω_T preferentially decay to the π_T and a Standard Model gauge boson if kinematically allowed. Changing the mass of the π_T relative to that of the ρ_T and ω_T affects the cross section times branching fraction to dimuons. The ρ_T and ω_T are expected to have masses below about 1 TeV.

The Large Hadron Collider (LHC) at CERN outside of Geneva, Switzerland, produces proton-proton collisions with a center of mass energy of 7 TeV. A general purpose high energy physics detector ATLAS has been used in this analysis to search for Technihadrons decaying to two muons. We use the ATLAS detector to reconstruct the tracks of muons with high transverse momentum coming from these proton-proton collisions.

The dimuon invariant mass spectrum is analyzed above 130 GeV to test the consistency of the observed data with the Standard Model prediction. We observe excellent agreement between our data and the background only hypothesis, and proceed to set limits on the cross section times branching ratio of the ρ_T and ω_T as a function of their mass using the Low-Scale Technicolor model. We combine the dielectron and dimuon channels to exclude masses of the ρ_T and ω_T between 130 GeV - 480 GeV at 95% Confidence Level for masses of the π_T between 50 GeV - 480 GeV. In addition for the parameter choice of m(π_T) = m(ρ_T/ω_T) - 100 GeV, 95% Confidence Level limits are set excluding masses of the ρ_T and ω_T below 470 GeV. This analysis represents the current world's best limit on this model.

Contents

List of Tables

List of Figures

List of Abbreviations

ADC	....	Analogue to digital converter.
ATLAS	....	A Toroidal LHC ApparatuS.
ASD	....	Analog Shaper Discriminant.
BC	....	Bunch-Crossing.
BCID	....	Bunch-Crossing Identifier.
CERN	....	European Laboratory for Particle Physics.
CL	....	Confidence Level.
CSC	....	Cathode Strip Chamber.
CSM	....	Chamber Service Module.
CTP	....	Central Trigger Processor.
DAQ	....	Data Acquisition System.
DCS	....	Detector Control System.
HCal	....	Hadronic Calorimeter.
HEP	....	High Energy physics.
ID	....	Inner Detector.
IP	....	Interaction Point.
L1	....	Level-1 Trigger System.
L2	....	Level-2 Trigger System.
LAr	....	Liquid Argon Calorimeters.
LHC	....	Large Hadron Collider.
LINAC	....	Linear Accelerator.
LVL1	....	Level-1 Trigger System.
LVL2	....	Level-2 Trigger System.
MC	....	Monte Carlo simulation.
MDT	....	Monitored Drift Tube.
PDF	....	Parton Distribution Function.
PS	....	Proton Synchrotron.
PV	....	Primary Vertex.
QCD	....	Quantumchromo Dynamics.
RMS	....	Root Mean Square.
RoI	....	Region of Interest.
RPC	....	Resistive Plate Chamber.
SCT	....	Semiconductor Tracking detector.

SM	....	Standard Model.
SPS	....	Super Proton Synchrotron.
TDC	....	Time to Digital Converter.
TGC	....	Thin Gap Chamber.
TileCal	....	Tile Calorimeter.
TLA	....	Three-letter acronym.

Chapter 1

Introduction

The twentieth century saw an explosion in the discovery of new sub-atomic particles by experimental physicists. Theoretical particle physicists set about explaining the nature of these new particles and their interactions. In 1961 theorists developed [19, 20], what Murray Gell-man dubbed, the “Eightfold way” which led to the quark model. The mid-1960’s saw great advances in theoretical physics with Glashow, Weinberg, and Salam formulating our current model of the Electroweak Theory [21–23]. In the late sixties and early seventies experiments carried out at SLAC and CERN probed the structure of the proton and showed that the quark model and quark confinement were in fact correct. In 1974 the “November Revolution” was spawned by two experiments, who simultaneously claimed discovery of a new particle known as the J/ψ [24, 25], a bound state of the charm and anti-charm quarks. At around the same time the theoretical discovery of the asymptotic freedom of quarks [26, 27] helped to solve a theoretical problem pertaining to Quantum chromodynamics (QCD). In the late seventies the theory of Electroweak interactions, QCD, and the flavor structure of the quarks and leptons were combined to form the Standard Model of particle physics.

Experiments at CERN in the early eighties observed the predicted $W^{\pm}$ and Z bosons [28,29] and in the mid-nineties the discovery of the top quark at Fermilab [30, 31]. In the 30 years since the Standard Model was initially formulated it has been tested repeatedly and no significant discrepancy with experimental results has been observed. But there remains one final piece to the Standard Model that has not yet been observed, the mechanism by which the $W^{\pm}$ and Z bosons obtain mass and break Electroweak symmetry. The Higgs Mechanism [32] breaks Electroweak symmetry, mediated by the Higgs boson in the Standard Model. However, this predicted spin-0 Higgs boson has yet to be observed experimentally. Despite the unprecedented success of the Standard Model, many high energy theorists are not satisfied with some of the unaddressed questions in the Standard Model.

In the intervening decades High Energy theorists have proposed many extensions to the Standard Model, one of which is technicolor. Technicolor theories predict a new strong QCD-like force that is responsible for electroweak symmetry breaking. With this new force come new bound states called technihadrons. The lightest spin-1 technihadrons are the ρ_T and ω_T which can decay to Standard Model fermion pairs such as muons. This is the same signal that started the "November Revolution" by discovery of the J/ψ, and years later discovered the Z boson.

With the start up of the Large Hadron Collider (LHC) a new accelerator at the European Center for Nuclear Research (CERN), a new energy frontier is accessible for testing. Previously, at CERN, Fermilab, and Brookhaven National Lab hadron colliders have been used to discover new unexpected physics. Like these previous accelerators the LHC will collide particles with energies high enough to create new resonances. If they are not observed in the data, limits can be set on the theoretical prediction for them.

In Chapter 2 of this thesis, a brief theoretical discussion is presented. The elements of the Standard Model are described in detail as well as the structure of the fundamental interactions. Special emphasis is placed on the mechanism for Electroweak Symmetry breaking in the Standard Model, describing both the Higgs boson and in its absence Electroweak Symmetry breaking via QCD. Additionally, the beyond the standard model explanation provided by the new dynamics of technicolor is discussed, as well as an overview of the phenomenology of the theory and current experimental limits.

In Chapter 3 and Chapter 4 the experimental apparatus is presented. In Chapter 3 accelerator physics and specifically the LHC accelerator is discussed. The advantages over previous accelerators as well as the unique challenges are presented. The LHC not only represents the energy frontier but also the intensity frontier for hadron colliders, and with this new machine come new challenges. In Chapter 4 the layout and description of the ATLAS detector and sub-systems, and its design parameters are presented. Special emphasis is paid to the tracking sub-detectors used in the search for technihadrons.

Chapter 5 presents a look at the Muon Spectrometer of the ATLAS detector. The Muon Spectrometer was designed to achieve 10% resolution on a 1 TeV p_T muon. This figure of merit for the performance along with the capability to handle the high rate drove the spectrometer layout, detector technology, and chamber design. The focus of this chapter is the Monitored Drift Tubes, the precision measurement chambers that are installed over the majority of the detector coverage. There is a discussion of the challenges of such wire proportional chambers. In Chapter 6 the reconstruction of detector data to physics objects is discussed, as well as the instrumental backgrounds and challenges to dimuon analyses. The factors that affect the resolution of the muon p_T are presented and what steps were taken to counter them.

Chapter 7 presents the search for technihadrons, with descriptions of Monte Carlo modeling of physics backgrounds and signal processes, event selection, estimation of the systematic uncertainties, statistical methods used, and the results in the context of the Low-scale technicolor model. Chapter 8 presents the conclusions and future plans and improvements for this analysis.

This thesis presents all masses, momentums, and energies in the same units of eV unless otherwise noted. This choice is a standard convention and a consequence of natural units, where $\hbar = c = 1$, which are used throughout, unless otherwise noted.

Chapter 2

Technicolor Theory

2.1 The Standard Model of Particle Physics

The Standard Model(SM) of particle physics is an effective quantum field theory of interactions between spin-$\frac{1}{2}$ matter fermions and unit spin gauge bosons.[1] The matter spin-$\frac{1}{2}$ fermions are grouped into two categories, quarks and leptons, the classification is based on their charges. The Standard Model uses a common framework to describe three fundamental forces based on the symmetry group $SU(3)_C \times SU(2)_L \times U(1)_Y$, each of these symmetries correspond to one of the fundamental forces [34]. The three forces described by the Standard Model are the strong nuclear force or Quantum chromodynamics(QCD), the weak nuclear force, and the electromagnetic force.

Quantum chromodynamics is mediated by the eight gluons [35] and is represented by the symmetry group $SU(3)_C$. Gluons (g) are massless and electrically neutral but carry color charge and are strongly self-interacting. At low energy the strong coupling strength makes QCD non-perturbative and calculations difficult. At higher energies QCD becomes perturbative due to the coupling getting weaker.

The weak nuclear force and electromagnetic force are unified, at high energies, into the Electroweak Force (EW) and represented by the symmetry group $SU(2)_L \times U(1)_Y$ [21–23]. The Electroweak force is mediated by the massless photon (γ), and

[1]Spin is the intrinsic quantum number explaining the quantization of the magnetic moment proposed by Pauli in 1925 [33].

the massive W and Z bosons ($W^{\pm}$ and Z). Above the masses of the W and Z the fields are unified and viewed as one, at lower energies the symmetry is broken and they can be treated as two separate forces.

2.2 Matter Fermions

The twelve matter particles of the Standard Model are classified as quarks and leptons. The leptons are charged under the electroweak force half with unit electrical charge and half, the neutrinos, electrically neutral. The six quarks[2] are charged under QCD, and the electroweak force. But the quarks are never observed "bare", only as constituents of bound state composite particles. Their fundamental masses must be inferred from the observable particles. These particles are called hadrons, with two constituent, quark anti-quark, particles called mesons, and three-quark particles called baryons. Both mesons and baryons have unit electrical charge, so quarks must have fractional charges. The charges and masses of the twelve fermions are summarized in Table 2.1 [1].

Table 2.1: The known SM fermions sorted by electrical charge and generation [1]. Their masses are in GeV unless otherwise noted.

Quarks				**Leptons**			
$Q = 2/3$		$Q = -1/3$		$Q = 0$		$Q = -1$	
u	0.0015-0.004	d	0.004-0.008	ν_e	< eV	e	0.000511
c	1.15-1.35	s	0.80-0.130	ν_μ	< 190 keV	μ	0.106
t	174.3 ± 5.1	b	4.1-4.4	ν_τ	< 18.2 MeV	τ	1.77

Both the quarks and leptons are organized into three "generations" of particles that repeat with identical quantum numbers save for masses which increase.[3] The

[2] up(u), down(d), charm(c), strange(s), top(t), and bottom or beauty(b).

[3] This structure is known to be true for quarks, and non-neutrino leptons. In the neutrino sector how the flavor and mass eigenstates are arranged has not been determined.

three generations can then be represented as:

$$\begin{pmatrix} \nu_e \\ e^- \end{pmatrix}_L, e^-_R, \begin{pmatrix} u \\ d \end{pmatrix}_L, u_R, d_R$$
$$\begin{pmatrix} \nu_\mu \\ \mu^- \end{pmatrix}_L, \mu^-_R, \begin{pmatrix} c \\ s \end{pmatrix}_L, c_R, s_R \quad (2.1)$$
$$\begin{pmatrix} \nu_\tau \\ \tau^- \end{pmatrix}_L, \tau^-_R, \begin{pmatrix} t \\ b \end{pmatrix}_L, t_R, b_R$$

Here there is a left handed doublet and a right handed singlet for each generation, and handedness refers to the particle's chirality. Additionally each fermion has a corresponding anti-particle with the same mass and opposite charge.

2.3 The Standard Model Interactions

The Standard Model Lagrangian can be separated into components dealing with the interactions and that dealing with the masses:

$$\mathcal{L}_{SM} = \mathcal{L}_{EW} + \mathcal{L}_{QCD} + \mathcal{L}_{Mass} \quad (2.2)$$

where the $\mathcal{L}_{EW}$ and $\mathcal{L}_{QCD}$ are the Lagrangian of the interactions and have been separated from the mass terms and associated mechanism $\mathcal{L}_{Mass}$. The interaction Lagrangians describe coupling of the matter fermions with the force currents of the bosons. Here the mass Lagrangian is kept separate to make a distinction between what has been experimentally observed and what has not, and to allow for discussion of different methods of Electroweak symmetry breaking, and dynamic mass generation.

2.3.1 Quantum Chromodynamics

The QCD Lagrangian can be written as:

$$\mathcal{L}_{QCD} = \sum_{q} \left[\bar{q} \left(i\gamma^{\mu}\partial_{\mu} - m \right) q - g_s \left(\bar{q}\gamma^{\mu}T_a q \right) G^a_{\mu} \right] - \frac{1}{4} G^a_{\mu\nu} G^{\mu\nu}_a \tag{2.3}$$

where q and $\bar{q}$ are the quark fields, γ are Dirac matrices, g_s is the color charge, T_a are the eight generator matrices for the non-abelian $SU(3)_C$, G^a_{μ} are the gluon fields, and the indices μ run over the four coordinates, and a over the eight generators of the $SU(3)_c$ group that defines the QCD interactions. The three terms in this equation are the kinetic term for the quarks, the quark gluon interaction term, and the gluon kinetic term. The $SU(3)_c$ group is non-abelian because the generators T_a do not all commute with each other, meaning:

$$[T_a, T_b] = T_a T_b - T_b T_a = i f_{abc} T_c \tag{2.4}$$

where f_{abc} are real constants known as the structure constants of the group. The field strength tensor is then defined as:

$$G^a_{\mu\nu} = \partial_{\mu} G^a_{\nu} - \partial_{\nu} G^a_{\mu} - g f_{abc} G^b_{\mu} G^c_{\nu} \tag{2.5}$$

and under a non-abelian gauge transformation the eight gluon fields transform as:

$$G^a_{\mu} \rightarrow G^a_{\mu} - \frac{1}{g}\partial_{\mu}\alpha^a - f_{abc}\alpha^b G^c_{\mu} \tag{2.6}$$

in order to leave $\mathcal{L}_{QCD}$ invariant, where α^a is a gauge function.

In Eqn. 2.3 the charge g_s is proportional to the coupling of QCD α_s by:

$$\alpha_s = \frac{g_s^2}{4\pi}. \tag{2.7}$$

The coupling constant α_s of QCD runs with energy and is given by:

$$\alpha_s\left(\mathsf{Q}^2\right) = \frac{\alpha_s\left(\mu^2\right)}{1 + \frac{\alpha_s(\mu^2)}{12\pi}\left(33 - 2n_f\right)\log\left(\frac{\mathsf{Q}^2}{\mu^2}\right)} \tag{2.8}$$

where Q is the energy of the interaction, μ is the renormalization scale, and n_f is the number of quark flavors.[4] As the energy of the interaction (Q) grows large $\alpha_s\left(\mathsf{Q}^2\right)$ decreases and becomes small for short-distance interactions this is called asymptotic freedom [26, 27]. At these short distances the small coupling constant allows for a perturbative description of QCD interactions in terms of quasi-free quarks and gluons. However, as Q decreases the effective coupling increases and can be approximated by:

$$\alpha_s\left(\mathsf{Q}^2\right) = \frac{12\pi}{\left(33 - 2n_f\right)\log\left(\frac{\mathsf{Q}^2}{\Lambda_{QCD}^2}\right)} \tag{2.9}$$

here Λ_{QCD}, the QCD scale, is the energy boundary between quasi-free quarks and gluons and the bound states of so called hadrons. Hadrons made up of a quark and anti-quark are called mesons, and bound states of three quarks or three anti-quarks are called baryons. There is no theoretical prediction for this scale Λ_{QCD} and it must be determined experimentally. The QCD scale Λ_{QCD} is of the order of the light hadron masses, about a few hundred MeV [1].

Due to the non-perturbative nature of QCD different techniques have been developed to allow calculations to be performed, lattice QCD has made calculations at low energy possible, and at high energy Parton Distribution Functions (PDFs) are used to parameterize the quark content of hadrons. PDFs parameterize the fraction of momentum carried by each constituent of a particle. These PDFs are necessary for generating Monte Carlo(MC), and making predictions of cross sections and kinematic distributions at hadron colliders. Figure 2·1 shows the fraction of momentum

[4] If the number of quark flavors is greater than 16 the QCD coupling will change sign and would then have the same sign coupling as α_{EW}.

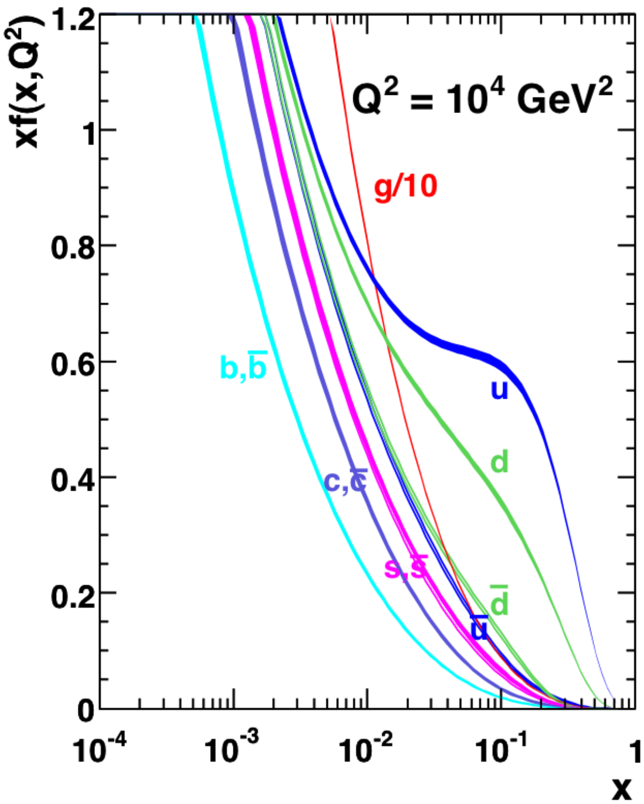

Figure 2·1: The MSTW NLO parton distribution functions within a proton evaluated at 10 TeV, from Ref [7]. An important note is that the gluon curve in red is divided by 10.

x, carried by the different quarks and gluons in a proton at LHC energies as calculated by the MSTW2008 PDF set [7]. The red gluon curve in the distribution is divided by 10 and dominates the partonic luminosity at low momentum fraction.

2.3.2 Electroweak Force

The $\mathcal{L}_{EW}$ describing the interactions of fermions and the electroweak gauge bosons can be written as:

$$\begin{aligned}\mathcal{L}_{EW} = & - \frac{1}{4}W_{\mu\nu} \cdot W^{\mu\nu} - \frac{1}{4}B_{\mu\nu}B^{\mu\nu} \\ & + \bar{L}\gamma^{\mu}\left(i\partial_{\mu} - g\frac{1}{2}\tau \cdot W_{\mu} - g'\frac{Y}{2}B_{\mu}\right)L \\ & + \bar{R}\gamma^{\mu}\left(i\partial_{\mu} - g'\frac{Y}{2}B_{\mu}\right)R\end{aligned} \tag{2.10}$$

where L and R are the left and right handed fermion fields, g and g' are the couplings, τ are the generators of the $SU(2)_L$ group, and $W^a_{\mu\nu}$ and $B_{\mu\nu}$ are the gauge field strength tensors. The field strength tensors are defined as:

$$\begin{aligned}W^a_{\mu\nu} &= \partial_\mu W^a_\nu - \partial_\nu W^a_\mu + g\epsilon^{abc}W^b_\mu W^c_\nu \\ B_{\mu\nu} &= \partial_\mu B_\nu - \partial_\nu B_\mu\end{aligned} \tag{2.11}$$

$\mathcal{L}_{EW}$ of Equation 2.10 is invariant under an $SU(2)_L \times U(1)_Y$ transformation as the W^a_μ and B_μ fields transform:

$$\begin{aligned}W^a_\mu &\rightarrow W^a_\mu + \partial_\mu\theta^a(x) + g\epsilon^{abc}\theta^b W^c_\mu \\ B_\mu &\rightarrow B_\mu - \partial_\mu\alpha(x)\end{aligned} \tag{2.12}$$

and the physical $W^{\pm}$, Z, and γ fields are expressed as linear combinations using the weak mixing angle θ_W:

$$\begin{aligned} W^{\pm}_{\mu} &= \frac{1}{\sqrt{2}}\left(W^1_{\mu} \mp iW^2_{\mu}\right) \\ Z_{\mu} &= \cos(\theta_W)W^3_{\mu} - \sin(\theta_W)B_{\mu} \\ A_{\mu} &= \sin(\theta_W)W^3_{\mu} + \cos(\theta_W)B_{\mu} \end{aligned} \tag{2.13}$$

the coupling of the L and R to these particle fields in Equation 2.10 produce the electroweak interactions.

2.3.3 Electroweak Charges

At high energy the electroweak force is the unification of two separate symmetry groups there are different charges for the two forces with the couplings of:

$$Q = T_3 + Y \tag{2.14}$$

where Q is the electric charge, Y is the hypercharge, and T_3 is third component of the weak isospin. The value of these charges for the first generation of matter fermions are listed in Table 2.2 [1].

2.4 Electroweak Symmetry Breaking

Since the SM Lagrangian is invariant under a local $SU(2)_L \times U(1)_Y$ gauge transformation explicit mass terms for the gauge bosons are forbidden. Explicit mass terms break this gauge invariance and make the theory non-renormalizable. Since the $W^{\pm}$ and Z have masses a new non-explicit feature must be introduced to give rise to mass terms without simply adding them by hand [34]. There are many theoretical models to generate mass terms for the SM gauge fields and fermions and in the following sections Electroweak Symmetry Breaking from the Higgs Mechanism, QCD,

Table 2.2: Quantum numbers for the first generation fermions. The second and third generation fermions have the same quantum numbers as their corresponding first generation particle listed here [1].

Fermion	T	T_3	Q	Y
ν_L	$\frac{1}{2}$	$\frac{1}{2}$	0	-$\frac{1}{2}$
e_L	$\frac{1}{2}$	-$\frac{1}{2}$	-1	-$\frac{1}{2}$
e_R	0	0	-1	-1
u_L	$\frac{1}{2}$	$\frac{1}{2}$	$\frac{2}{3}$	$\frac{1}{6}$
d_L	$\frac{1}{2}$	-$\frac{1}{2}$	-$\frac{1}{3}$	$\frac{1}{6}$
u_R	0	0	$\frac{2}{3}$	$\frac{2}{3}$
d_R	0	0	-$\frac{1}{3}$	-$\frac{1}{3}$

and technicolor will be discussed.

2.4.1 Higgs Mechanism

The mechanism for electroweak symmetry breaking is known as the Higgs mechanism [32]. In the Standard Model the Higgs mechanism is implemented by addition of a new doublet of complex scalar fields:

$$\phi = \begin{pmatrix} \phi^+ \\ \phi^0 \end{pmatrix} \tag{2.15}$$

is introduced along with a potential of the form:

$$V = \lambda \left(\phi^\dagger \phi - \frac{1}{2} v^2 \right)^2 \tag{2.16}$$

where λ is the scalar self coupling. This self coupling gives rise to a non-zero vacuum expectation value, $v \approx 246\,\text{GeV}$ [1], for the Higgs field, which through couplings to the SM gauge fields, gives masses to the $W^\pm$ and Z but not the γ. To accomplish

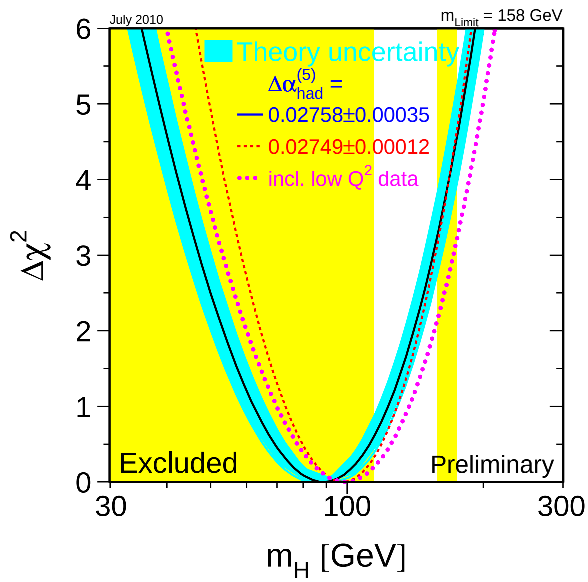

Figure 2·2: Using experimental measurements which depend on the mass of the Higgs boson a likelihood (black line) can be calculated to determine the value of the most probable Higgs mass given the observed experimental data, from Ref [8]. Excluded regions from direct searches are shown in yellow.

this the representation of the Higgs field is chosen such that:

$$< \phi_0 >= \frac{1}{\sqrt{2}} \begin{pmatrix} 0 \\ v \end{pmatrix} \tag{2.17}$$

This new Higgs field is shifted by its vacuum expectation value, and the remaining real field ϕ is interpreted as the spin-0 Higgs boson. By expanding $V(\phi)$ in Eqn 2.16 the mass of the Higgs boson can be seen to be:

$$m_h^2 = 2v^2\lambda. \tag{2.18}$$

Despite the success of the Standard Model in predicting experimental results the Higgs boson has not been observed. In fact the most probable value, as determined by a fit to other experimental results, has been ruled out by direct searches [8]. As the Standard Model is in a sense over-constrained Figure 2·2 shows the change in χ^2 of a fit to experimental observables whose value depend on the Higgs mass as a function of the Higgs mass. The yellow region has been excluded by direct searches, the black line shows the most probably value, which has already been ruled out.

Once electroweak symmetry has been broken by the Higgs vacuum expectation value the full $\mathcal{L}_{EW} + \mathcal{L}_{Mass}$ can be written as:

$$\begin{aligned}
\mathcal{L}_{EW} + \mathcal{L}_{Mass} = & - \frac{1}{4} W_{\mu\nu} \cdot W^{\mu\nu} - \frac{1}{4} B_{\mu\nu} B^{\mu\nu} \\
& + \bar{L}\gamma^{\mu} \left(i\partial_{\mu} - g\frac{1}{2}\tau \cdot W_{\mu} - g'\frac{Y}{2} B_{\mu} \right) L \\
& + \bar{R}\gamma^{\mu} \left(i\partial_{\mu} - g'\frac{Y}{2} B_{\mu} \right) R \\
& + \left| \left(i\partial_{\mu} - g\frac{1}{2}\tau \cdot W_{\mu} - g'\frac{Y}{2} B_{\mu} \right) \phi \right|^2 - \lambda \left(\phi^{\dagger}\phi - \frac{1}{2} v^2 \right)^2 \\
& - \left(G_1 \bar{L}\phi R + G_2 \bar{L}\phi_c R + \text{hermitian conjugate} \right)
\end{aligned} \tag{2.19}$$

Here terms on the last line show that coupling the left and right handed fermion fields to the Higgs field ϕ generates mass terms such as $G_1\bar{L}\phi R$ for the Standard Model fermions.

2.4.2 Quantum Chromodynamics

Even, without the Higgs mechanism Electroweak symmetry would still be broken by the pions of QCD. Since the massless gluons have a self coupling there is a vacuum polarization that causes the u and d quarks to form stable condensates:

$$< \bar{u}u > = < \bar{d}d > \neq 0 \tag{2.20}$$

in the limit where both u and d are massless and degenerate. Since the quarks are arranged in a left handed doublet and right handed singlets they couple to the gauge fields in the same way as the Higgs field to break the electroweak interactions down to electromagnetism in the same way, giving mass to the $W^{\pm}$ and Z but not the γ. The Nambu-Goldstone bosons [36] produced by breaking this symmetry are the pions of QCD. Three of these pions are "eaten" and become the longitudinal components of the $W^{\pm}$ and Z giving these bosons mass. These masses are

$$\begin{aligned} M_{W^{\pm}} &= \frac{g f_{\pi}}{2} \\ M_{Z} &= \frac{g f_{\pi}}{2\cos(\theta_W)} \\ \frac{M_{W^{\pm}}}{M_Z} &= \cos(\theta_W) \end{aligned} \tag{2.21}$$

where g the EW coupling is ~0.65 and f_{π} is the pion decay constant equal to 93 MeV, and θ_W the weak mixing angle [21]. The masses predicted for the $W^{\pm}$ and Z bosons would be 30 and 34 MeV [37]. This is $\sim 2500\times$ lower than their experimentally measured values of 80 GeV and 91 GeV [1]. However, the ratio of their masses $\cos(\theta_W) = 0.88$ is correct [1, 37]. In order to correctly predict $M_{W^{\pm}}$ and M_Z the f_{π} would need to be ~ 250 GeV [37].

2.5 Technicolor Theories

Technicolor theories are based on a new QCD-like force that dynamically breaks Electroweak symmetry [37]. This new force comes with new massless fermions called technifermions, and new massless bosons technigluons which carry technicolor charge of the new force. The technifermions are grouped into left-handed doublets and right-handed singlets like the SM quarks and charged under the $SU(2)_L \times U(1)_Y$ to correctly break the electroweak symmetry in complete analogy with QCD. Just like

QCD the technifermions form bound states called technihadrons and the fermion anti-fermion bound states are called technimesons. The lightest of the technimesons are the π_T, ρ_T, ω_T, and a_T.

The technipions (π_T) play the same role as the pions from QCD breaking the local symmetry and giving masses to the $W^{\pm}$ and Z:

$$\begin{aligned} M_{W^{\pm}} &= \frac{g f_T}{2} \\ M_Z &= \frac{g f_T}{2\cos(\theta_W)} \\ \frac{M_{W^{\pm}}}{M_Z} &= \cos(\theta_W) \end{aligned} \tag{2.22}$$

The new technipion decay length f_T must be 246 GeV to predict $M_{W^{\pm}}$ and M_Z correctly. While this theory successfully breaks electroweak symmetry, a scaled up QCD version of technicolor suffers from a few problems in other areas. Most importantly, there are no fermion masses generated and this simple scaled up QCD theory is incompatible with precision Standard Model observables.

2.5.1 Extending Technicolor

To dynamically give mass to the Standard Model fermions using the same mechanism used for the gauge bosons, technicolor must be modified. Extended technicolor theories (ETC) [38, 39] unify QCD, technicolor, and flavor symmetries into a new gauge group, G_{ETC}. This new group is assumed to commute with the $SU(2)_L$ of the weak interactions but not the $U(1)_Y$ of electromagnetism, as this would result in pseudo-Goldstone bosons similar to axions. The G_{ETC} gives a dynamic understanding of the flavor structure observed in the Standard Model. Flavor changing neutral currents are an unavoidable problem in Extended technicolor theories. They arise from non-diagonal realistic mass matrices and the couplings of all fermions to Extended technicolor force currents. Experimentally flavor changing neutral currents are highly suppressed and are a stringent test of any theoretical model that contributes to their rate.

The heavy masses of fermions like the bottom and top quarks further complicate Extended technicolor contributions to flavor changing neutral currents. The larger mass requires stronger couplings which enhance the Extended technicolor contributions to flavor changing neutral currents. In order to address these issues and others Walking technicolor(WTC) was introduced [40–45]. Walking technicolor modifies the scaled up QCD dynamics by having a scale dependent gauge coupling $\alpha_T(\mu)$ that evolves slowly, or walks, over energy range of $\Lambda_T \lesssim \mu \lesssim M_{ETC}$. By assuming that $\alpha_T(\mu)$ remains close to the critical coupling, at which chiral symmetry breaking occurs, almost up to M_{ETC}, then SM fermion masses of $\mathcal{O}(\text{ GeV})$ can be generated solving the problem of the b-quark mass. At 172 GeV the top quark mass is still much too heavy to be accounted for by WTC.[5]

2.5.2 Low-Scale Technicolor

Walking technicolor theories require many generations of fermions giving many new technimesons. In models with several scalar doublets the scale of electroweak symmetry breaking is lower than that of the Standard Model. In WTC the vacuum expectation value is 90 MeV as opposed to the 246 GeV of the Standard Model. This light value implies light technihadrons on the order of a few hundred GeV. The phenomenology of these models is called Low-scale technicolor [47]. The lightest vector ρ_T and ω_T, and pseudo-scalar π_T technimesons are considered with techni-isospin assumed. This means that the ρ_T and ω_T are nearly degenerate in mass and will be referred to as a single resonance of ρ_T/ω_T.

[5] To account for the top mass, an additional force called Topcolor has been proposed. It couples to only the third generation giving rise to a significantly larger mass for the top quark [46].

2.5.3 Collider Signatures

The dominant decay mode of the ρ_T and ω_T is to a Standard Model gauge boson and a π_T. However, the decay to SM fermion pairs $f\bar{f}$, and particularly to leptons either e^+e^- or $\mu^+\mu^-$, offers a very clean search channel at a hadron collider. Figure 2·3 shows the Feynman diagram for such a process to dimuons. The dominant production mechanism is $q\bar{q}$ annihilation which produces a Z or γ^* through the Drell-Yan process (DY) [48] which "resonates" through a ρ_T/ω_T and then back through Z/γ^* which decay to the lepton pairs that are observed. This makes the dominant and irreducible background the smoothly falling dilepton spectrum. The collider signature for such a new particle search would be a narrow Breit-Wigner resonance in the dilepton invariant mass spectrum. The resolution of a realistic detector is not sufficient t resolve the true width of these resonances, as they have an intrinsic width of $\mathcal{O}(1\,\text{GeV})$, and so a Gaussian resonance is actually observed.

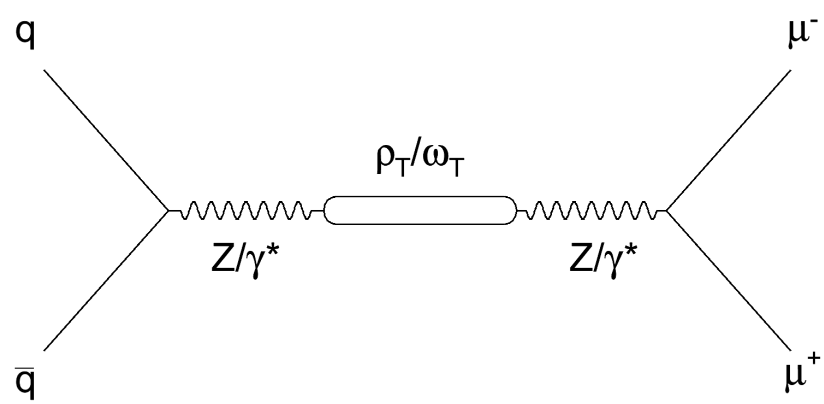

Figure 2·3: The Feynman diagram for production of a ρ_T/ω_T through $q\bar{q}$ annihilation resonating through the Drell-Yan process which then decays to $\mu^+\mu^-$ or any other lepton pairs.

The decay rate for ρ_T and $\omega_T \to f\bar{f}$ are given by [47]:

$$\begin{aligned}\Gamma(\rho_T^0 \to f\bar{f}) &= \frac{N_f \alpha^2 p}{3\alpha_{p_T}\hat{s}}\left[(\hat{s} - m_i^2)A_i^0(\hat{s}) + 6m_i^2 \mathcal{R}e(\mathcal{A}_{iL}(\hat{s})\mathcal{A}_{iR}^*(\hat{s}))\right] \\ \Gamma(\omega_T \to f\bar{f}) &= \frac{N_f \alpha^2 p}{3\alpha_{p_T}\hat{s}}\left[(\hat{s} - m_i^2)B_i^0(\hat{s}) + 6m_i^2 \mathcal{R}e(\mathcal{B}_{iL}(\hat{s})\mathcal{B}_{iR}^*(\hat{s}))\right]\end{aligned} \tag{2.23}$$

where A_i^0 and B_i^0 are

$$\begin{aligned}A_i^0(\hat{s}) &= |\mathcal{A}_{iL}(\hat{s})|^2 + |\mathcal{A}_{iR}(\hat{s})|^2, \\ B_i^0(\hat{s}) &= |\mathcal{B}_{iL}(\hat{s})|^2 + |\mathcal{B}_{iR}(\hat{s})|^2,\end{aligned} \tag{2.24}$$

and for $\lambda = L, R$

$$\begin{aligned}\mathcal{A}_{i\lambda}(\hat{s}) &= Q_i + \frac{2\zeta_{i\lambda}\cot 2\theta_W}{\sin 2\theta_W}\left(\frac{\hat{s}}{\hat{s} - \mathcal{M}_Z^2}\right), \\ \mathcal{B}_{i\lambda}(\hat{s}) &= \left[Q_i - \frac{4\zeta_{i\lambda}\sin^2\theta_W}{\sin^2 2\theta_W}\left(\frac{\hat{s}}{\hat{s} - \mathcal{M}_Z^2}\right)\right](Q_U + Q_D),\end{aligned} \tag{2.25}$$

and

$$\begin{aligned}\zeta_{iL} &= T_{3i} - Q_i \sin^2\theta_W, \\ \zeta_{iR} &= -Q_i \sin^2\theta_W, \\ \mathcal{M}_Z^2 &= M_Z^2 - i\sqrt{\hat{s}}\Gamma_Z(\hat{s}).\end{aligned} \tag{2.26}$$

For all these equations Q_i and $T_{3i} = \pm\frac{1}{2}$ are the electric charge and left handed weak isospin of the ith fermion, $\hat{s}$ is the energy of the interaction, and $\Gamma_Z(\hat{s})$ is the energy dependent width of the Z. The phenomenology of these lowest laying states has been incorporated into the MC software PYTHIA [49]. The cross section times branching ratio as a function of mass of the ρ_T/ω_T resonance for eight different center of mass energies is shown in Figure 2.5.3 [4].

The branching fraction to fermion pairs is dependent on what other decay channels are available. The other relevant decays involve the $\pi_T$and weak Boson pairs.

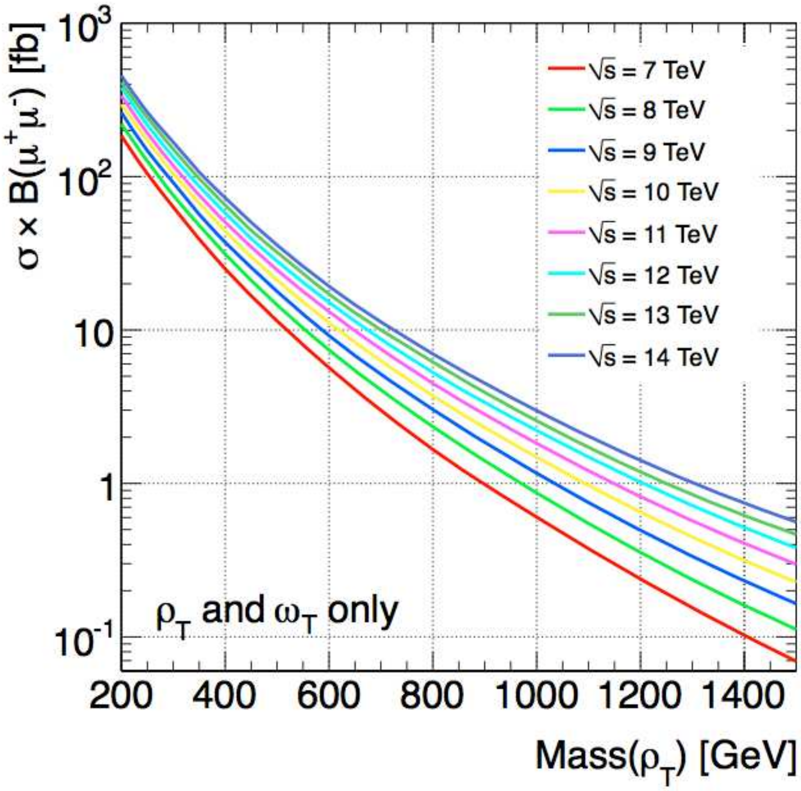

Figure 2·4: Technicolor cross section as a function of dimuon invariant mass for multiple center of mass energies, from Ref [4].

Therefore the mass splitting between the π_T and the ρ_T/ω_T sets the available decay rates for the ρ_T and ω_T. Figure 2·5 shows the cross section of the ρ_T/ω_T resonance as a function of $m(\pi_T)$ for three values of $m(\rho_T/\omega_T)$. There are three critical settings for m(π_T) relative to $m(\rho_T/\omega_T)$, when a new kinematically allowed decay "turns on":

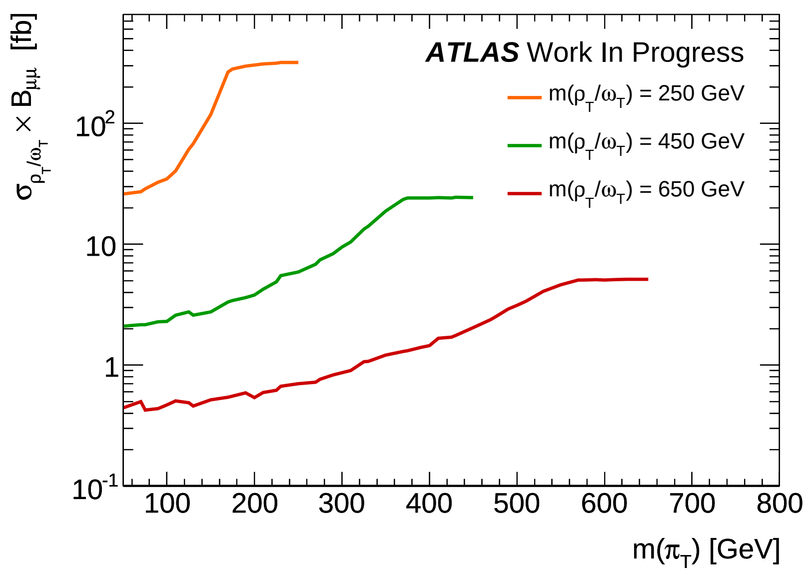

Figure 2·5: Low-scale technicolor cross section of a fixed mass ρ_T/ω_T resonance times the branching fraction to dimuons as a function of $m(\pi_T)$.

- When $\rho_T/\omega_T \rightarrow \pi_T + W/Z$ is allowed at m(π_T) $\leq$ m(ρ_T) - 90 GeV.
- When $\rho_T \rightarrow \pi_T\pi_T$ at m(π_T) $\leq \frac{1}{2}\times$ m(ρ_T).
- When $\omega_T \rightarrow \pi_T\pi_T\pi_T$ at m(π_T) $\leq \frac{1}{3}\times$m(ω_T).

In Figure 2·5 this first threshold can be seen as the transition from the"flat" portion of the curves to the falling. In this flat section no decays to the π_T are available so increasing $m(\pi_T)$ further does not increase the branching fraction to fermion pairs. At lower values of $m(\pi_T)$, the curve falls steeply as more phase-space becomes available for other decays. The second threshold when $m(\rho_T) = 2\ m(\pi_T)$ has only a slight affect on the distribution as the ρ_T accounts for only 10% of the signal produced. The third threshold $m(\omega_T) = 3\,m(\pi_T)$ further flattens out the distribution as the minimum branching fraction has essentially been reached and below this the branching fraction to fermion pairs is relatively insensitive to $m(\pi_T)$. In LSTC the expectation is that m(π_T) be greater than half the m(ρ_T). But since there is no way to know *a priori* what this mass splitting between the ρ_T/ω_T and π_T is we will search for ρ_T/ω_T for values of $m(\pi_T)$ from $\frac{1}{3} \times m(\rho_T) \leq m(\pi_T) \leq m(\rho_T)$.[6]

2.5.4 Current Limits

In the dilepton channel, previous limits on $m(\rho_T/\omega_T)$ have only been set for one value of $m(\pi_T)$.[7] This measurement will be the first to vary $m(\pi_T)$ to give a range of validity for a limit on $m(\rho_T/\omega_T)$. In the dilepton channel the strictest experimental limits come from the CDF collaboration [9]. They performed a search for a narrow spin-1 resonance above the continuous Drell-Yan spectrum in both the ee and $\mu\mu$ channel. They determined at 95% Confidence level that the ρ_T/ω_T must have masses above 280 GeV. Shown in Figure 2·6 is the result of this search.

Other collaborations have performed simultaneous searches for both the ρ_T/ω_T and the π_T. Direct searches of π_T are not possible in the dilepton channel and as such have a more complex final state. The two strictest searches cover different regions of the parameter space. The CDF Collaboration exclude $m(\rho_T) = 180$ - 250 GeV, and $m(\pi_T) = 95$ - 145 GeV in the W+jj channel [11]. The results of this search are

[6] Values of $m(\pi_T) \geq m(\rho_T)$ are not motivated theoretically and not considered in this search.

[7] Experimentally the choices of the LSTC parameters greatly affect the expected and measured limits. As shown in Figure 2·5 these parameters can have a large impact on the cross sections, and make direct comparison of experimental results difficult or even impossible. The parameter choices used in this analysis are given in detail in Chapter 7.

shown in Figure 2·8. The D0 Collaboration excludes $m(\rho_T)$ = 208 - 408 GeV and $m(\pi_T)$ = 120 - 408 GeV in the WZ channel, shown in Figure 2·7 [10].

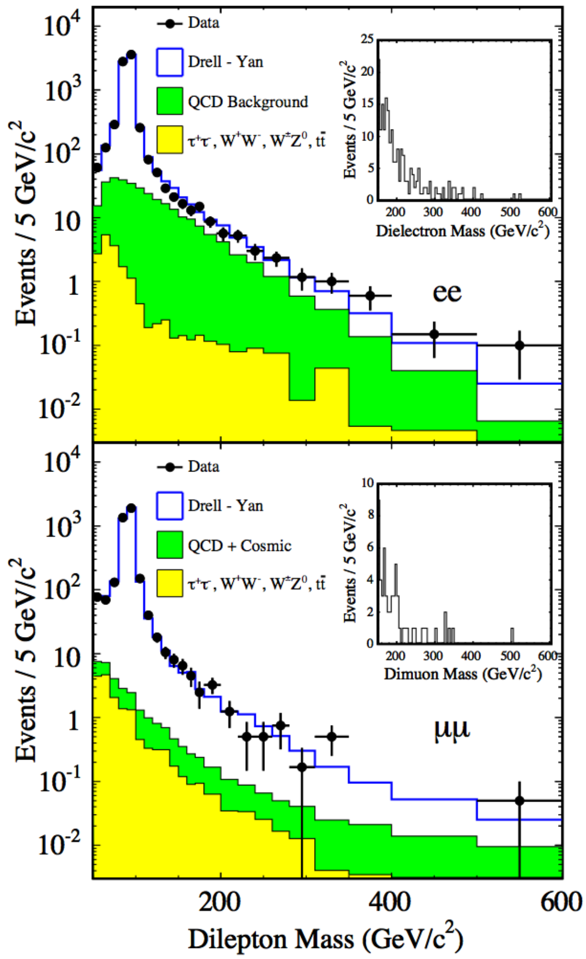

Figure 2·6: CDF Collaboration dilepton invariant mass distribution, from Ref [9]. Above *ee* below $\mu\mu$, the inserts show the distribution of M_{ll} > 150 GeV. In neither search do they observe a statistically significant excess.

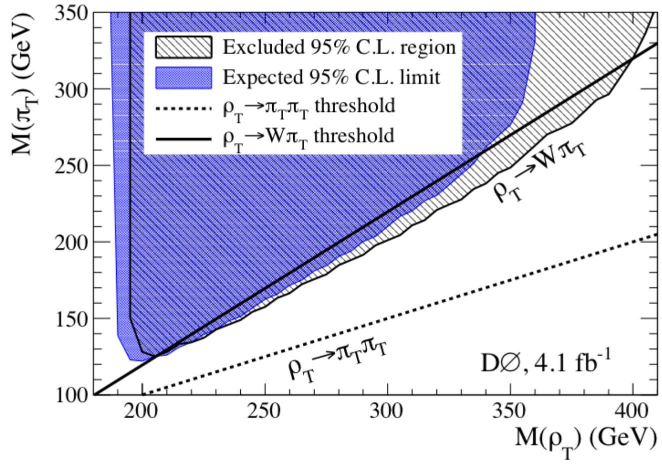

Figure 2·7: The observed and expected 95% Confidence level limits, as a function of $m(\pi_T)$ vs. $m(\rho_T)$ in the WZ channel, from the D0 Collaboration Ref [10].

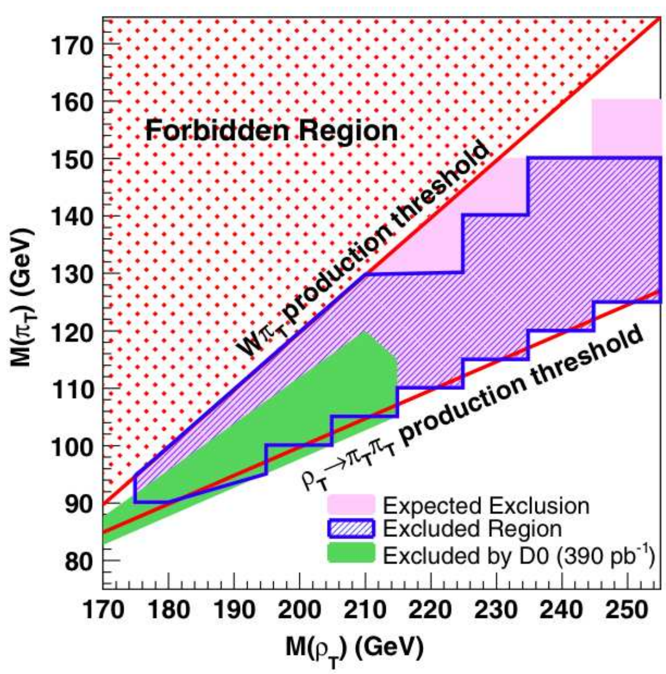

Figure 2·8: The observed and expected 95% Confidence level limits, as a function of $m(\pi_T)$ vs. $m(\rho_T)$ in the Wjj channel, from the CDF Collaboration Ref [11].

Chapter 3

The Large Hadron Collider

3.1 Accelerator and Complex

The Large Hadron Collider (LHC) [2], was designed to be a 14 TeV center of mass energy proton-proton circular synchrotron collider.[1] In the LHC are two counter rotating proton beams, each in an evacuated beam pipe. These proton beams collide head-on at four interaction points, illustrated in Figure 3·1. The LHC is located in a tunnel 100m below the French-Swiss border at the European Organization for Nuclear Research (CERN) outside of Geneva Switzerland. Along the 27 km circumference of the LHC, the proton beams are “steered” by 1232 super conducting dipole bending magnets, and focused using quadrapole and sextapole magnets. Radio Frequency cavities accelerate proton bunches at each revolution of the beams through point four. In addition to proton proton collisions the LHC is designed to collide singly ionized atoms up to the atomic mass of lead.

The LHC is fed by a series of smaller accelerators (shown in Figure 3·2), that CERN has constructed throughout its 50 year history, each successively increasing the energy of the proton beams. The protons begin as ionized hydrogen gas and are accelerated to 0.3c in a linear accelerator (LINAC). They are next passed to the Proton Synchrotron (PS) and Super Proton Synchrotron (SPS) which increase the beam energy up to 25 GeV and then 450 GeV where they are passed to the LHC. The

[1] Currently running at 7 TeV.

injected protons are then accelerated by the Radio Frequency cavities in the LHC from 450 GeV up to 7000 GeV, at which point focusing and squeezing of the beams occur to cause the proton bunches to collide at the four interaction points. For the data taking in 2010 and 2011 each proton beam was accelerated up to 3.5 TeV.

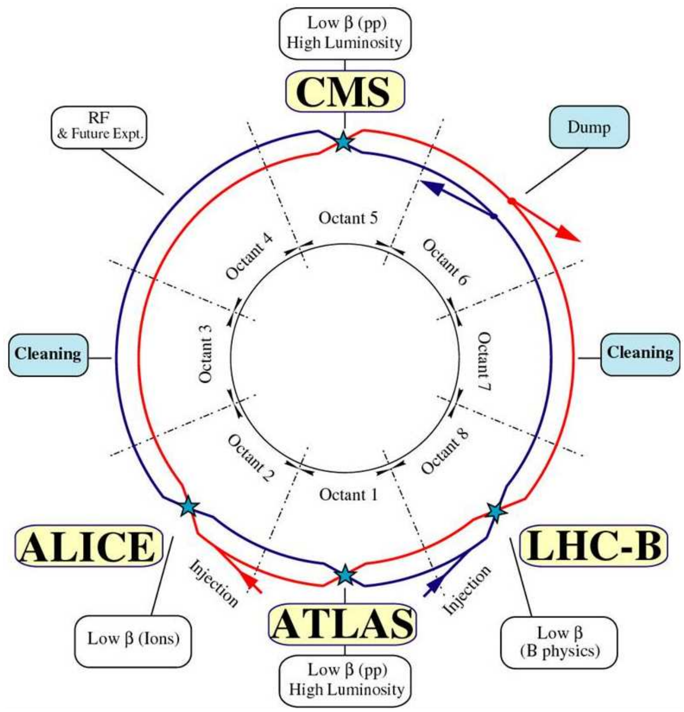

Figure 3·1: Schematic layout of the LHC. Including counter rotating beams, octal symmetry, and experimental locations, from Ref [2].

3.2 Luminosity

At a particle accelerator collisions produce all allowed physics processes, for any single process the number of events that we observe will be proportional to the theoretical cross section times the integrated luminosity,

$$N_{event} = \mathcal{L}\sigma_{event}. \tag{3.1}$$

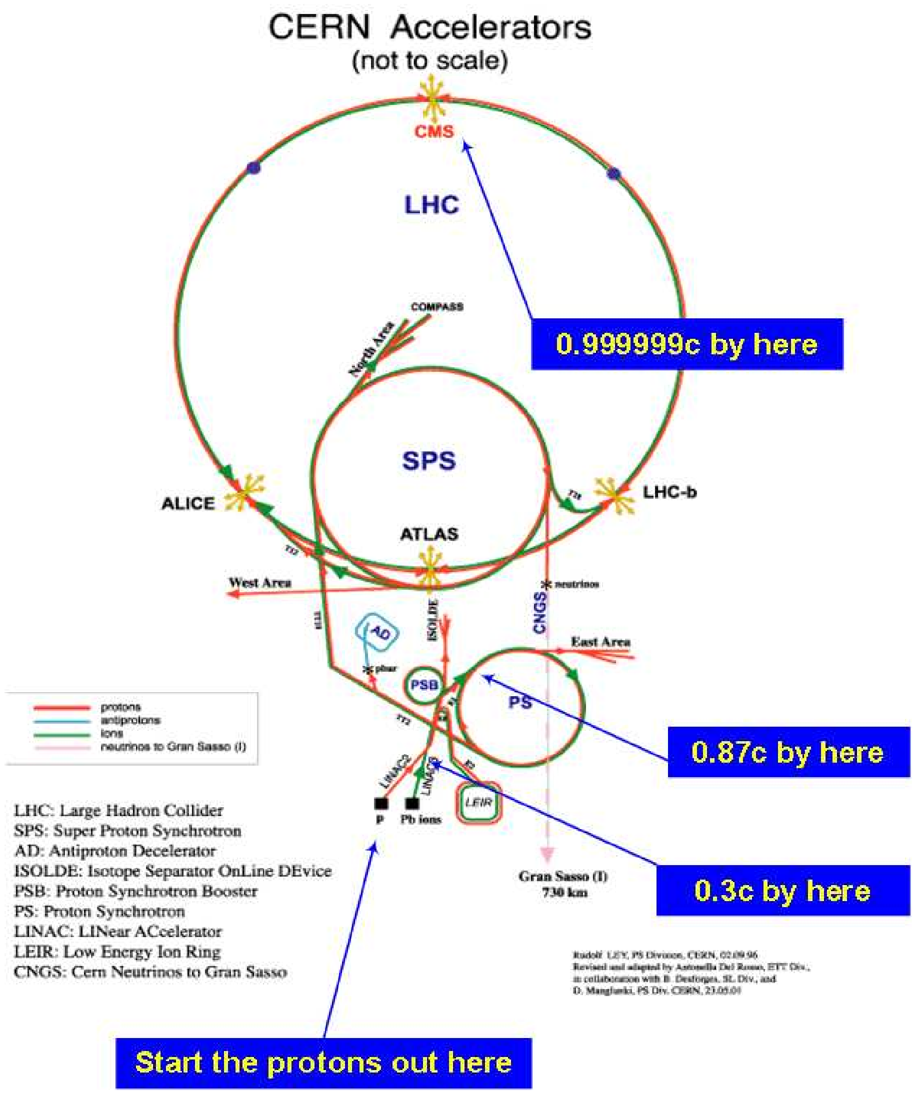

Figure 3·2: The CERN accelerator complex, from Ref [2]. Starting with the linear accelerators LINAC1 and LINAC2 the proton beams are stepped up in energy through the PS, SPS and finally LHC.

Here σ_{event} is the theoretical cross section of the physics process, and $\mathcal{L}$ is the integrated luminosity. Integrated luminosity is the integral of instantaneous luminosity, L, a measure of how intense the beams are, or how many interactions are occurring in the detector at any given moment. In general, parameters which increase the number and density of protons in the beam and the energy of the beams increase luminosity, and those that lower these quantities decrease it. The instantaneous luminosity can be determined by the beam parameters, which for a bunched beam with standard Gaussian particle distribution can be written as:

$$L = \frac{N_B^2 n_b f_{rev} \gamma}{4\pi \epsilon_n \beta^*} F \tag{3.2}$$

Here L depends quadratically on N_B the number of protons per bunch, n_b the number of bunches making up a beam, f_{rev} the revolution frequency for a single bunch, the relativistic gamma γ, and F the geometric luminosity reduction factor. L is inversely proportional to ϵ_n the normalized transverse beam emittance and β^* the beta function at the collision point, related to the interaction size [2]. At the interaction point (IP) with a crossing angle θ_c between the counter rotating beams, and transverse and longitudinal RMS size σ^* and σ_z, F is determined by Eqn 3.3, relating the geometric size of the interaction region to instantaneous luminosity.

$$F = \left(1 + \left(\frac{\theta_c \sigma_z}{2\sigma^*}\right)^2\right)^{-\frac{1}{2}} \tag{3.3}$$

At the LHC the large number of bunches circulating in the machine at high intensity require a crossing angle so that collisions between the beam occur at only the IP of the experimental halls. This requires that θ_c be non-zero, to avoid parasitic collisions in the detector hall away from the central interaction point.

Assuming both colliding beams have the same properties at design energy and peak luminosity the LHC has the parameters in Table 3.1, from Ref [2]. Table 3.1 also shows the beam parameters as determined over the summer of 2011 with 3.5 TeV per beam. These parameters have been calculated and measured from different techniques such as beam current monitors, van der Meer scans, and total cross section measurement. Using these techniques the relative uncertainty on integrated luminosity, measure in ATLAS, is currently 3.4% [12].

Table 3.1: LHC beam parameters at peak instantaneous luminosity and nominal 7 TeV per beam energy, from Ref [2], as well as the parameters during the Summer of 2011 with beams colliding at 3.5 TeV.

Parameter	Meaning	Nominal Value	2011 Value
	L		
N_B	Number of Protons per Bunch	1.15×10^{11}	1.1×10^{11}
n_b	Number of Bunches per Beam	2808	1380
f_{rev}	Frequency of Revolution	11 kHz	11 kHz
γ	Relativistic Gamma Factor	7461	3284
ϵ_n	Transverse Beam Emittance	3.75×10^-4 cm	2.7×10^{-3} cm
β^*	Beta Function At Collision Point	0.55	1.5
	F		
σ_z	RMS Bunch length	7.55 cm	7.55 cm
σ^*	RMS Cross sectional area	16.7 μm^2	16.7 μm^{-2}
θ_c	Crossing Angle	285 μrad	285 μrad

3.3 Performance and Challenges

At 14 TeV center of mass energy the LHC is designed to reach L of 10^{34} cm^{-2} s^{-1} two orders of magnitude higher than Fermilab's proton anti-proton Tevatron collider's 4×10^{32} cm^{-2} s^{-1}. In March of 2011 the LHC began to collide beams at 7 TeV center of mass energy, reaching L of 10^{32} cm^{-2} s^{-1}, this continued through July, when a scheduled maintenance shutdown took place. Over the course of this first physics run in 2011 at 7 TeV the LHC was able to deliver 1.24 fb^{-1} of integrated luminosity to ATLAS. Figure 3·3 shows the increases in integrated luminosity achieved during the entire 2011 physics run [12]. This analysis corresponds to the amount of data taken up to the second flat section from March 21st to June 28th. These flat periods where no additional luminosity is recorded correspond to the technical stops scheduled to allow work on the accelerator and detectors.

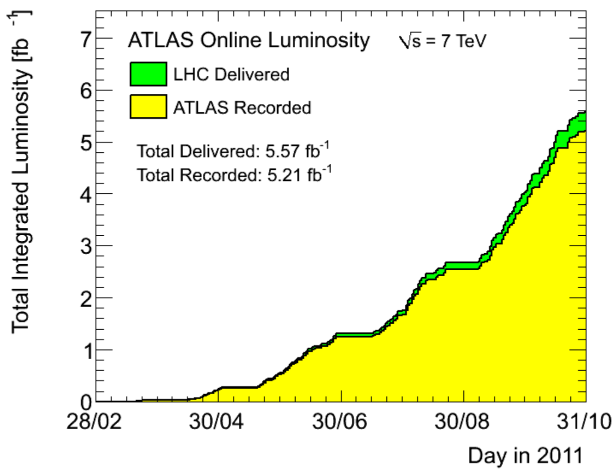

Figure 3·3: Integrated luminosity by day in 2011, produced using methods from Ref [12]. The flat sections are technical stops allowing for work to be done on the accelerator and experiments.

The parameters in Equation 3.2 are not yet at their design values, but the LHC is currently running at $\sim 10^{32}$ cm^{-2} s^{-1}, the same order as that of the Tevatron. Being at 7 TeV center of mass energy significantly increases the cross section of many interesting physics processes at the LHC compared to the Tevatron at 2 TeV. At the design $L = 10^{34}$ cm^{-2} s^{-1} the LHC luminosity is high enough that on average 19.8 proton proton interactions occur per beam crossing in the ATLAS detector. For this analysis the average number of interactions, $< \mu > = 6.3$, and has gotten as high as 11.6 in later data taking. Shown in Figure 3·4 is the average number of interactions as a function of recorded luminosity. The average number of interactions is calculated by:

$$< \mu >= \frac{L\sigma_{inel}}{n_b f_{rev}}. \tag{3.4}$$

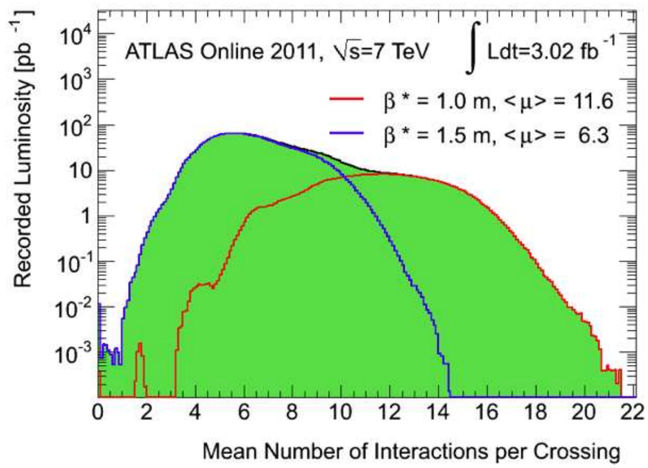

Figure 3·4: Mean number of interactions during the 2011 data taking, before and after a luminosity upgrade which lowered β^*. Produced using methods from Ref [12].

3.4 Physics at a Hadron Collider

Protons are composite objects made up of quarks and gluons with different fractions of the total proton momentum, as shown in Figure 2·1. At high energies when two protons "collide" one constituent particle from each proton, interact via a gauge boson in what is referred to as the "hard scatter" with a large momentum transfer. The other particles in the proton are referred to as the spectators and either go down the beam pipe, or hit the forward detectors as jets of particles. Shown in Figure 3·5 is a schematic diagram of this process where two composite hadrons A and B have constituents a and b interact through some process $\hat{\sigma}$. The interacting particles carry some unknown fraction of the total momentum $f_{a/A}$ and $f_{b/B}$ with the remaining momentum carried by the remainder of the proton [13]. This process repeats every 25 ns, leaving experimentalists to reconstruct which $\hat{\sigma}$ process took place and study the interactions of interest.

The total inelastic cross section is $\sigma_{\text{tot}} = 71.5 \ \ mb$ [50], with the most likely

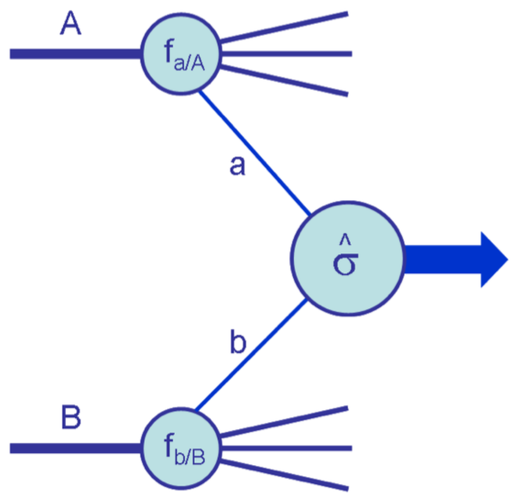

Figure 3·5: Schematic diagram of a generic hard scatter process between two protons, from Ref. [13].

interactions at a hadron collider due to QCD. Figure 3·6 shows the cross section for many processes at various center of mass energies. The vertical dashed line at 2 TeV corresponds to the Tevatron, and at 14 TeV the design center of mass energy of the LHC. The production of W and Z bosons have cross sections on the order of 10^6 smaller than $\sigma_{\rm tot}$ at 10 – 100 nb. The Z boson production σ_Z is the dominant background to a dilepton search. In Figure 2.5.3 the cross section for a Technicolor signal was shown, which at 14 TeV has values of about 10 – 100 fb. This is a factor of 10^4 lower than the high invariant mass irreducible dilepton background and 10^{12} less than the total cross section. The low rate of these electroweak processes compared to QCD backgrounds necessitates the use of a trigger system that makes a decision every 25 ns to determine the type of interaction that just took place and its relative interest to the collaboration.

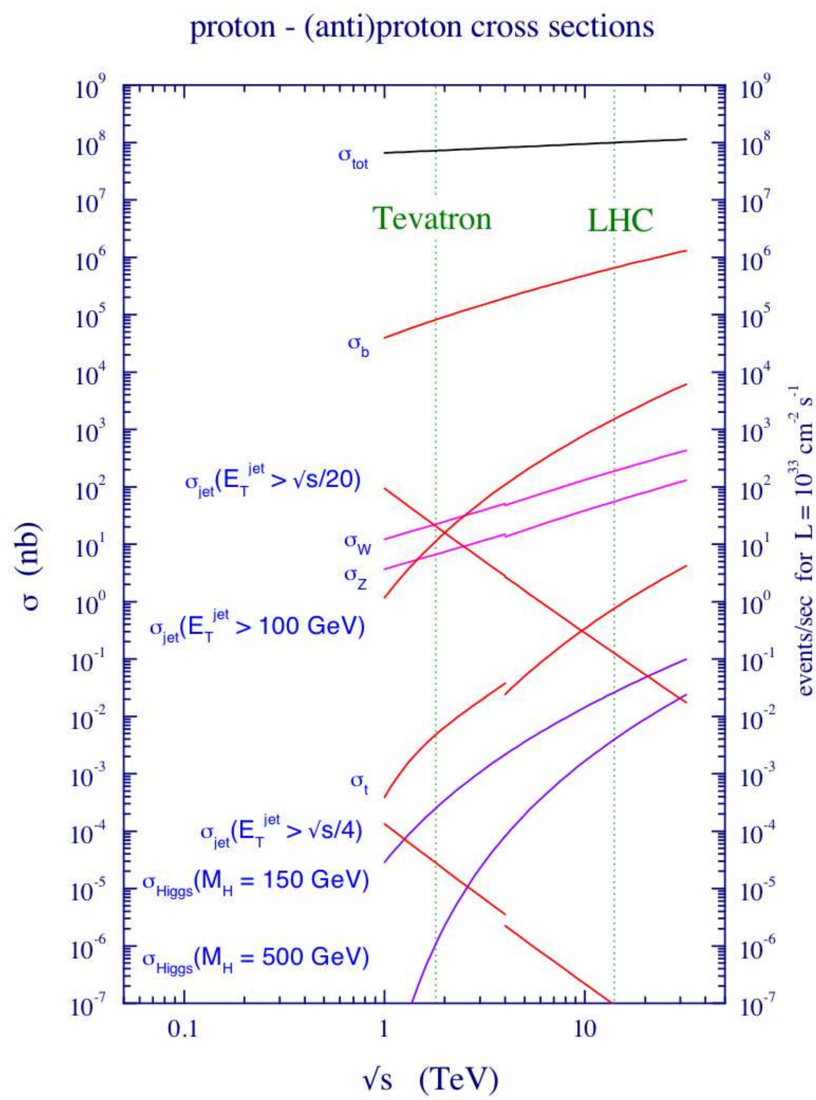

Figure 3·6: Shown are Standard Model cross sections as a function of center of mass energy from Ref. [13]. The dashed green vertical lines indicate the Tevatron and LHC design center of mass energy.

Chapter 4

The ATLAS Detector

4.1 General Purpose High Energy Physics Detectors

Over the last three decades a new type of detector designed to produce many different physics results over a broad range of topics has been developed in the High Energy Physics (HEP) community. The physics goals of such a detector are to reconstruct interactions and decays of short lived particles. This is done by reconstructing as much information as possible for the stable particles on an event by event basis. This requires accurate measurement of each stable object's detector response to identify particle type and reconstruct its four-momentum (p^μ). To accomplish this a detector is built as symmetric and as close to full 4π angular coverage as possible. Using nested detector technologies designed to provide complimentary information and measurements. Figure 4·1 shows the ATLAS detector [14], an example of a general purpose HEP detector.

The three sub-systems common to general purpose HEP detectors consist of two magnetic spectrometers and a calorimeter system. An inner tracking system, located closest to the beam pipe, with extremely fine segmentation is designed to reconstruct the momentum of all charged particles coming from the interaction point (IP). The inner tracker also provides a precise measurement of track vertices and measures deviations from the IP. It is used in the reconstruction of e, μ, hadronic jets, heavy flavor jets. Outside of that volume, a calorimeter system comprised of a

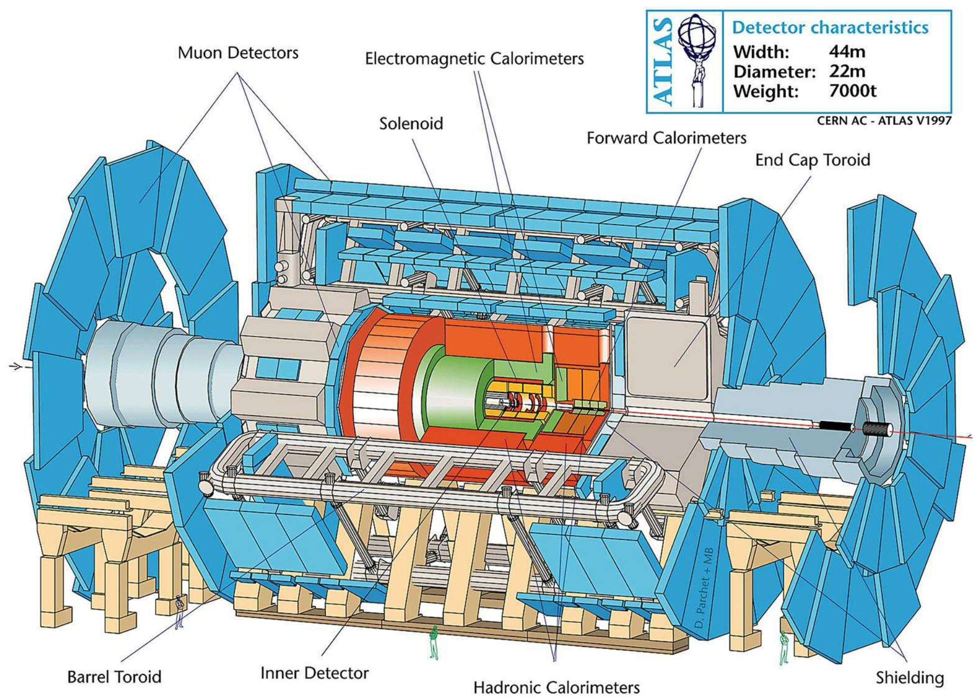

Figure 4·1: The ATLAS Detector, comprised of two magnetic spectrometers, the Inner Detector and the Muon Spectrometer, and the calorimeters, from Ref [3]. ATLAS is cylindrical in shape and covers a volume of 17,000 m^3.

finely segmented electromagnetic calorimeter to measure showers from electrons and photons, and then a heavy hadronic calorimeter with large geometric coverage to measure hadronic jets of particles, E_T^{miss},[1] and H_T.[2] An additional design feature of the hadronic calorimeter is that it be thick enough to limit hadronic punch through to the final detector system. The second magnetic spectrometer, designed to reconstruct tracks of muons and trigger on events with muons. In all cases the sub-systems are centered around the beam pipe and consist of a cylindrical barrel with two disk shaped end-caps on either side. A sub-detector's cracks and transitions between barrel and end-cap section are designed to minimize the gaps in coverage and be non-projective towards the interaction point, to maximize coverage and limit punch through into the Muon Spectrometer.

4.2 ATLAS

The ATLAS (A Toroidal LHC ApparatuS) detector [14], located at Point 1(Figure 3·1) on the LHC ring, is a new general purpose high energy physics detector. It is made up of nine distinct sub-detectors, grouped together into the three previously mentioned major sub-systems. The ATLAS detector is cylindrical in shape, 44m long, 22m in diameter, and weighing 7000 tons. The large size is necessary to increase the lever-arm of the magnetic spectrometers and to contain showers of particles.

ATLAS uses a right-handed coordinate system with its origin at the nominal interaction point in the center of the detector and the z-axis along the beam pipe. The x-axis points from the interaction point to the center of the LHC ring, and the y axis points upward. Cylindrical coordinates (r, ϕ) are used in the transverse plane,

[1] E_T^{miss} is the vector sum of all transverse energy in the detector. It is used to detect non-interacting particles such as neutrinos.

[2] H_T is the scalar sum of all hadronic activity in an event. It is a handle on how much energy was involved in the hard scatter.

ϕ being the azimuthal angle around the beam pipe. Instead of the z coordinate ATLAS uses pseudo-rapidity, η defined as:

$$\eta = -\ln\left(\tan\left(\frac{\theta}{2}\right)\right) = \frac{1}{2}\ln\left(\frac{|p|+p_z}{|p|-p_z}\right) \tag{4.1}$$

where θ is the angle to the particle trajectory and the beam axis $\hat{z}$. The second equality in Eqn 4.1 is the same as the definition for rapidity with the assumption that all particles are massless. This accounts for the difference between rapidity and pseudo-rapidity. Differences in pseudo-rapidity are insensitive to Lorentz boosts along the z-axis, making this a very useful coordinate at a hadron collider where the z component of the velocity of the partonic rest frame is not known event by event.

The resolution requirements and trigger coverage of the ATLAS detector major sub-systems are summarized in Table 4.1 [3]. These performance goals are determined by the physics requirements of the experiment. For the Muon Spectrometer reconstructing a 1 TeV Z' decaying to dimuons determines the $\sigma_{\mathrm{p_T}}$ and reconstructing a Higgs boson decaying to four muons determines the geometric acceptance [14].

Table 4.1: General performance goals of the ATLAS detector. Note that, for high-$\mathrm{p_T}$ muons, the Muon Spectrometer performance is independent of the Inner Detector system, from Ref [3]. The units for E and $\mathrm{p_T}$ are in GeV.

Detector component	**Required Resolution**	**η coverage**	
		Measurement	Trigger
Tracking	$\sigma_{\mathrm{p_T}}/\mathrm{p_T} = 0.05\%\ \mathrm{p_T} \oplus 1\%$	2.5	
EM calorimetry	$\sigma_E/E = 10\%/\sqrt{E} \oplus 0.7\%$	3.2	2.5
Hadronic calorimetry (jets)			
barrel and end-cap	$\sigma_E/E = 50\%/\sqrt{E} \oplus 3\%$	3.2	3.2
forward	$\sigma_E/E = 100\%/\sqrt{E} \oplus 10\%$	$3.1< \lvert\eta\rvert < 4.9$	$3.1< \lvert\eta\rvert < 4.9$
Muon Spectrometer	$\sigma_{\mathrm{p_T}}/\mathrm{p_T} = 10\%$ at $\mathrm{p_T} = 1$ TeV	2.7	2.4

4.3 The Inner Detector

The sub-system closest to the beam pipe first reached by particles traveling outward from the interaction point is the Inner Detector (ID). The Inner Detector is composed of three tracking detectors, using separate technologies, inside a 2 T solenoid field, along the z-axis, giving a measurement of all charged particle momenta. Some longer lived relativistic particles such as mesons containing b-quarks decay a measurable distance away from the interaction point. These displaced particle vertices can be reconstructed by finding the intersection of the daughter tracks. To achieve the necessary precision while keeping occupancy and cost low, the ATLAS Inner Detector uses three separate sub-detectors: Pixel and silicon microstrip (SCT) trackers, and the straw tubes of the Transition Radiation Tracker (TRT). Seen in Figure 4·2 is a schematic for the Inner Detector technologies. The arrangement of the sub-detectors is such that the highest granularity detector the Pixel detector is closest to the beam pipe, and each successive detector decreases in granularity.

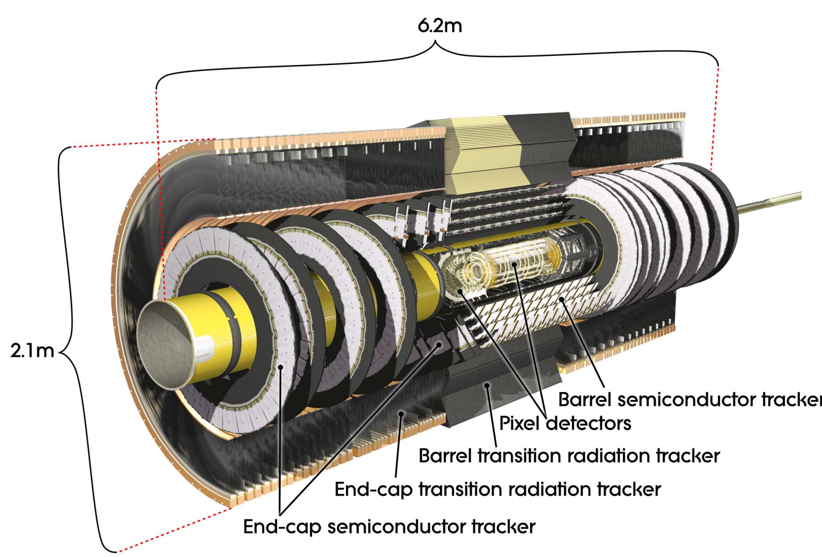

Figure 4·2: Cut-away view of the ATLAS Inner Detector with labeled sub-detectors, from Ref [3].

As the ID is inside a solenoid magnetic field, aligned with the z-axis, the bend plane of charged particles is $R-\phi$ therefore the detector segmentation in $R-\phi$ is finer than in z. Segmentation in the $R-\phi$ plane allows for precise momentum measurement of charged tracks, while segmentation in z is necessary to keep occupancy down, aid in pattern recognition, and reconstruct secondary vertices. Each ID subdetector's position resolution and alignment tolerances necessary to give the $\sigma_{\mathrm{p_T}}$ of Table 4.1 is summarized in Table 4.2. The Inner Detector contribution to measuring muon tracks is dominant at low-$\mathrm{p_T}$. For muon tracks with $\mathrm{p_T} \geq 100$ GeV the measurement is dominated by the Muon Spectrometer, due to the larger lever arm.

Table 4.2: Intrinsic measurement accuracies and mechanical alignment tolerances for the Inner Detector as defined by the performance requirements of ATLAS [3]. The numbers correspond to the single module accuracy for the pixel and SCT and the single straw drift-time accuracy for the TRT.

Item	**Intrinsic accuracy** (**μm**)	**Alignment Tolerances** (**μm**)		
		Radial (R)	**Axial** (z)	**Azimuth** ($R-\phi$)
Pixel				
Layer-0	10 ($R-\phi$) 115 (z)	10	20	7
Layer-1 and Layer-2	10 ($R-\phi$) 115 (z)	20	20	7
Disks	10 ($R-\phi$) 115 (R)	20	100	7
SCT				
Barrel	17 ($R-\phi$) 580 (z)	100	50	12
Disks	17 ($R-\phi$) 580 (R)	50	200	12
TRT	130			30

4.4 Calorimeters

The ATLAS calorimeters main role is to provide accurate measurement for electromagnetic and hadronic showers. The second is to limit punch-through into the muon system. Achieving both of these goals requires good depth of absorber material over the full range of η coverage. This is because to accurately measure a shower the shower should be contained, and the calorimeter well segmented. Over the η region covered by the Inner Detector, the electromagnetic calorimeter has fine granularity for the precision measurements of electrons and photons. The coarser granularity of the rest of the calorimeter is sufficient to satisfy the physics requirements for jet reconstruction and E_T^{miss} from Table 4.1. A view of the ATLAS calorimeters is presented in Figure 4·3. All of the ATLAS calorimeter sub-detectors are sampling calorimeters. Sampling calorimeters are calorimeters that use different materials for absorber and scintilator.

To limit punch through and contain all showers the total thickness of the electromagnetic (EM) calorimeter is more than 22 radiation lengths (X_0), and the hadronic calorimeters are over 9.7 hadronic interaction lengths (λ) thick. This total thickness of $\sim$11 λ including support structure has been measured using test beam data [51] to adequately reduce punch-through below the irreducible level of non-prompt decay muons. When combined the calorimeter systems cover the range of $|\eta| <$4.9, each using techniques suited to the widely varying requirements of the physics processes and radiation environment.

4.4.1 LAr Electromagnetic Calorimeter

The Electromagnetic calorimeter is a lead-LAr sampling calorimeter with accordion shaped electrodes and lead absorber plates over its full coverage. The detector strategy is to measure the ionization in the active material, liquid-Ar, from showers of particles coming from high energy electromagnetic particles interacting with the lead absorber material. The accordion ("zig-zag") geometry provides complete ϕ symmetry without azimuthal cracks. In the region $|\eta| < 2.5$ the electromagnetic calorimeter is segmented in three sections in depth to provide shower profile information. This gives superior resolution to radial readout and helps in distinguishing true electromagnetic showers from "fakes" due to pions or other instrumental issues. In the central region of $|\eta| <1.8$ a presampler is used to correct for the energy lost by electrons and photons in the dead material upstream of the calorimeter. The presampler is made necessary by the position of the central solenoid in front of the electromagnetic calorimeter, as well as the support structure and services for the Inner Detector.

4.4.2 Hadronic Calorimeters

The Hadronic Calorimeter system is made up of two separate technologies. In the central region ($|\eta| < 1.7$) there is a lead scintillator sampling calorimeter referred to as the Tile Cal. It is a sampling calorimeter using steel as the absorber and scintillating tiles as the active material. In the forward region of $1.5 < |\eta| < 4.9$ two LAr sampling calorimeters are used. The tile calorimeter is placed directly outside the electromagnetic calorimeter. Radially, the tile calorimeter extends from an inner radius of 2.28 m to an outer radius of 4.25 m segmented in depth in three layers to provide shower profile information. Two sides of the scintillating tiles are read out by wavelength shifting fibers into two separate photo-multiplier tubes, giving longitudinal shower information.

In addition to the central Tile Cal the hadronic calorimeter system includes two dedicated end cap calorimeter technologies, both of which use LAr as the active material. These lower granularity detectors' primary role is to aid in H_T and E_T^{miss} measurements and forward jet reconstruction. Together they cover the range $1.5 < |\eta| < 4.9$ overlapping slightly with the Tile Cal. They are known as the LAr hadronic end-cap calorimeter (HEC) and the LAr Forward calorimeter (FCal).

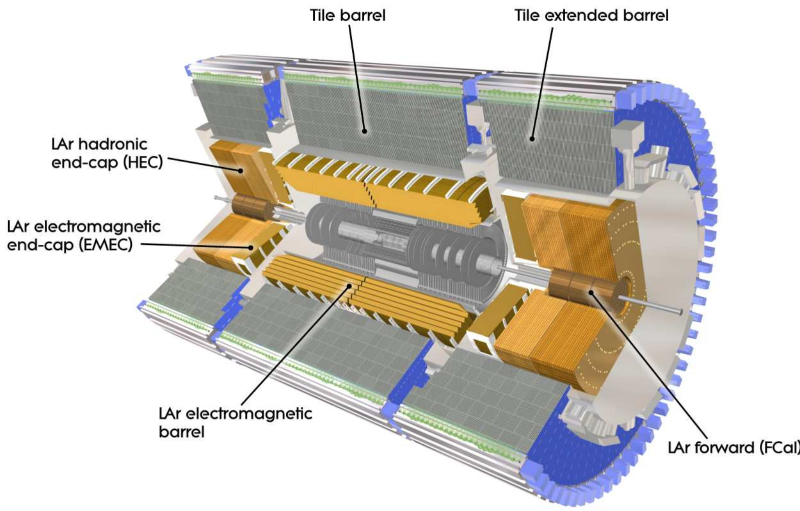

Figure 4·3: Cut-away view of the ATLAS calorimeter system, from Ref [3].

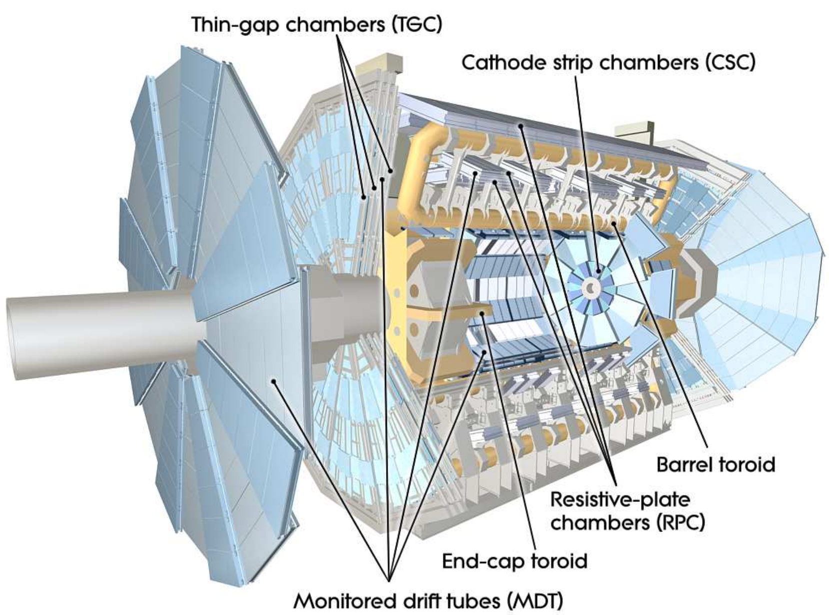

Figure 4·4: Cut-away view of the ATLAS muon system, from Ref [3].

4.5 The Muon Spectrometer

The ATLAS Muon Spectrometer (MS) is a tracking detector which measures the magnetic deflection of muon tracks in a large superconducting air-core toroid magnetic field. Instrumented with separate fast response trigger and high-precision tracking chambers, a combination of four complementary technologies are used to achieve the physics performance goals. The toroidal magnetic field, which points in ϕ, is orthogonal to the solenoid field in the Inner Detector and having an air gap minimizes multiple scattering, due to Coulomb interactions. In the barrel and end-cap regions, tracks are measured in chambers arranged in three cylindrical layers in the central region and three disks in the end-cap region. These three layers are called stations and are symmetric around the beam axis. In the transition region where the barrel and end-cap toroids meet, and the magnetic field has large variations, and additional chambers are installed to add measurement stations and improve resolution. The conceptual layout of the Muon Spectrometer is shown in Figure 4·4 and the main parameters of the muon chambers are listed in Table 4.3.

4.5.1 Muon Chamber Technologies

The Muon Spectrometer sub-detectors are broken up into two categories, the first provide precise measurements of position, and the second offer fast response for triggering. Over most of the angular coverage precision measurement of the track momentum is provided by the Monitored Drift Tubes (MDTs), a proportional wire drift chamber. For $2.0 < |\eta| < 2.7$, Cathode Strip Chambers (CSCs), a multi-wire proportional chamber with segmented cathode strips and higher granularity are used. The CSCs are designed to withstand the demanding rate and background conditions of this high particle flux and radiation region.

The fast response trigger chambers cover the range $|\eta| < 2.4$. In the barrel ($|\eta| <$

Table 4.3: Main parameters of the Muon Spectrometer [3]. Numbers in brackets for the MDTs and the RPCs refer to the final configuration of the detector.

Monitored drift tubes	**MDT**
- Coverage	$\|\eta\| < 2.7$ (innermost layer: $\|\eta\| < 2.0$)
- Number of chambers	1088 (1150)
- Number of channels	339,000 (354,000)
- Function	Precision tracking
Cathode strip chambers	**CSC**
- Coverage	$2.0 < \|\eta\| < 2.7$
- Number of chambers	32
- Number of channels	31,000
- Function	Precision tracking
Resistive plate chambers	**RPC**
- Coverage	$\|\eta\| < 1.05$
- Number of chambers	544 (606)
- Number of channels	359,000 (373,000)
- Function	Triggering, second coordinate
Thin gap chambers	**TGC**
- Coverage	$1.05 < \|\eta\| < 2.7$ (2.4 for triggering)
- Number of chambers	3588
- Number of channels	318,000
- Function	Triggering, second coordinate

1.05) Resistive Plate Chambers (RPCs) are used and in the region $1.05 < |\eta| < 2.4$ Thin Gap Chambers (TGCs) are used. The trigger chambers for the Muon Spectrometer serve a threefold purpose: provide bunch-crossing identification (BCID), provide a trigger with well-defined p_T thresholds, and measure the muon's ϕ coordinate for track reconstruction. A more detailed discussion of the Muon Spectrometer layout, technologies, and challenges can be found in Chapter 5.

4.6 Magnet System

The ATLAS magnet system is comprised of a solenoid field for the Inner Detector and a toroidal field for the Muon Spectrometer. For muons which pass through the whole detector these two separate magnet systems provide orthogonal measurements of momentum. Figure 4·5 shows the orientation of the windings of the magnets and

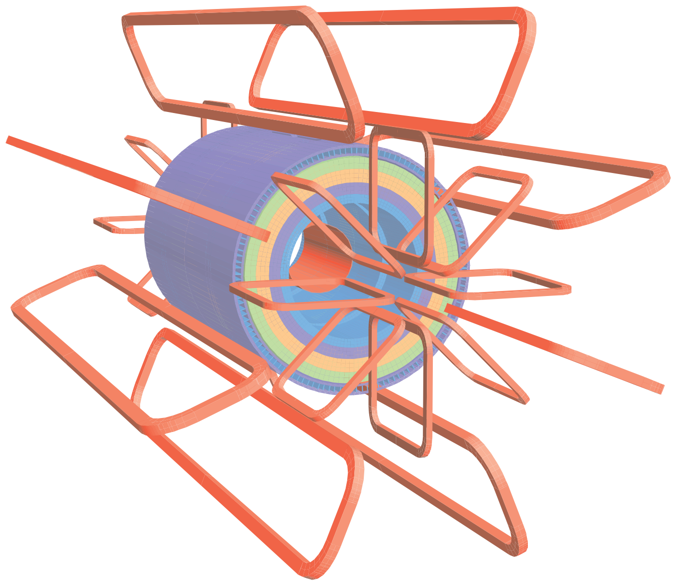

Figure 4·5: Geometry of magnet windings and tile calorimeter steel. The eight barrel toroid coils, with the end-cap coils interleaved are visible. the solenoid winding lies inside the calorimeter volume, from Ref [3].

the Tile Cal steel. The steel in the calorimeters acts as the flux return for the solenoid field. In the Muon Spectrometer the magents are air gap toroids, each with eight coils.

4.6.1 Central Solenoid

The 2 T superconducting solenoid magnet with $\overrightarrow{B}$ along positive $\hat{z}$ bends tracks traversing the Inner Detector in the $r - \phi$ plane. The solenoid has an inner radius of 2.46 m and and outer radius of 2.56 m and length of 5.8 m, with 40 MJ of stored energy at the nominal 7.730 kA operating current. With a weight of 5.7 tons the solenoid and its cryostat contribute ∼0.66 radiation lengths to the total dead material of ATLAS, at $\eta = 0$.

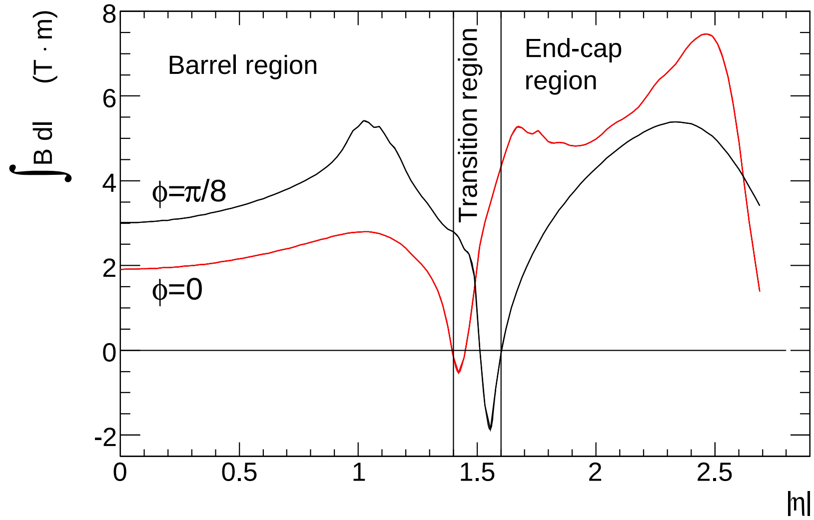

Figure 4·6: Predicted field integral as a function of $|\eta|$ in one toroid octant, for an infinite momentum muon. The red curve corresponds to $\phi = 0$ and black $\phi = \pi/8$, from Ref [3].

4.6.2 Muon Spectrometer Toroids

In the ATLAS Muon Spectrometer eight "race track" superconducting magnets are used to create a toroidal magnetic field. The symmetrically spaced windings of each magnet can be seen in the diagram of Figure 4·5. The barrel toroid has an individual cryostat for each winding, while for each of the two end-cap toroids all eight windings are in the same cryostat. To reduce multiple scattering the toroids are air gap with no return for the magnetic flux. This results in large fringe affects and very non-uniform magnetic field in both η and ϕ shown in Figure 4·6. An additional challenge of the toroidal configuration is the asymmetric acceptance for μ^+ and μ^- in the forward region.

The barrel toroid coils are 25.3 m long, with an inner diameter of 9.4 m and an outer diameter of 20.1 m. With a peak field of 3.9 T at the design current of 20.5 kA the barrel toroids have 1.08 GJ of stored energy. For the end-cap toroid the inner bore of the coils is 1.65 m and the outer bore 10.7 m. The field strength at nominal 20.5 kA current is 4.1 T giving each end-cap toroid 250 MJ of stored energy. The average bending power $\int Bdl$ for muons passing through the spectrometer is more than 2 T m in the barrel and 4 T m in the end-cap, however in transition region because the end-cap toroid is rotated and set between the barrel coils there are trajectories where $\int Bdl$ is extremely small, for $|\eta| \simeq 1.5$, as can be seen in Figure 4·6. In this region additional chambers are installed as the $\int Bdl$ may be zero but the $\int |Bdl| \neq 0$, due to the muon trajectories passing inside and outside of the coils in this region. Instrumenting this area of inflection allows measurement of the momentum despite $\int Bdl$ being close to zero.

4.7 Trigger System

In order to handle the high rate of LHC data the ATLAS trigger system has a three level system, designed to reduce the rate at each level with the goal of giving the next step in the chain more time to make a more detailed decision before passing the event along to the next step. In ATLAS the three distinct trigger levels are called: Level 1 (L1), Level 2 (L2), and the event filter (EF). The last two stages are L2 and EF are grouped together and refered to as the High Level Trigger (HLT), this distinction is made as the L1 trigger is implemented using custom built electronics while the HLT is software running on a dedicated computer farm.

The L1 trigger has 2.5 μs to make a decision to either keep or reject an event, in this time window only a limited amount of information from the whole detector is available. The timing is such that a hardware trigger system is built to find coincidences in hit patterns in the Muon Spectrometer and calorimeter towers matching specific thresholds. The maximum L1 rate feeding the L2 trigger is 75 kHz, known as the L1 bandwidth. At this rate the L2 trigger system can look at a limited amount of the ATLAS detector. The L1 trigger defines Regions of Interest (RoIs) by geometric location of L1 trigger objects and L2 uses these areas to look more closely at the event. The L2 trigger system further reduces the event rate to 3.5 kHz going into the EF using on average 40 ms to make a decision. In EF the full detector information is available not just the ROIs and a coarse version of the offline reconstruction algorithms are run. The EF reduces the event rate to the 200 Hz ATLAS accepts with an event processing time of 4 s on average.

Triggers are organzed by physics objects into trigger chains, jet, muon, electromagnetic, E_T^{miss} each chain having multiple $\mathrm{p_T}$ or energy thresholds. Trigger chains and thresholds have very different rates depending on the backgrounds and signals. In order to meet the bandwidth requirement and physics goals of the ATLAS experiment trigger threshholds are adjusted and triggers pre-scaled by keeping a fraction of the total accepts. The muon triggers have 6 different single muon $\mathrm{p_T}$ thresholds, and only the highest threshold, used by this analysis, is not prescaled. A detailed discussion of the muon triggers can be found in Chapter 5.

Chapter 5

The ATLAS Muon Spectrometer

5.1 Introduction

The Muon Spectrometer [15] is a magnetic spectrometer using a toroidal magnetic field and four separate detector technologies to reconstruct track momentum. As a muon passes through the magnetic field its momentum can be measured by measuring the radius of curvature R of the deflected path:

$$p \cos \lambda = 0.3 \ B \ R \tag{5.1}$$

for a track with pitch angle λ relative to the $\overrightarrow{B}$ [52]. Typically sagitta, the depth of the arc made by the track, is used instead of the radius of curvature to calculate momentum and resolution. The relationship between sagitta and momentum p in a uniform solenoid field B is:

$$s = \frac{0.0375 \ B \ l^2}{p} \tag{5.2}$$

where l is the arc length of the track in the magnetic field. Here the intrinsic resolution is:

$$\frac{\Delta p}{p} \simeq \frac{\Delta s}{s} \simeq \frac{0.27 \ p}{B \ l^2} \ \% \tag{5.3}$$

This is inversely proportional to the field strength and the square of the track length. Maximizing this length improves the resolution faster than increasing the field strength.

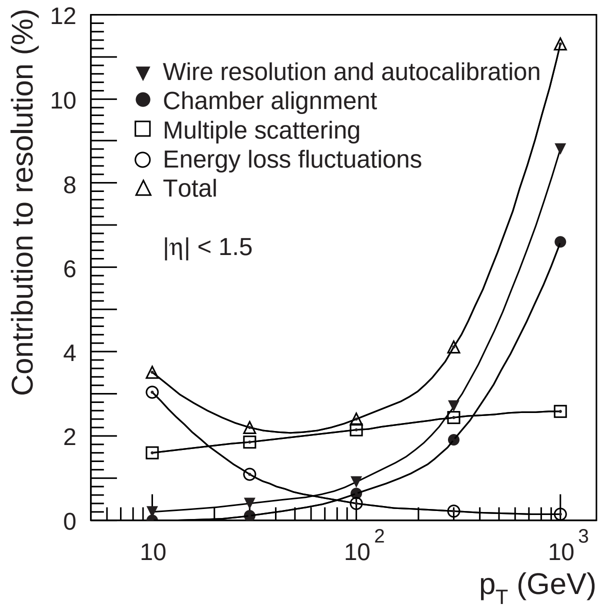

Figure 5·1: Contributions to the Muon Spectrometer momentum resolution averaged over η and ϕ in a standard sector, from Ref [14]

The factors contributing to momentum resolution as a function of momentum can be seen in Figure 5·1. At low-$\mathrm{p_T}$ less than about 20 GeV the energy loss fluctuations in the calorimeters are the dominant uncertainty. Then effects from multiple scattering in dead material dominates from around 20-200 GeV. Above 200 GeV the intrinsic chamber resolution and chamber to chamber alignment become the most important factors. At low momentum the Inner Detector provides a measurement of the momentum before the muon interacts with the calorimeters, to help with the resolution at low-p_T. To minimize the impact of multiple scattering an air core toroid configuration is used, along with an accurate description of the "dead" material in ATLAS to help determine where scattering might occur.

The design of the ATLAS Muon Spectrometer was driven by the physics goals of benchmark analyses covering muon $\mathrm{p_T}$ from ∼1 GeV to ∼1000 GeV. At low-$\mathrm{p_T}$ the performance is driven by the reconstruction and triggering of muons coming from b-quark jets, while at high-p_T the requirements come from the geometric acceptance of H→ $ZZ^* \rightarrow 4\mu$, and resolution on a 1 TeV Z'. The figure of merit is that the resolution of a 1 TeV p_T muon should be 10%. The high luminosity environment of the LHC presents additional challenges in design, coming from the high rate of muons, and additional spurious hits from background radiation. This causes difficulty in pattern recognition and the trigger rates, particularly at Level-1, where precision chamber information is not yet available.

5.2 Muon Spectrometer Layout

The Muon Spectrometer is the outermost sub-system of ATLAS and is the largest part of the detector by volume. The ATLAS Muon Spectrometer is a cylindrical magnetic spectrometer designed to have three layers of measurements with an air core toroidal magnetic field. Each layer has a precision chamber to give accurate measurements in the $r - z$ bend plane, and two layers have a fast response detector. The cylindrical muon system is composed of two main parts: a cylinder barrel section and two disk like end-cap systems. The toroid magnet is also organized into barrel and end-cap sections. The cut away view of one quarter of the detector can be seen in Figure 5·2. The Muon Spectrometer has a radius of 4.5 m to 11 m and extends from 7 m to 23 m away from the interaction point in the z direction along the beam pipe. The volume of the Muon Spectrometer is approximately 16,000 m^3 with a total of 1,076,000 read out channels.

Both the barrel and end-cap are composed of 16 phi sectors, alternating between larger and smaller sectors which overlap to have no projective cracks. To clearly illustrate the overlap of sectors in the barrel section Figure 5·3 shows a transverse view of the barrel. In the transition region between the barrel and the end-cap the diverging magnetic fields necessitate additional instrumentation. Precision chambers

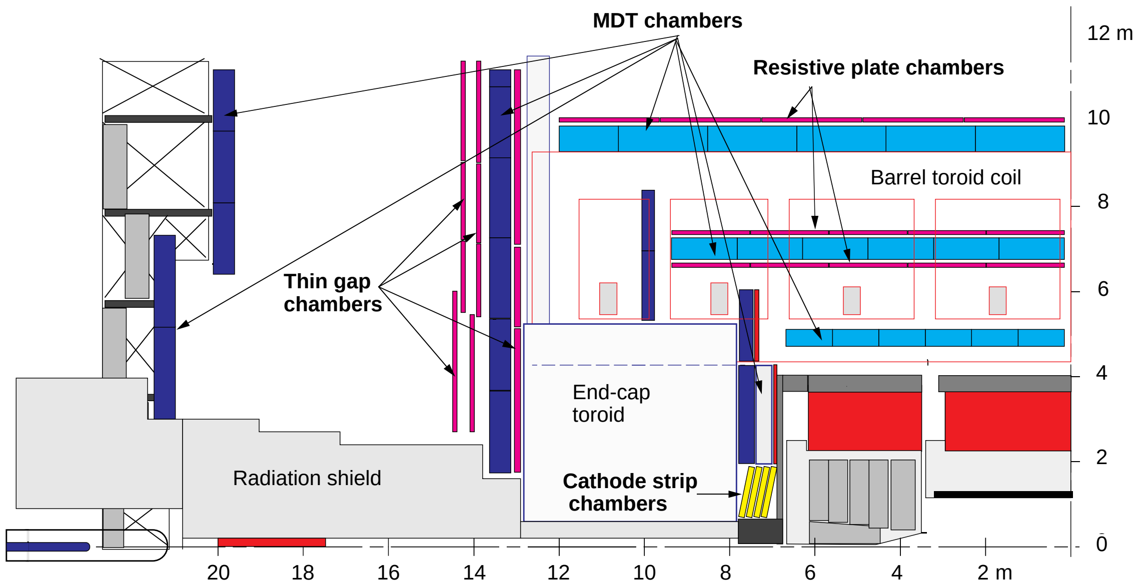

Figure 5·2: Side view of one quadrant of the ATLAS Muon Spectrometer, from Ref [15].

are installed to aid in the reconstruction of muon tracks.

The toroidal magnets create a field in this volume that ranges from 0.5 to 2 T. The chambers are arranged so that particles coming from the interaction point cross three layers of measurements called stations. The combined group of measurements for a station are fit into straight-line segments used for reconstructing tracks. The three positions of the stations are the inner field boundary, close to the maximum of the field, and at the outer field boundary. At $|\eta| > 1.4$ the cryostat of the end cap toroid magnet contains the maximums of the field and makes this impossible. A larger lever arm is instead used at the two outer stations to optimize the momentum measurement.

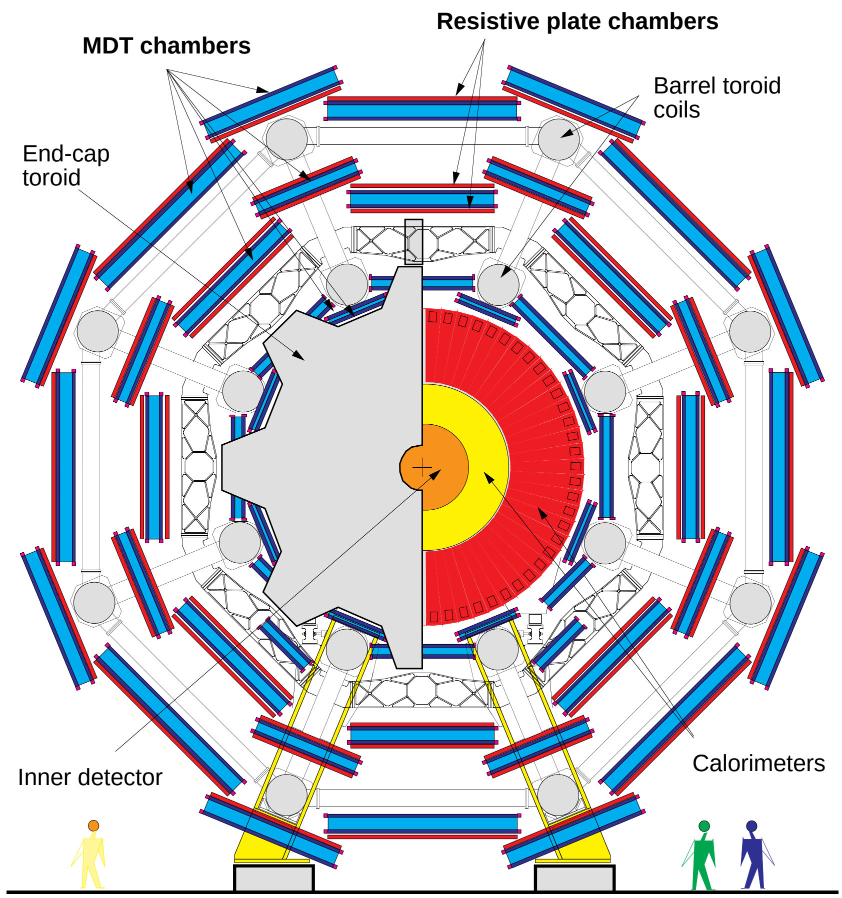

Figure 5·3: Transverse view of the ATLAS Muon Spectrometer, from Ref [15].

5.3 Fast Response Chambers

Triggering and ϕ coordinate measurements are handled by two separate detector technologies. In the barrel ($|\eta| \leq 1.05$) Resistive Plate Chambers (RPC) are used because of good spatial and time resolution as well as adequate rate capability. In the end-cap ($1.05 \leq \eta \leq 2.4$) Thin Gap Chambers (TGC) are installed to handle the higher rates of this more forward region.

5.3.1 Resistive Plate Chambers

The Resistive Plate Chambers are a gaseous parallel electrode-plate detector. Two resistive plates are kept parallel to each other at a distance of 2 mm by insulating spacers. An electric field is applied over this gap of 4.9 kV/mm so that when an ionizing particle passes through the $C_2H_2F_4$/Iso-C_4H_{10}/SF_6 gas (94.7/5/0.3) an avalanche of charge is deposited on the anode plates. This signal is read out via capacitive coupling to metallic strips mounted on the outer faces of the resistive plates. As RPCs have no wires, this makes the chambers less sensitive to small deviations from planarity, and simplifies their construction.

Each RPC unit is made of two gas volumes and four readout strip panels. The detector layers are interleaved with three support panels made of light-weight paper honeycomb and are held in position by a solid aluminum frame. The total thickness of an RPC unit is 96 mm.[1] The two units forming a chamber have an overlap region of 65 mm to avoid dead areas for curved tracks shown in Figure 5·4. Standard RPC chambers are divided into two segments along the ϕ direction with an 18 mm inefficient region in between due to the frames. Figure 5·4 contains a schematic of the chamber components and their arrangement for a single pad. The strips on one

[1]Except for the RPC paired to BOL chambers whose length requires additional support from an aluminum honeycomb that is 106 mm thick.

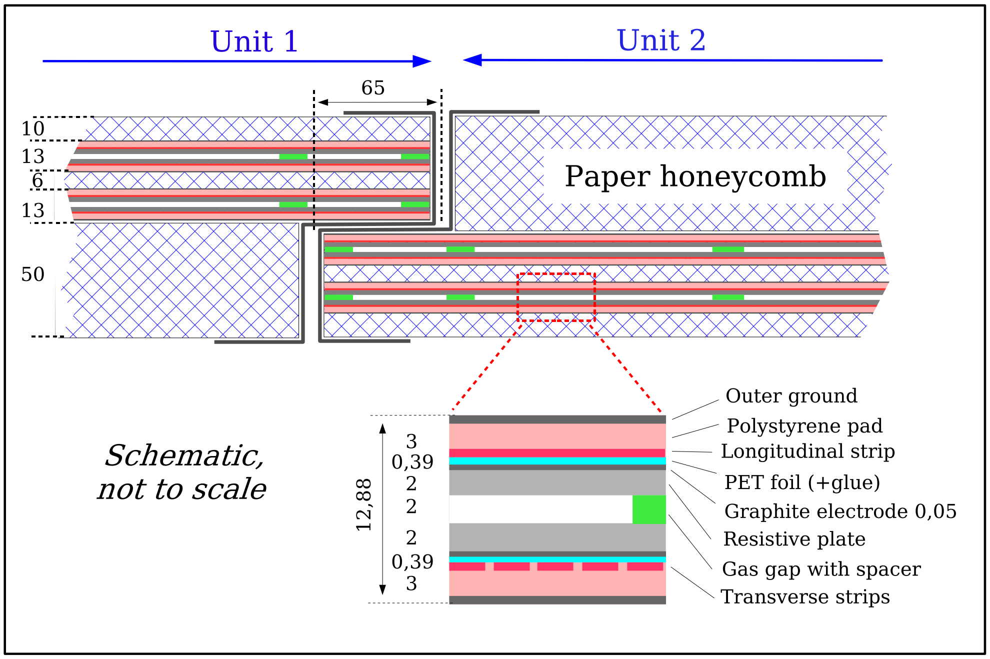

Figure 5·4: Cross section through an RPC where two units join to form a chamber including a detailed view of the chamber components, from Ref [3].

side of the gap are segmented in ϕ while on the other side they are segmented in η thus measuring both coordinates at once. Two RPC layers are mounted together to form a chamber, meaning each chamber gives two measurements of both η and ϕ. The readout-strip panels are also segmented in ϕ in order to get a homogeneous trigger scheme for all chamber types. This reduces the η-strips time jitter by a factor of two.

The RPCs are mechanically mounted to the barrel MDT chambers in the middle and outer stations. The middle MDT station chambers have two associated RPC chambers one below (RPC1) and one above (RPC2). For the outer station the RPCs are mounted on the interaction point side of the MDT (RPC3). The three layers of the RPC can be seen in Figure 5·17.

5.3.2 Thin Gap Chambers

The Thin Gap Chambers are multi-wire proportional chambers. The ATLAS TGCs have the characteristic that the wire-to-cathode distance of 1.4 mm is smaller than the wire-to-wire distance of 1.8 mm shown in Figure 5·5. The TGCs use a highly quenching gas mixture of CO_2 and n-C_5H_{12} to prevent streamers in the operating conditions. The high electric field around the TGC wires and the small wire-to-wire distance leads to very good timing resolution.

Only tracks at normal incidence passing equidistant between two wires have long drift times due to the vanishing electric field between the wires. In the TGC wheels, the angle of incidence for tracks from the interaction point always have an angle $\geq 10°$ so that some piece of the track will be outside the low field region. Including the variation of propagation time on wires and strips, signals arrive with 99% probability inside a window of 25 ns.

The TGC gas gaps are called "chambers" and combined in triplet and doublet

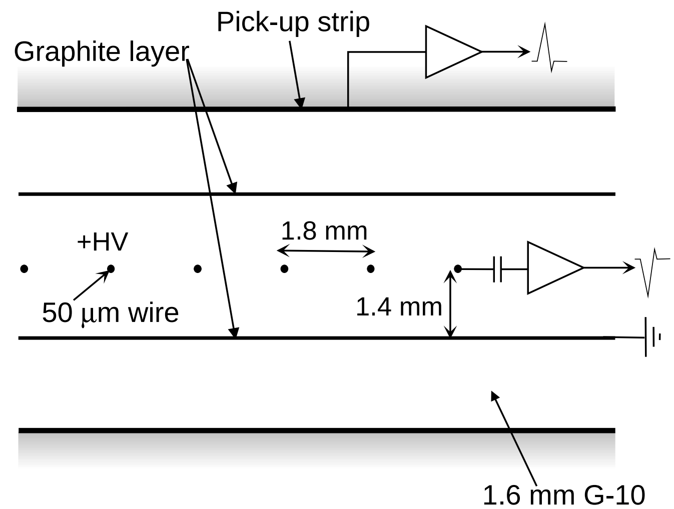

Figure 5·5: TGC cross section showing the anode wires, graphite cathodes, and signal strips orthogonal to the wires, from Ref [3].

configurations known as modules, shown in Figure 5·6. The location of these modules are in two stations shown in Figure 5·17 as one doublet paired with the MDT end-cap inner station and two doublets and a triplet in the middle station. The middle TGC layers are the only trigger detectors in the Muon Spectrometer end-cap and form circular disks made of concentric rings. All module's in the middle station are segmented into 12 sectors of 30° in the azimuthal direction, in contrast to the 16 sectors of MDTs.

5.4 Precision Chamber Design

Over the $|\eta| < 2.7$ covered by the Muon Spectrometer, the precision measurement of the sagitta is made by the Monitored Drift Tubes (MDT) with the exception of the inner most layer of the end cap. In the region of $2 < |\eta| < 2.7$ the measurement is made by Cathode Strip Chambers (CSCs).

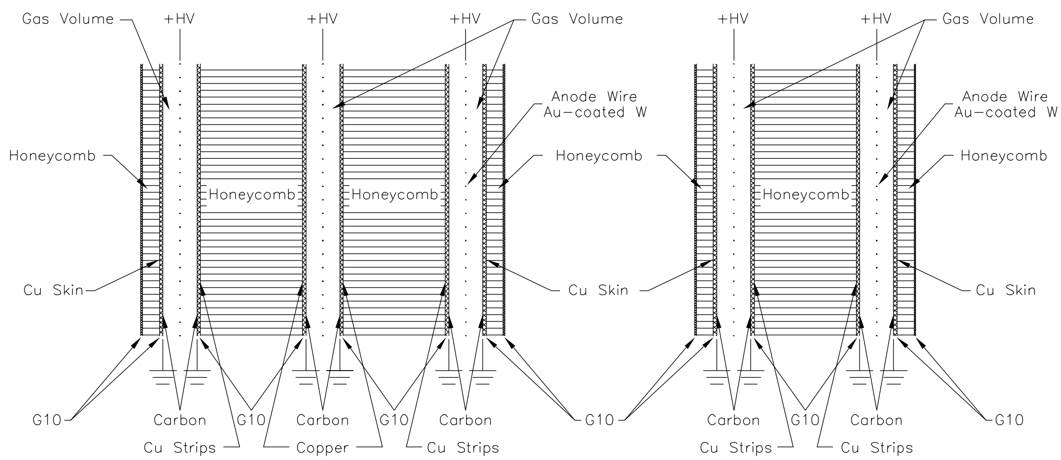

Figure 5·6: Cross section of a TGC triplet and doublet module. The triplet has three wire layers but only two strip layers. The schematic is not to scale, from Ref [3].

5.4.1 Cathode Strip Chambers

With the limits for operating MDT chambers at counting rates of roughly 150 Hz/cm^2 an alternative detector technology must be used at $|\eta| > 2$ in the inner most station, where this rate is exceeded. The ATLAS Muon Spectrometer compliments the MDTs with Cathode-strip chambers (CSC) which combine high spatial and time resolution with high rate capability and low sensitivity to neutrons. The CSCs are able to handle a counting rate up to 1000 Hz/cm^2, and are therefor used in the forward region of the detector $2 < |\eta| < 2.7$. The ATLAS CSCs are operated with an 80/20 mixture of Ar/CO_2 gas and 1.9 kV.

CSC chambers are trapezoidal in shape and divided into large and small chambers in the azimuthal angle, ϕ. The CSC chambers are in only the inner most layer of the end-cap the whole sub-detector consists of two rings of 16 chambers shown eight large and eight small in Figure 5·7. The CSC chambers experience a degradation in spatial resolution due to the Lorentz force on drifting electrons. To minimize this

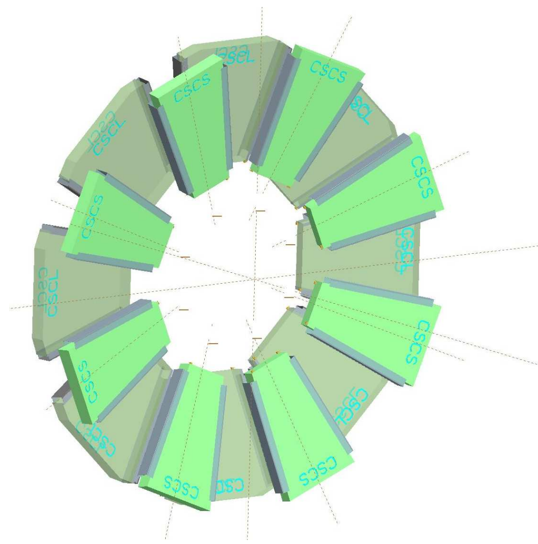

Figure 5·7: Layout of one CSC end-cap with eight small and eight large chambers, from Ref [3].

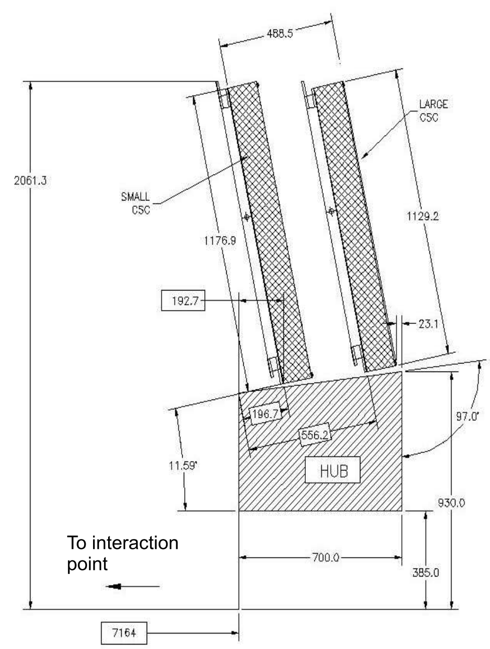

Figure 5·8: The inclination of the CSC chambers towards the interaction point, with dimensions in mm, from Ref [3].

effect the CSC chambers are inclined towards the interaction point such that a muon of infinite momentum would be normal to the CSCs. The 11.59° angle can be seen in Figure 5·8.

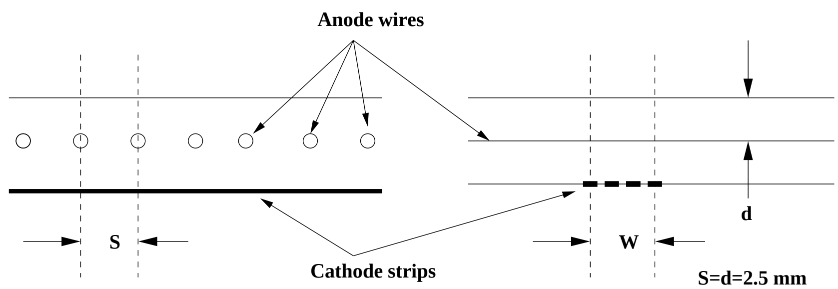

Figure 5·9: Structure of the CSC cells looking down the wires in the transverse coordinate on the left and perpendicular to the wires in the bending plane on the right, from Ref [3].

Each CSC chamber is made of four planes of CSC each independently providing measurements of both η and ϕ. Each of the four CSC planes are a multi-wire proportional chambers with the anode wire oriented in the radial direction. Both cathodes are segmented, one with strips perpendicular to the anode wires, and the other parallel Figure 5·9. This segmentation allows the CSCs to measure both the precision η and transverse ϕ coordinates at the same time. The charge from a shower is spread out over neighboring η-strips, and the actual position can be fit based on the charge deposited. In Figure 5·10 the cathode segmentation can be seen with a typical signal. Typically the charge from a track is spread over 3-5 strips, with width of 1.519 mm and 1.602 mm in the large and small sectors respectively. There is an inter-strip gap of 0.25 mm. To keep cost of readout electronics down the cathodes are readout as four strips with a pitch of 5.308 mm and 5.567 mm for large and small chambers.

The resolution of the CSCs is dominated by two factors. The first is electronic noise causing a reduction in the number of strips used in the clustering algorithm for

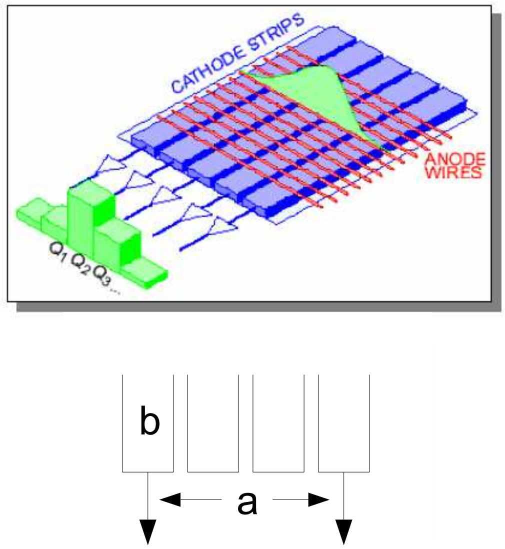

Figure 5·10: The segmentation of the CSC cathodes. A smooth green distribution on the anode wire is read out as the green blocks in the lower left. These can be interpolated to find the true position of the track, from Ref [3].

interpolation of the track position. For the ATLAS CSC geometry it was determined that the best results are obtained using three to five strips around the peak of the distribution. The second factor is the Lorentz angle mentioned previously, as the motivation for the 11.59° tilt towards the interaction point. The single layer resolution for the CSCs is rate dependent and ranges from 40 μm to a plateau of 65 μm over the range of muon fluxes 0-2 kHz/cm^2.

5.4.2 Monitored Drift Tube Chambers

The Monitored Drift Tube chambers (MDT) are proportional chambers constructed of high grade aluminum cylindrical tubes with an outer diameter of 29.970 mm, operating with an Ar/CO_2 gas mixture with a ratio of 93/7 at 3 bar pressure. The electrons resulting from ionization are collected at the central gold-plated tungsten-rhenium anode wire with a potential difference of 3080 V to the grounded tube wall.[2] The anode wire is held in position on either end by a cylindrical end-plug ensuring the position of the wire within a tube to an accuracy of $\sigma < 10\ \mu$m.[3] This

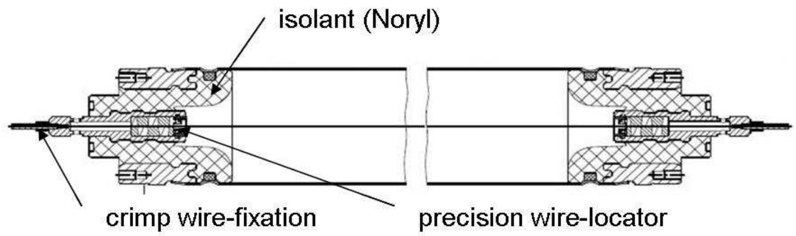

Figure 5·11: Longitudinal cut through an MDT tube, from Ref [3].

arrangement is shown in Figure 5·11.

When an ionizing particle passes through the active gas it causes the freed electrons to drift radially towards the anode wire. As illustrated in Figure 5·12 the electrons coming from the closest approach to the wire will have the shortest path to reach the anode as the drift electrons travel along the radial field lines. This field configuration makes the drift tubes relatively insensitive to the incidence angle between the track and the chamber plane. One down side to the cylindrical tube geometry is the long pulse train caused by all electrons not at freed at the distance of closest approach. These signals arrive over a fraction of the maximum drift time of 700 ns for electrons originating at the tube wall. The signal from the distance of closest approach to the wire is relevant for the tracking, shown as R_{min} in Figure 5·12. The MDTs use an adjustable dead time to the read out electronics to keep just the first signal and eliminate multiple hits.

Within a single MDT chamber, tubes are grouped together into two layers with the number of tubes varying by chamber type and location. In the middle and outer

[2] The diameter of the anode wire is 50 μm.

[3] The accuracy of the wire to wire position within a chamber was verified using X-ray microscopy on a random 10% subset of the installed chambers [3].

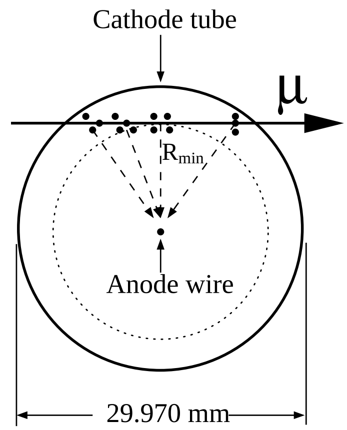

Figure 5·12: Cross-section of an MDT tube and fundamental operating principle, from Ref [3].

stations three, and in the inner four, rows of tubes are glued together to form a multi-layer, chambers are then constructed out of two multi-layers using aluminum spacer bars as frames, seen in Figure 5·13.[4] MDT chambers are rectangular in the barrel and trapezoidal in the end-cap. These geometries are chosen to minimize gaps in the coverage.

MDT Services

The sides of MDT chambers are referred to by where services are routed. One end of the tube has the 3080 V supplied to it and is labeled the High Voltage (HV) side. There are two HV lines per chamber, one for each multi-layer. The other side has the Mezzanine Cards (Mezz Cards) responsible for reading out 24 tubes, grouped together onto three Analog Shaper Discriminator (ASD) chips with eight tubes each. The signal coming out of the Mezz Cards is read out for a chamber by the Mother Board of which there is one per chamber. The handling of HV, low voltage (LV), and electronics configuration, known as slow control, of the chamber is also handled through the mother board, and the signal readout here is transferred to radiation

[4] The MDT chambers in the transition region known as the BEEs have only one multi-layer.

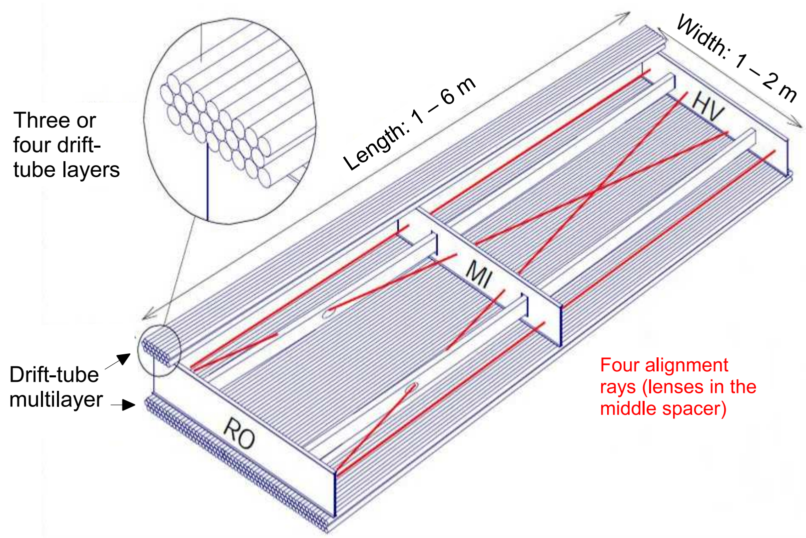

Figure 5·13: MDT Chamber schematic, from Ref [3].

hard fiber optic cables. These cables are collected in Read-out Devices (RODs) in the counting room. The gas for the MDT chambers is provided in parallel by a manifold designed to have approximately uniform flow rate, of roughly one volume per day, through each tube.

Hit Calibration

The MDT chambers read out a Time-to-Digital Converter (TDC) for the drift time and an Analog-to-Digital Converter (ADC) indicating the amount of charge collected in the first 18 ns. The TDC can be used to determine the distance of closest approach of the ionizing track to the wire. This is done by means of an r-t relationship. Shown in Figure 5·14 is an example of a TDC spectrum, and a time to distant an r-t relationship. Many different factors affect the r-t relationship, such as the tube minimum drift time t_0, the gas pressure, the temperature, water content of the gas, and variations in the voltage. The ADC can be used to discriminate real signal from electronics noise, and also if calibrated the relativistic γ of the incident particle. The

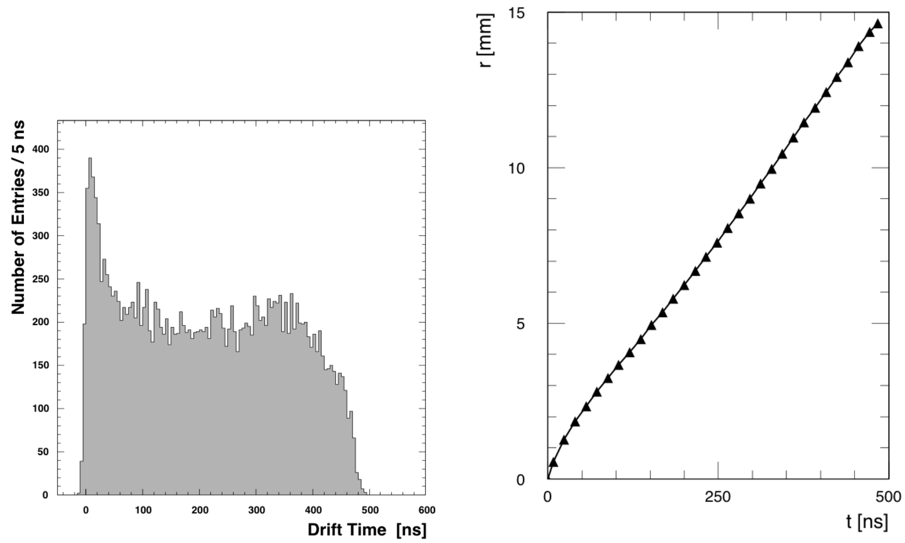

Figure 5·14: Shown on the left is a typical TDC spectrum for an MDT tube. On the right is the r-t relationship, from Ref [3]. The triangles are predictions from MC and the line is the auto-calibrated fit function, from Ref [3].

timing offsets are kept per tube in a database, and the temperature and pressure are monitored on the chambers with sensors. Installed on the surface above the ATLAS experimental cavern, is an MDT chamber with the first multi-layer having the gas entering the MDT gas system and the second multi-layer the gas exiting the cavern. Cosmic ray muons passing through this chamber are used to provide a global r-t function, which is corrected tube by tube for given the individual t_0, pressure, and temperature information.

5.5 Muon Spectrometer Transition Region

The ATLAS Muon Spectrometer has a complex toroidal configuration seen in Figure 4·5. In the bulk of the Muon Spectrometer an average bending power $\int B\ dl$ of well over 2 Tm is achieved, but in the transition region of $1.4 < |\eta| < 1.6$ the bending power can be as low as 0 Tm, Figure 4·6. This is not caused by the low

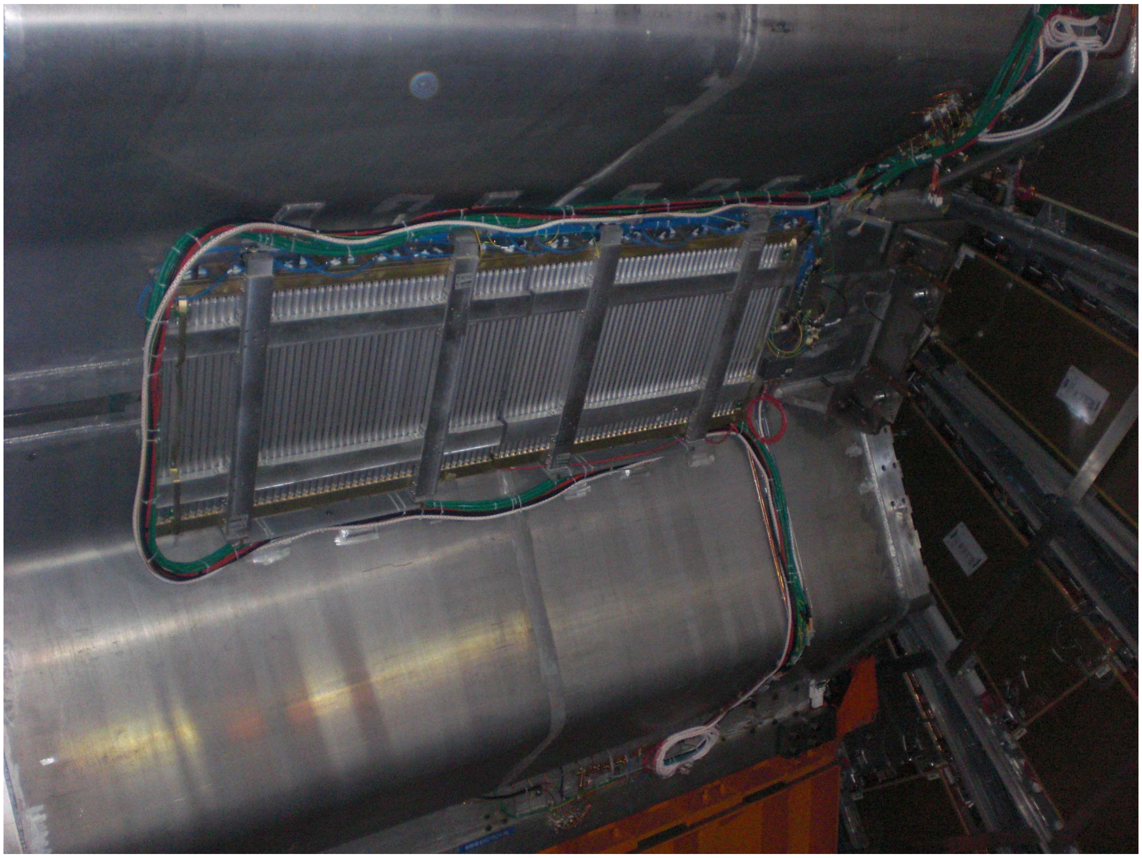

Figure 5·15: Photograph of the BEE chambers mounted on the end-cap Toroid cryostat between coils.

magnetic field but instead tracks traversing inside coils then outside through the return flux of either the end cap or barrel toroid or both. Additional chambers are installed in this area to instrument the region where total $\int B\ dl = 0$, and where only two stations would traversed. This is the motivation of the extra chambers or BEE (Barrel End-cap Extra), EEL (End-cap Extra Large), and EES (End-cap Extra Small) MDT chambers added into the design of the ATLAS Muon Spectrometer to improve muon coverage.

5.5.1 BEE Chambers

The BEE chambers are mechanically mounted to both end-cap toroid cryostats in the eight sectors between the coils, corresponding to the eight small MDT barrel sectors. One sector of BEEs can be seen in Figure 5·15. There are two chambers in a single sector, with the orientation of standard small barrel chambers. The BEE chambers consist of one four-tube multi-layer with 48 tubes in each tube layer for a total of 192 tubes per chamber. These two chambers are serviced by the same Chamber Service Module (CSM) electronics which handle slow control and readout of the chambers. In total on both A and C side there are 32 BEE chambers for a total of 6,144 tubes. The BEE tubes are 1.04 m in length and located 4.42 m radially from the beam pipe. Their position is known on the toroid housing to the precision of a few mm, the position of the toroid is monitored by the end-cap optical alignment system to far greater precision. The BEEs must be aligned by track based methods, however the complex magnetic field makes this difficult.

5.5.2 EE Chambers

The EE chambers have the orientation of an end-cap MDT chamber with two three tube layer multi-layers with 240 tubes. Two chambers in η form a ϕ sector. The large and small EE chambers overlap to form a ring inside of the barrel toroid coils located 11 m from the IP in z and 6 m in r. The chambers are mounted on precisely machined steel rails and slid into position, which is monitored by the EEs inclusion in the end-cap optical alignment system.[5]

[5] There are two chambers at $\phi = 90°$ on both A and C which are mounted to the the end-cap toroid chimney and moved by hand crank into position once the toroid is in place. They are not part of the optical alignment system and must be aligned by track based methods.

5.5.3 BEE Noise Problems

Due to unforeseen consequences caused by the delayed installation of the BEEs there was not time for adequate commissioning.[6] The BEE chambers suffered from high noise issues with many tubes with hit rates over 10 kHz and as high as 10 MHz making the BEE chambers unusable for quality data taking. The two main causes of noise in the MDT chambers come from faulty electronics producing fake signals, and interference from stray electromagnetic waves in the experimental cavern. With thousands of boards of electronics and power supplies the ATLAS detector hall is full of electromagnetic radiation at all frequencies. An oscilloscope analysis of the frequency and beat patterns determined that the sources of EM radiation are too numerous and broad band to be analytically countable. This resulted in the primary concerns being means for these stray signals to penetrate the BEE electronics and produce false signals. The cause of these signals are ground loops and long service cables acting as antennae. Also poor shielding on the chamber allowed the EM radiation to directly penetrate the Faraday cages and interact with the on-chamber electronics.

5.5.4 Noise Reduction

The first cause of noise, faulty electronics, can be handled by replacing the necessary parts when possible. It was determined all Mezzanine cards with over four noisy tubes should be replaced. This reduced the noise levels but not below the desired threshold leaving the second source of noise to be dealt with.

Using the ATLAS guide for grounding [53] a new grounding scheme, free of loops was devised. There are two methods to properly ground the sub-systems. The first is to ground everything, detector, electronics, power supplies, and mechanical

[6] The incident on September 19th 2008 allowed for unscheduled access to the detector and time to continue working on such existing issues.

structure to the same point of ground. The second is to leave everything electrically "floating" and have only one ground point.[7] The second method must be used for BEE chambers because they are mechanically mounted to the end-cap toroid cryostats which has a necessarily separate ground from the main ATLAS ground due to the quench protection system. The goal the second method is to control all the points where a chamber contacts ground and ensure that the lone ground of a chamber is at the power supply where it can be maintained. One consequence of this choice is each BEE chamber now forms a capacitor with the mechanical structure of the end-cap toroid cryostat, which have different potentials.

Each BEE chamber was checked to ensure that it was electrically isolated from the toroid housing and all other chambers. Sources checked were possibly broken rubber rings isolating the chamber mounts to the toroids, copper tubing used to pipe the MDT gas, and the aluminum plate the CSMs were mounted to. This was found to be a source for ground loops, isolating the service plate using G-10 greatly reduced noise levels. In addition to isolating the CSM plates, grounding wires were added to the mechanical frames, and Faraday cages of each chamber connecting to the CSM plates which were linked between sectors a "high quality" ground. This dedicated grounding wire connects BEE sector service plates to the power supply rack and the ATLAS common ground. Implementing this grounding scheme improved the noise rate.

The largest improvement in noise reduction came from adding ferrite cores to the LV cables, that provide power to the chamber electronics at 3.5 V. A factor of 100 improvement in the noise rate was achieved simply by adding ferrite rings around the LV wire at the power supply. The improvement is due to the long LV cables

[7]The middle station of the end-cap MDT system takes the first grounding system. Where the support structure and every potential grounding point are coupled to the main ATLAS common ground.

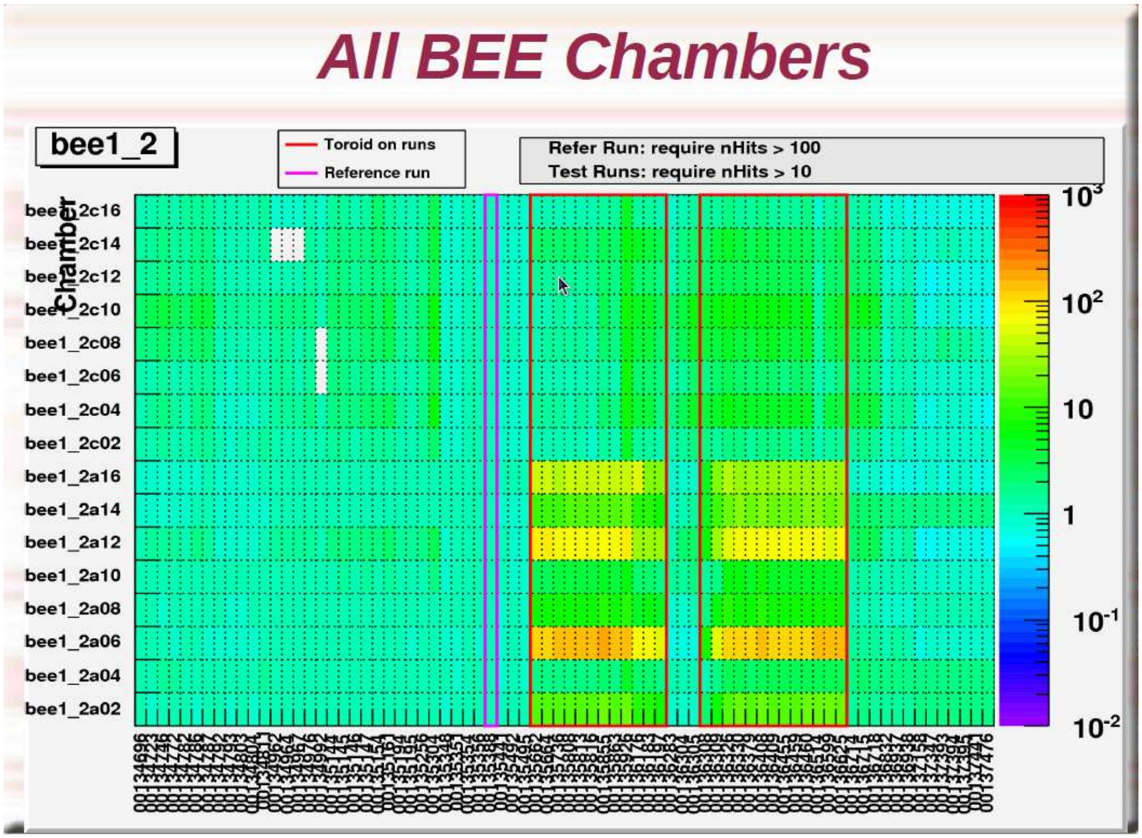

Figure 5·16: Shown here on the vertical axis is the BEE sector, the horizontal axis is the run number. The color of each bin is the noise rate calibrated to the run in the purple box. In the red box are the time periods when the toroids were on, from Ref [16].

which are more than 30 m in length and their roughly coaxial shape. The MDT LV cables consist of four insulated wires, two positive and two negative inside a grounded copper sheath. This copper must be pulled back and braided in order to ground the cable. This exposes a few cm depending on LV cable to the EM radiation. To avoid creating grounding loops the LV ground wires must be connected at the chamber service plate and not at the power supply. So the end of the LV cable closest to the power supply is actually furthest from the ground, putting a ferrite on this effectively damps harmful oscillations of this ground voltage.

These steps brought the noise rate in the BEEs well below the previously set limit of 10 kHz per chamber, until the toroids were turned on for data taking. At that point a B-field dependent behavior was observed [16]. Shown in Figure 5·16 is the relative noise rate calibrated to the runs in the purple box. The relative noise rate was seen to rise dramatically when the toroids were turned on in three sectors of the A-side BEEs. As can be seen the behavior was reproducible through power cycles of the magnets. When the magnets were off the BEEs return to being relatively quiet and then noisier when the magnets were on.

Eventually the problem was traced to the HV path. This was due to the Faraday cage surrounding the BEE HV hedgehog cards, which is penetrated directly by the HV cables, and clear visual line of sight of the electronics is possible, providing a direct path for electromagnetic interference. In the end-cap MDT chambers a "Bernie board" is used to bridge the inside and outside cables so that no outside signals are brought directly into the Faraday cage. To help with this, metal tape was placed over the holes in the three noisy sectors. In two sectors this removed the noise completely, however in one sector it increased the noise rate. The metal tape was removed in this sector and the noise rates measure to still be within the tolerable 10 kHz per tube average.

5.6 Muon Trigger and Data Acquisition System

The main goals of the Muon Spectrometer L1 trigger system are on a short time scale determine coarse muon transverse momentum, determine the bunch crossing identification of the event producing the muon track, and to determine Regions of Interest (RoI) to be passed as seeds to the HLT. These goals must be achieved at maximal efficiency while remaining insensitive to random hits and other noise in the experimental hall, over the full coverage of the Muon Spectrometer. There are considerable challenges for the muon trigger system, especially in the end-cap region where p_T can be up to 5.8 times larger than p but bending power is only twice that of the barrel. Furthermore, the radiation levels in the end-cap region reach a factor of ten higher than the barrel adding additional spurious hits that must be correctly handled. Finally, the trigger station for the end-cap is outside the field region and sees little curvature, with a lever arm of only 2 m between the triplet and second doublet of TGCs.

5.6.1 Muon Triggers

The Level-1 muon trigger system uses a system of fast coincidence "look up tables" between the three layers of the trigger chambers. Each coincidence pattern corresponds to a certain deviation from straightness, corresponding to a muon with infinite momentum. The deviation from straightness is proportional to the curvature of the track, or sagitta, which relates to the track's p_T. These coincidences are compared to predefined momentum thresholds to determine if the trigger has passed that threshold. Figure 5·17 shows the strategy in the barrel and end-cap where the deviation from straightness is shown as the shaded grey regions. In the end-cap the interaction point must be assumed as there is no trigger information from the inner station. This makes the L1 end-cap triggers extremely susceptible to non-muon backgrounds.

The line connecting the interaction point and the reference "pivot layer" defines the straight line. The other layer's hits determine the deviation from straightness. For the barrel the second layer RPC2 is the pivot plane and the final TGC layer TGC3 in the end-cap. All slopes are calculated relative to these pivot planes. For example in the barrel the low-p_T trigger compares the slope of the line connecting the hits of RPC2 and RPC1 with the slope of the line connecting the RPC2 hits

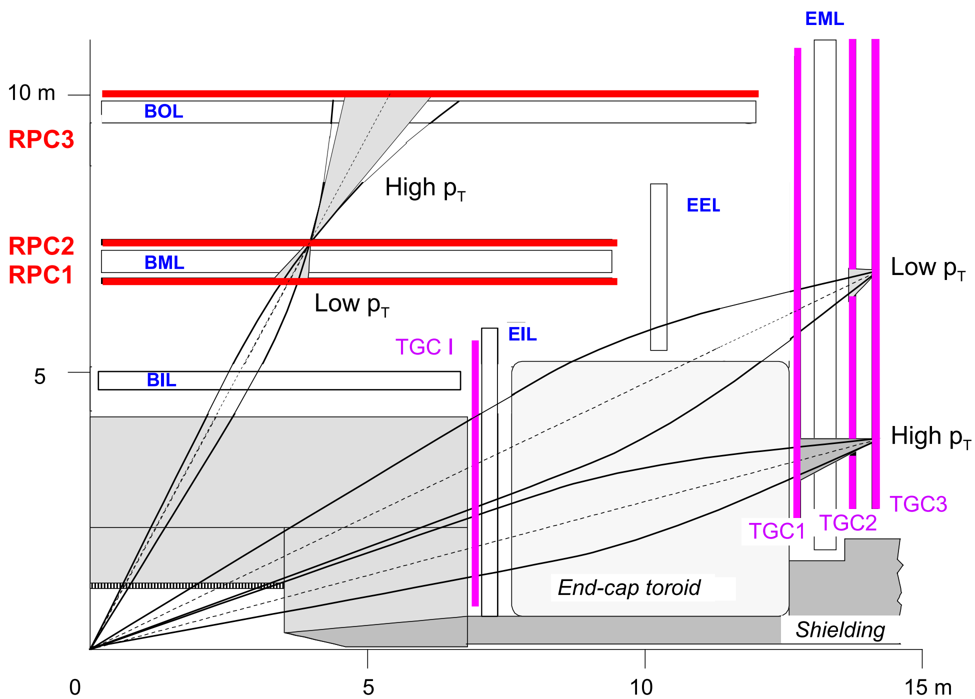

Figure 5·17: Longitudinal view of the Muon Spectrometer showing the Level 1 trigger scheme, requiring two layer coincidence for the low-p_T trigger and three layer for the high-p_T trigger. The layout of the RPC and TGC chambers is also illustrated in red and pink respectively, from Ref [3].

with the interaction point. And for the high-p_T trigger the slope is between the RPC3 and RPC2 hits compared with the line from RPC2 and the interaction point. Beyond determining what thresholds have been crossed the muon level-1 trigger uses these coincidences to define the regions of interest for the L2 trigger system. The L1 muon trigger logic has six independently programmable p_T thresholds that are checked in each region of interest.

The Level-1 muon trigger system sends its decision to the Central Trigger Processor (CTP), which can trigger an ATLAS-wide Level-1 accept. The Central Trigger Processor combines the information from the calorimeter triggers with the muon triggers to make the decision for an event. At Level-1 the Inner Detector information is not yet available. The interaction of the Level-1 muon triggers with the rest of the trigger system is shown in the block diagram of Figure 5·18. The information sent to the CTP is the number of bunch-crossings used to make the decision and the number of muons found passing each of the six p_T thresholds. Upon the event being accepted by the central trigger processor the muon trigger processors send geometric information to the Level-2 trigger as RoIs.

In ATLAS the Level-2 trigger is grouped with the third stage known as the Event Filter (EF) into the High Level Trigger (HLT). The majority of the HLT is handled by dedicated computing farms. The Level-2 muon triggers run specialized algorithms on the trigger roads that were defined by the Level-1 geometric RoI. The Level-2 trigger then combines the various RoI into one event object that is transmitted to the processor farm. Special Level-2 reconstruction algorithms are then run on these selected RoI with full detector information available in the RoI. The Level-2 trigger is designed to reduce the rate from the 75 kHz Level-1 output to 3.5 kHz, though this is scalable.

After the Level-2 trigger comes the Event Filter stage of the trigger. Here the

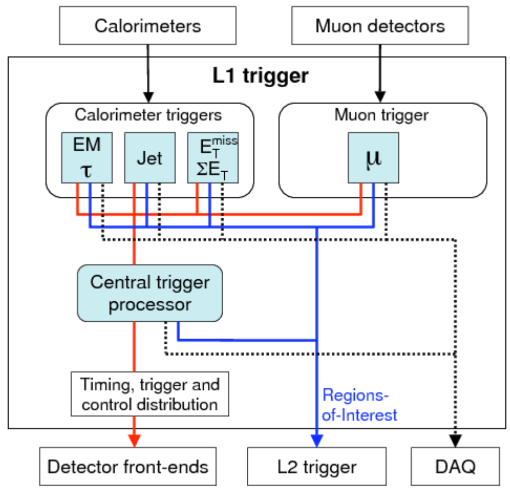

Figure 5·18: Block diagram of the L1 trigger. The paths to the detector front-ends, L2 trigger, and data acquisition system are shown from left to right in red, blue, and black respectively, from Ref [3].

whole detector has been read out and version of the full ATLAS reconstruction software is run on the entire detector not just the RoI, with preliminary calibration constants. The final calibration constants and other parameters necessary for full reconstruction have not yet been determined so the resolution is not as good as the offline reconstruction software. The Event Filter reduces the rate from 3.5 kHz to roughly 200 – 400 Hz that is saved for offline reconstruction.

5.6.2 Calibration and Alignment

ATLAS data runs are held for 24 hours before reconstruction so that necessary calibrations can be performed. The MDTs in particular are sensitive to temperature and pressure variations during the data taking period that are tracked and monitored by three separate calibration centers. These calibration centers determine run-by-run $r - t$ functions that relate the time an MDT signal is received to the radius of the track that passed through the tube.

As the ATLAS detector runs it is possible for small shifts in the position of the chambers to occur. With the strict tolerance on resolution the position of the precision chambers must be known to ≤ 30 μm during all data taking periods. It is therefore necessary to frequently monitor and update the position of the precision chambers. The alignment of the ATLAS Muon Spectrometer is accomplished by combining multiple techniques. The first is during chamber construction where systematic methods were used to ensure the uncertainty on wire-to-wire position is less than 10 μm in the MDTs. Second, two independent optical alignment systems have been mounted on the MDT chambers to monitor and update chamber positions and deformations during data taking periods. However, it was not possible to install the optical alignment system on all chambers, most notably all small sector chambers in the barrel, alignment using reconstructed tracks is necessary to provide alignment parameters for the uncovered chambers and as a cross check for the optical system.

A schematic representation of the optical alignment system in the large sectors is shown in Figure 5·19. In the barrel the large sectors chambers are instrumented to monitor the motion of the chamber relative to its neighbors in three coordinates. Using a separate system, in the end-cap chambers are instrumented to precision machined alignment bars. The relative positions of the alignment bars are monitored in three coordinates, Figure 5·19. In addition Figure 5·13 shows the internal alignment used to monitor the deformations of a single MDT chamber. The alignment bars installed on the inner most MDT chambers are also used to align the CSCs.

As mentioned previously the small MDT chambers in the barrel are not aligned with projective lines and must be aligned with tracks. Multiple software algorithms have been developed to accomplish this task, using straight tracks as “pseudo” sensors, filling and inverting a large Hessian matrix using track parameters, and finding the minimum of track fit χ^2s by shifting chamber positions and re-fitting the track

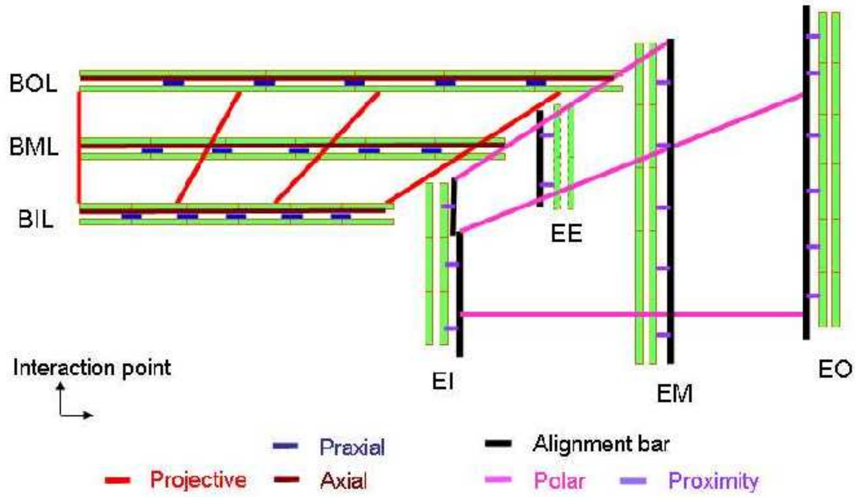

Figure 5·19: Principle of the optical alignment system for the ATLAS Muon Spectrometer, from Ref [3].

to determine the most likely position. The impact of chamber mis-alignment is discussed in the next Chapter 6. The alignment is not yet at its ideal level and this mis-alignment is taken into account as a smearing on the reconstructed muon p_T.

Chapter 6

Performance of Reconstructed ATLAS Muons

6.1 Finding and Identifying Muons

When muons pass through the ATLAS Muons Spectrometer [15], curving in the toroidal magnetic field, spatial points are measured as detector hits that can be used to reconstruct the momentum of the muon in the detector. In physics analyses the goal is to understand the hard scatter interaction that took place inside the beam pipe between the protons. To do this the detector response to muons is reconstructed into series of spatial points or hits, that are used to form small straight track segments. Segments are used to help fit larger curving tracks which measure momentum, these tracks are then extrapolated to the beam line to determine the muon properties at the interaction point. It is necessary to be able to distinguish muons from backgrounds and where possible remove their contribution to our sample. The main reducible sources of backgrounds are cosmic ray muons, beam halo, non-prompt or decay in-flight which can be non-isolated or collinear with other hadronic activity.

6.1.1 Reconstructing Muons

After the events have been recorded and calibrated the data is passed to the reconstruction software. The role of the reconstruction software is to take the detector response and create physics objects used in analyses. As muons leave hits in the tracking volumes of the Inner Detector and Muon Spectrometer, along with deposits of minimum ionizing energy in the calorimeters, muon tracks are relatively clean to reconstruct. In the Muon Spectrometer the hits of each muon station are grouped and fit into straight line segments, before being reconstructed as a single track passing through the whole Muon Spectrometer. The track is then combined with an Inner Detector track and extrapolated to the primary vertex.

The first step in track reconstruction is pattern recognition. A decision must be made as to which hits should be fit to form a segment. In the Muon Spectrometer a Hough Transform [54] is used searching in both the $r-z$ plane for η-patterns and the $x-y$ plane for ϕ-patterns. The MDT hits in a single chamber identified in the η-pattern finding are fed into a segment fitting algorithm.

Starting with the two outermost hits the four possible tangent lines are compared with the other hits in the chamber using hits within 1.5 mm in a linear fit for the segment of a chamber. If the segment χ^2/N_{dof} is larger than 10 the hit with the largest χ^2 is removed, and the segment re-fit. This process is repeated until the segment χ^2/N_{dof} is less than ten. At this point the ϕ-pattern information is used to associate the RPC, TGC, and CSC ϕ-hits to the segment. Figure 6·1 shows a schematic view of the process of segment fitting. The MDT tubes are outlined in light gray with the hits shown as filled in circles. The four possible segments formed from the tangent lines of the outermost hits are shown as dashed lines and the black hits and lines are the final segments and associated hits.

The resultant segments may contain ambiguities, as it is possible for a given η-pattern to have multiple segments with χ^2 less than ten. The decision on which is the true or correct segment is made by keeping the best segment as ordered by $\chi^2/ndof$, the number of hits on the segments, the sum of the number of out of time hits, delta ray hits, and holes. The four categories of MDT hits, true hits, delta

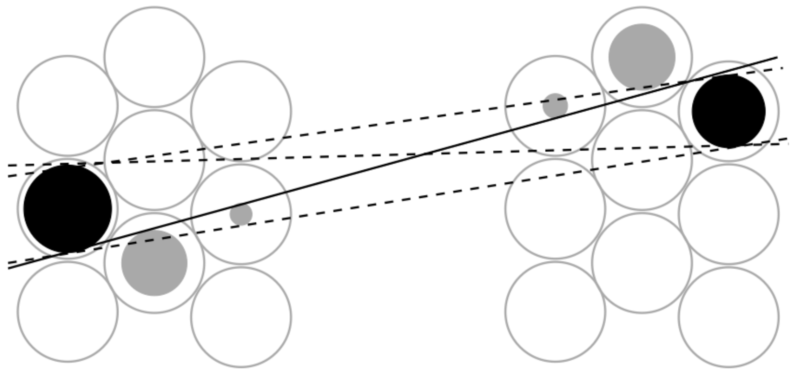

Figure 6·1: Diagram showing MDT tubes, light gray circles, with hits shown as filled in circles. The potential segment lines are the black dashed lines with the selected segment the solid line. Here the black filled in circles are hits that seeded the segment finding, from Ref [17].

rays, out of time, and holes can be seen in Figure 6·2. A hit on segment is a hit where the drift circle and segment are close to tangent and it can be used as a good measurement. Delta rays occur when the muon transfers sufficient momentum to an electron such that it can ionize the gas. When this Delta electron travels closer to the wire the time measured will be due to the electron and not the muon track, making the drift circles appear too small. Hits that are too large are either poorly calibrated or out of time and should not be used. The final category of hits are holes, holes come from MDT tubes crossed by the muon, where no hit was recorded. This is due to the high but not 100% per tube efficiency of an MDT chamber.

Next the segments associated with an η-pattern are combined into a track candidate. Seeding the track fit with the outermost segment and extrapolating in to all middle and inner segments still associated with the η-pattern track candidates are fit. The track candidates are again ranked by χ^2/N_{dof}, number, and type of hits. Hits that appear on multiple segments are assigned to the segment with the highest ranking. At this stage the tracks are re-fit with the full geometry description and magnetic field map, generating the final muon spectrometer track fit. In the Inner

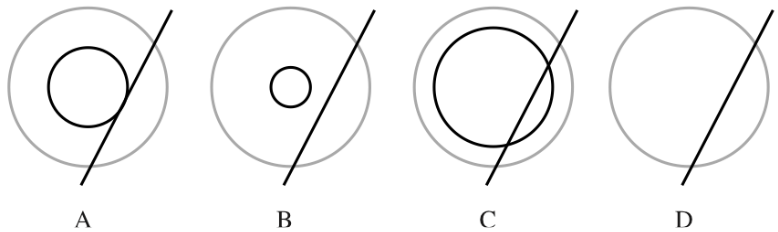

Figure 6·2: Diagram showing the four different types of hits in MDT tubes. **A** is a hit on a track, **B** is a delta ray, **C** is an out-of-time hit, and **D** is a hole, from Ref [17].

Detector track fitting is handled by either a global χ^2 fitter [55] or Kalman Filter based fitter [56].

To combine tracks found in the Inner Detector and those found in the Muon Spectrometer, the reconstruction algorithms extrapolate the track from the Muon Spectrometer to the Inner Detector volume to test the combination using a χ^2_{match} defined as:

$$\chi^2_{match} = (T_{MS} - T_{ID})^T (C_{MS} + C_{ID})^{-1} (T_{MS} - T_{ID}) \tag{6.1}$$

where the T's are the vector of track parameters consisting of the local position, polar angle, azimuthal angle, and charge over momentum of the track, and the C's are the covariance matrices. Once a decision has been made that the track is a combined track the new track parameters are determined. A re-fit starting in the Inner Detector using the Muon Spectrometer track parameters gives the final result of a combined track. These parameters are then extrapolated to the beam line where their values are reported to be used in analyses.

6.1.2 Track Resolution

The main challenges in accurately reconstructing muon momenta are energy loss fluctuations, multiple scattering, intrinsic resolution, and alignment. Shown in Fig-

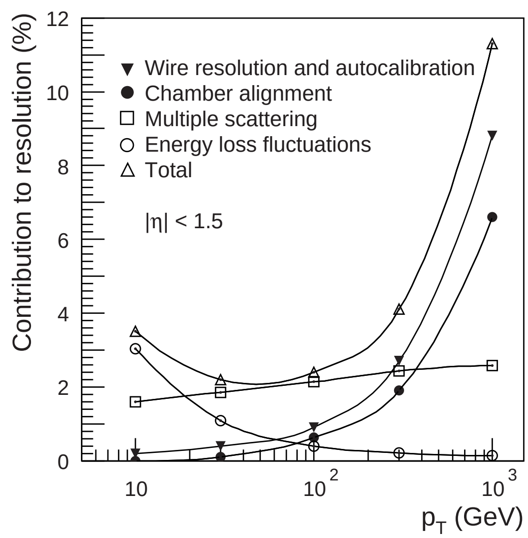

Figure 6·3: Contributions to muon p_T resolution as a function of p_T, from Ref [15].

ure 6·3 are these contributions as a function of p_T. At low-p_T the largest contribution to resolution comes from the muon energy loss in the calorimeters and dead material. There are three sources of muon energy loss, ionization, bremsstrahlung, and electron pair production.

$$\left(\frac{dE}{ds}\right)_{total} = \left(\frac{dE}{ds}\right)_{ion} + \left(\frac{dE}{ds}\right)_{brem} + \left(\frac{dE}{ds}\right)_{pair} \tag{6.2}$$

The ionization of a particle traveling through a material with known properties is described by the Bethe-Bloch formula [57]:

$$\left(\frac{dE}{ds}\right)_{ion} = -Kz^2\frac{Z\rho}{A\beta^2}\left(\frac{1}{2}\ln\frac{2m_e\beta^2\gamma^2E_{max}}{I^2} - \beta^2 - \ln\frac{28.8\sqrt{\rho Z/A}}{I} + \ln\beta\gamma - \frac{1}{2}\right) \tag{6.3}$$

where s is the path length, K is a constant, z is the charge of the particle, in this case the muon. The standard relativistic β and γ are used, along with the mass of an electron m_e, and the maximum amount of energy that can be transferred to an electron E_{max}. Finally the properties of the material being traversed, ρ the density, I the mean ionization energy, Z the atomic number, and A the atomic weight.

The mean energy loss from bremsstrahlung radiation for a muon is given by the Bethe-Heitler formula [58]:

$$\left(\frac{dE}{ds}\right)_{brem} = -\frac{E}{X_0}\left(\frac{m_e}{m_\mu}\right)^2 \tag{6.4}$$

where E is the energy of the muon, and X_0 the radiation length of the material. The mean energy loss from pair production and photo-nuclear interactions of muons with matter is parameterized as a function of $\frac{E}{X_0}$ as a third degree polynomial below 1 TeV and a linear function above 1 TeV [59, 60]. For muons in iron, the contributions from bremsstrahlung and pair production become important at momenta above a few hundred GeV as those contributions steeply rise and the ionization stays comparatively flat.

The amount of material traversed by a muon passing through the ATLAS detector is very dependent on the η, ϕ, and p_T of the muon. This makes the amount of energy lost by a muon η, ϕ, and p_T dependent. The mean expected energy loss for muons in just the calorimeters ranges from 2.5 - 8 GeV. In the reconstruction software, if a cluster in the calorimeter is found on the track that measurement is used to correct the muon energy. If no energy deposit is found an estimate based on a parameterized version of Equation 6.2 is used to correct the track parameters during the extrapolation.

At 20 - 30 GeV, as shown in Figure 6·3, the affects of multiple scattering start to dominate the resolution. Multiple scattering refers to the process by which particles traversing material undergoes multiple small angle deflections due to Coulomb interactions. Multiple scattering introduces real deflections in the particle trajectory not associated with bending in the magnetic field, degrading resolution. Multiple scattering is a stochastic process resulting in a Gaussian distribution with a mean value of zero. The width of the Gaussian can be found, on the polar angle in mrad, by using the Highland scattering formula [61]:

$$\sigma_{scat} = \frac{13.6}{\beta cp}\sqrt{\frac{s}{X_0}}\left(1 + 0.038\ \ln\frac{s}{\beta^2 X_0}\right). \tag{6.5}$$

This formula assumes that the change to the magnitude of a particle's momentum due to multiple scattering is negligible. The width, σ_{scat}, directly adds an uncertainty to the θ track parameter in the covariance matrix. In order to account for this affect in the reconstruction algorithm add "scattering centers"' to the track wherever it passes through matter. These scattering centers contribute to the total χ^2 as $\sim \theta^2_{scat}$. The preferred solution is to have the scattering centers only contribute to the track when the improvement to the χ^2 from the hits is greater than the increase in angle.

As can be seen in Figure 6·3, multiple scattering dominates the resolution from $\sim$ 30 GeV up to $\sim$ 200 GeV. Above this p_T the detector affects due to intrinsic resolution, calibration, and mis-alignment dominate. These affects were discussed in detail in Chapter 5.

6.2 Muon Resolution

Two methods were used for this analysis to test that the muon resolution was well understood. They were comparing the width of the J/ψ and Z resonances in data with MC, and independently comparing the orthogonal measurements provided by the Inner Detector and Muon Spectrometer. In both cases the resolution is studied as a function of both p_T and η. The studies were performed using the 2010 dataset and again using the first month of the 2011 dataset, then cross checked with the second month of the 2011 dataset. It was shown that the results were stable and not dependent on instantaneous luminosity.

It is known that the MC geometry used to describe the ATLAS detector underestimates the mis-alignment observed for the Muon Spectrometer. Furthermore the calibration of the data has not yet reached the ideal and optimized configuration. In order to account for this discrepancy an additional uncertainty is introduced by "smearing" the muon $\mathrm{p_T}$. For both the Inner Detector and Muon Spectrometer resolution parameters are determined as a function of η. The combined track uses a weighted combination of smearing parameters determined for both Inner Detector and Muon Spectrometer tracks. The combined $\mathrm{p_T}'(CB)$ is given by:

$$\mathrm{p_T}'(CB) = \frac{\frac{\mathrm{p_T}'(ID)}{\sigma_{ID}^2} + \frac{\mathrm{p_T}'(MS)}{\sigma_{MS}^2}}{\frac{1}{\sigma_{ID}^2} + \frac{1}{\sigma_{MS}^2}} \tag{6.6}$$

where

$$\begin{aligned} \mathrm{p_T}'(MS) &= \mathrm{p_T}(MS) \times (1 + \Delta(MS)) \\ \mathrm{p_T}'(ID) &= \mathrm{p_T}(ID) \times (1 + \Delta(ID)) \end{aligned} \tag{6.7}$$

and

$$\begin{aligned} \Delta(MS) &= f(0,1) \times \Delta p_1^{MS} + f(0,1) \times \Delta p_2^{MS} \times \mathrm{p_T} \\ \Delta(ID) &= g(0,1) \times \Delta p_2^{ID} \times \mathrm{p_T} \quad \text{for} \quad (|\eta| < 1.9) \\ \Delta(ID) &= h(0,1) \times \Delta p_2^{ID} \times \mathrm{p_T}/\tan^2(\theta) \quad \text{for} \quad (|\eta| > 1.9) \end{aligned} \tag{6.8}$$

Here $f(0,1)$, $g(0,1)$, and $h(0,1)$ are normally distributed random numbers centered at zero, with each a different random number. The smearing constants Δp_1^{MS}, Δp_2^{MS}, and Δp_2^{ID} are determined by data and MC comparisons using a fit to the $\mathrm{p_T}$ from W events, and fits to the J/ψ and Z peaks [62]. These fit values are constrained by alignment studies performed with cosmic rays, and straight track data taken with the toroid magnetic field off. The corrections Δp_1^{MS}, Δp_2^{MS}, and Δp_2^{ID} are used by all ATLAS physics analyses using muons.

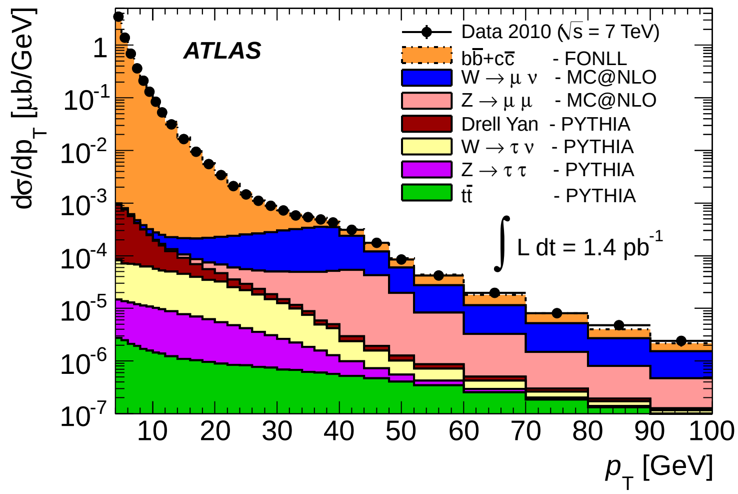

Figure 6·4: Inclusive muon spectrum in 2010 data shown as black points, and the physics processes from MC in filled in histograms, from Ref. [18].

6.3 Dimuon Resolution

One test that the muon spectrometer performance is well understood is the inclusive muon p_T spectrum. Shown in Figure 6·4, over the six decades of the plot the muon p_T agrees with MC, which include many different physics processes [18]. The Figure 6·5 plots are the difference in muon p_T, for two p_T slices, as measured by the Inner Detector and Muon Spectrometer in 2010 data. The contributions from prompt and non-prompt muons are scaled to fit the data [18] and show good agreement. The width of the MC and data matches well, indicating that the resolution of ATLAS muons is well understood at these p_T.

The resolution for muons with p_T below 100 GeV can be calibrated well using data driven techniques, but at higher p_T one must extrapolate the resolution. The dimuon resolution as a function of a resonance mass in smeared MC, can be seen in Figure 6·6. Here the reconstructed invariant mass of Sequential Standard Model Z' signals spaced 40 GeV apart were fit to a Breit-Wigner convoluted with a Gaussian.

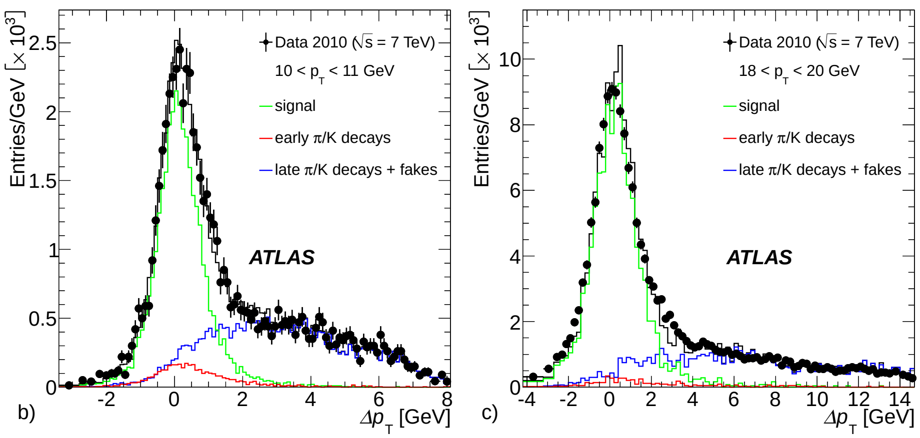

Figure 6·5: Plot of difference in p_T as measured by the ATLAS Inner Detector and Muon Spectrometer for an inclusive muon sample in from 2010 collisions data in black points, for two different p_T bins. The sources of the muons are shown as open histograms, showing good agreement, from Ref [18].

The width of the Breit-Wigner was constrained to be within 1% of the intrinsic MC simulation width, shown in red. The width of the Gaussian dimuon mass resolution is then plotted as the green points which are fit well by a quadratic function shown in black. Shifting the smearing parameters up or down one sigma and re-fitting gives the dashed grey line. Over the region of highest interest for Low-scale technicolor signal, 200 GeV – 1000 GeV, the resolution varies from 3% to 9%.

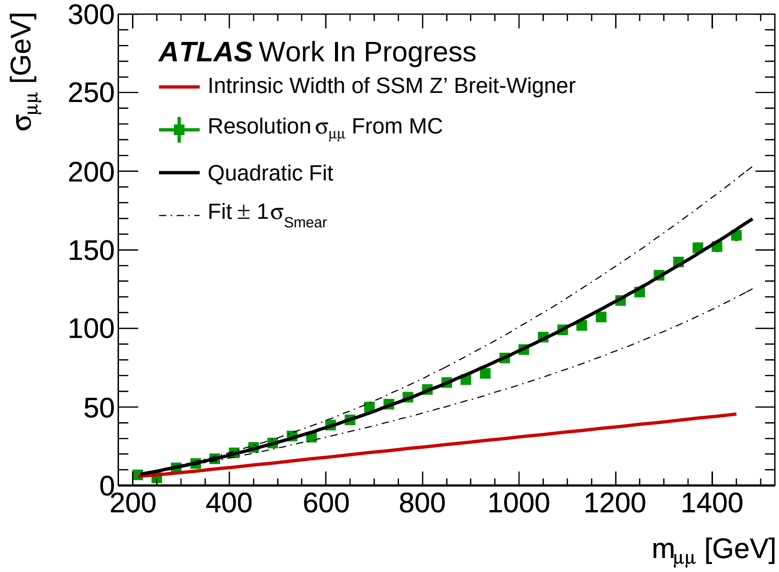

Figure 6·6: Plot of dimuon resolution as a function of SSM Z' mass. Shown in red is the intrinsic width of the SSM Z' resonance, and the dashed lines are the resolution when shifting the muon smearing parameters up or down one sigma.

Chapter 7

Dimuon Search for Technihadrons

7.1 Analysis Overview

A search for the technihadrons ρ_T/ω_T decaying to dimuons is performed in 1.21 $\text{fb}^{-1}$of $\sqrt{s} = 7$ TeV pp data by analyzing the steeply falling dilepton continuum to look for new narrow resonances. The consistency of the data with MC predictions of Standard Model backgrounds is checked in the dimuon invariant mass spectrum above 130 GeV. In the absence of a significant excess, 95% confidence level limits will be set on the Low-scale technicolor $m(\rho_T/\omega_T) - m(\pi_T)$ parameter space. This same technique is applied to searches for other new exotic particles such as spin-1 Z' and spin-2 Gravitons [5]. In the end limits can be set on all of these theories.

To reduce systematic uncertainties the search region is normalized to the Z peak. Using this normalization to a well known Standard Model "standard candle" process cancels mass independent systematics, while introducing a new 5% uncertainty on the measured dimuon cross section at high mass. The analysis uses signal shape information to improve sensitivity. These signal "templates" used to determine the signal significance and excluded masses were Sequential Standard Model Z' (SSM Z') [63–65]. The SSM Z' resonances have a broader intrinsic width than the ρ_T/ω_T, but over the range of 200 – 1000 GeV the dimuon mass resolution dominates the width of a potential signal.[1]

[1] This is shown in Chapter 6 in Figure 6·6.

7.2 Dataset and Monte Carlo

7.2.1 Dataset

The data sample used for this analysis was collected by ATLAS from March-July, 2011. The full recorded luminosity corresponds to 1.24 fb^{-1}, once detector quality selections and the 22 GeV single muon trigger are applied this results in the 1.21 fb^{-1}used for the analysis.

7.2.2 Monte Carlo

The hard scatter and hadronization of particles in the Monte Carlo(MC) datasets were simulated using a number of different software packages. The distribution of constituent particles inside the proton is modeled by the PDFs. These PDFs can be of many different orders of perturbation theory, and the like order is chosen to match that of the software simulating the hard scatter. The hard scatter is handled by the event generator and is typically leading-order (LO) in perturbation theory. The event generator produces a list of particles called the event record that can be hadronized. Hadronization is the name given to the step of MC generation where quarks and gluons form hadrons through QCD interactions. The hadronization is handled by PYTHIA, and HERWIG [66,67]. The particles coming out of this stage are those that interact with the material of the detector, which is modeled by GEANT [68]. The interaction of these particles is then turned a detector response and reconstructed using the ATLAS software ATHENA [69]. Further, the decay of tau leptons is done by dedicated software called TAUOLA [70]. At higher order the protons can radiate either before or after the hard scatter, this process called Initial State Radiate (ISR) if it takes place before the hard scatter or Final State Radiation(FSR) if it takes place after, is handled by PHOTOS [71]. Table 7.1 lists the MC background processes, the generation software, PDF, what order the cross section is corrected to, and the fraction of events due to that process in the search region above 130 GeV in dimuon invariant mass.

Table 7.1: Table showing MC datasets used in the search for technihadrons analysis, with event generators, PDFs, k-factor corrections, and relative contributions to the search region.

Sample	Generator	PDF	Correction	Contribution (%)
Drell-Yan	PYTHIA [49]	MRSTLO* [72]	NNLO	90.7
$t\bar{t}$	MC@NLO [73]+JIMMY [74]+HERWIG [66,67]	CTEQ6.6 [75]	LO	6.7
Diboson	HERWIG [66,67]	CTEQ6L1 [75]	NLO	2.5
W+jets	ALPGEN [76]+JIMMY [74]+HERWIG [66,67]	CTEQ6L1 [75]	LO	0.006
QCD			DATA	0.02

K-factors

In general the cross sections and event kinematics from are simulated using leading-order (LO) matrix elements and PDFs. These are then corrected to next-to-leading-order (NLO) or next-to-next-to-leading-order(NNLO) whenever possible by normalizing the LO cross sections to the NLO(NNLO) cross sections calculated using dedicated software. This technique is typically referred to as applying k-factors. There is an assumption that in going from LO to NNLO or NLO there is little change in the kinematic distributions, so the acceptance of the process will not change, and only the event weight, cross section, changes. Figure 7.2.2 shows the k-factors as a function of dilepton invariant mass, for QCD, EW, and the full QCD times EW correction. The QCD correction at NLO takes into account physics process where an additional color particle is radiated, at NNLO are loops of colored particles. The NLO EW correction takes into account processes where a W or Z boson is radiated in the initial or final state, before or after the hard scatter. The NNLO EW correction includes loops of EW bosons in the cross section calculation, and initial and final state photon radiation but not W or Z boson radiation. The full correction take both EW and QCD corrections into account, however assumptions must be made particularly about couplings to the EW gauge bosons, which make the correction model dependent. Therefore corrections to the SM Drell-Yan process are corrected for both QCD and EW processes but the technicolor signal sample has only the QCD correction applied.

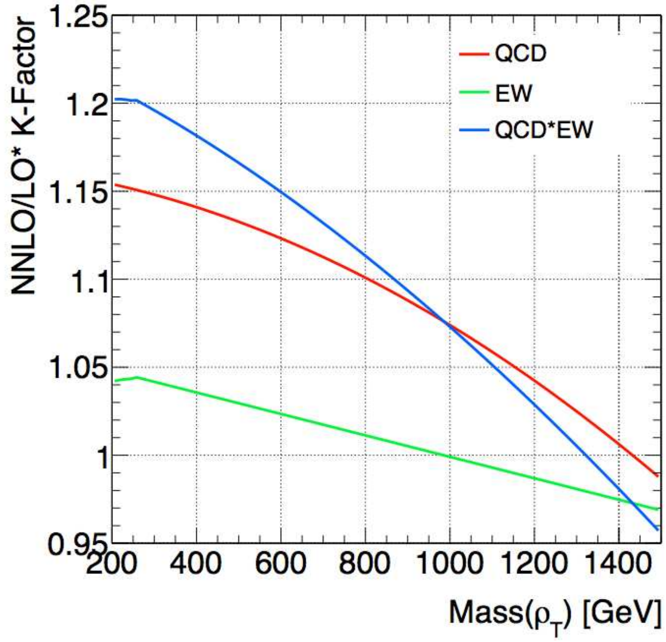

Figure 7·1: Cross section ratios for dilepton invariant mass giving the QCD, EW, and full QCD times EW k-factors. The background DY samples are corrected with the full QCD times EW blue correction, while the technicolor signal samples are corrected with QCD only (red), from Ref [4].

Backgrounds

The largest background is the Drell-Yan process, accounting for 90.7% of events in the search region above 130 GeV and 99.7% of total number of events above 70 GeV used in the analysis. The search for technihadrons is from 130 GeV – 2.5 TeV in dilepton invariant mass. In order to ensure good MC statistics over this whole range of dimuon invariant mass, the Drell-Yan MC samples were binned in dilepton invariant mass. Were the samples not binned the majority of MC statistics would be at the lower mass and the high interest search regions would be under-populated due to the steeply falling spectrum. The binned Drell-Yan samples cover 70 GeV – 3 TeV with eleven bins of varying width of dilepton mass.[2] The width of the samples was chosen such that the statistical uncertainty on the number of entries per 5 GeV in the upper edge of the bin would not be larger than 5%. Figure 7.2.2 shows the PYTHIA generator level dilepton mass for each of the eleven bins, that resulted from this analysis.

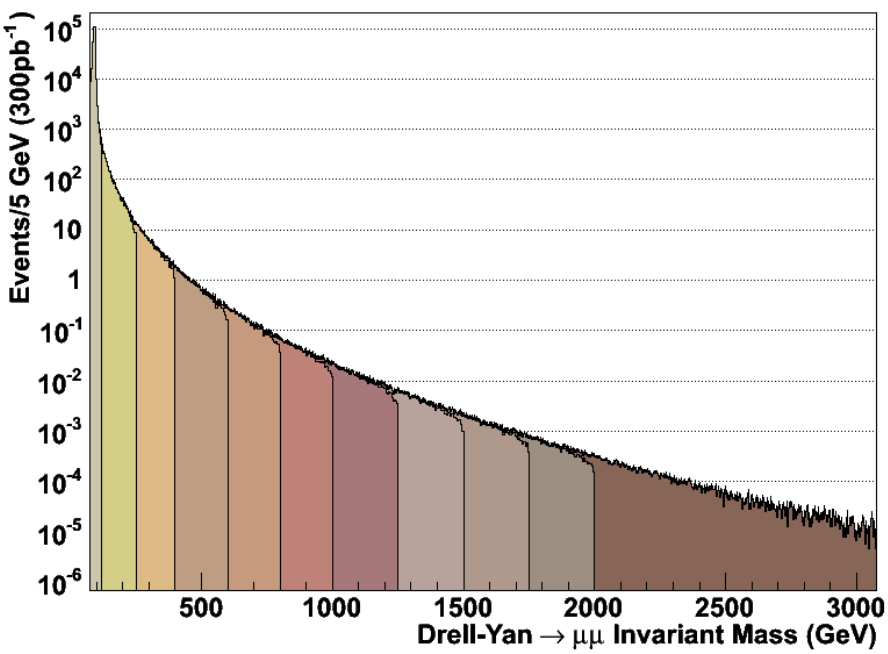

Figure 7·2: PYTHIA Drell-Yan to dimuon invariant mass spectrum, plotted as number of events per 5 GeV vs dimuon mass in GeV. This histogram has been scaled to the expected 2010 luminosity of 300 pb^{-1}. Here each different color is a different MC dataset, which when combined form a smoothly falling distribution.

[2]The highest mass bin has no upper bound, but high statistical coverage runs out at 3 TeV.

Additional Standard Model backgrounds considered were diboson WW, WZ, ZZ samples, W+jets, $t\bar{t}$ with top mass set to 172.5 GeV, and QCD samples with weights taken from data driven techniques. Table 7.1 gives the samples, generator, PDF, and relative contribution to the search region above 130 GeV. The $t\bar{t}$ samples are also binned in four regions of dilepton invariant mass to give a smooth distribution.

Technicolor Signal

The phenomenology of Low-scale technicolor has been implemented in PYTHIA [47], as a modification to the Drell-Yan propagator. This means that the ρ_T/ω_T are necessarily simulated with the Drell-Yan interference. The ρ_T/ω_T resonances are extremely narrow $\mathcal{O}(1\,\text{GeV})$, so the technicolor signal datasets are simulated in windows of $\pm$ 10 GeV around the resonance. The 20 GeV window minimizes the effect of the Drell-Yan "contamination" while taking into account the interference. Corresponding Drell-Yan samples are simulated in the same 20 GeV windows so that the Drell-Yan contribution to the cross section can be subtracted off and the ρ_T/ω_T only cross sections are used to normalize the signal MC. The window is shifted 0.5% due to the interference of the ρ_T and the ω_T. Table 7.2 shows the values for the 7 TeV center of mass energy samples LSTC and Drell-Yan with various k-factors applied. For this analysis the values of column K_{QCD} are used, as the EW k-factors may be model dependent.

There are many parameters in the LSTC theory that affect the cross section or branching fraction of the ρ_T/ω_T to dileptons. In this analysis we choose the PYTHIA defaults except for what is explicitly mentioned and all but the m(π_T) are taken to be unchanging. The non-m(π_T) parameters are as follows:

- The Q^2 scale where the PDFs are evaluated is set to be the dilepton invariant mass to be the same as the PYTHIA default for Drell-Yan.[3]

- The techniquarks charges are set such that $Q_U = (Q_D + 1) = 1$. Many technicolor production and decay rates are proportional to $(Q_U + Q_D)^2$, such as the $\rho_T/\omega_T \rightarrow l^+l^-$ process.

- The vector technimesons decay parameter M_V is set to be m(ρ_T). M_V affects the $\pi_T - G$ decay rates where G is a SM transverse gauge boson.

- The axial mass parameter is set to m(ρ_T). It affects the $\pi_T - G$ decay rates where G is a SM transverse gauge boson.

- The vector and axial mass parameters for the $a_T - G - \pi_T$ interaction are set to m(ρ_T).

- The vector and axial mass parameters for the $a_T - G - \rho_T$ interaction are set to be very large in this case 20×m(ρ_T).

Default Values

- The mixing angle between mass and π_T interaction eigenstates is set such that, $\sin(\chi) = 1/3$.

- The technipion decay constant discussed in Chapter 2, $F_T = 82$ GeV.

- The number of technicolors $N_{TC} = 4$.

- The coefficient of the π_T decay to charm and bottom, $C_c = C_b = 1$.

- The coefficient of the π_T decay to top, $C_t = 0.0182$

- The coefficient of the π_T decays to tau, $C_\tau = 1$.

[3] This is not the PYTHIA default for LSTC and must be set by hand, though it is the default for Drell-Yan. Meaning one must be changed in order for the cross section subtraction to make sense.

- The coefficient of the π_T to gluon-gluon decays, $C_\pi = 0$.
- The coefficient of the π_T' to gluon-gluon decays, $C_{\pi'} = 1.33333$.
- The mixing angle between the π_T' interaction and mass eigenstates, $\sin(\chi') = 0.33300$.
- The isospin violating ρ_T and ω_T mixing amplitude is set to be 0.05

The mass splitting between the π_T and the ρ_T/ω_T sets the available decays for the ρ_T and ω_T resonance, as discussed in Chapter 2. As m(π_T) controls only the branching fraction and does not affect the production or decay kinematics of the ρ_T/ω_T we assume that the acceptance and efficiency of the signal remains unchanged by the change in m(π_T), and only the weight of the events is affected due to the available decays.

Table 7.2: Low-scale technicolor cross sections for different masses and k-factors applied, from Ref [4].

m(ρ_T)	$\sigma \times B(ll)$ [fb]					
[GeV]	(LSTC+DY)	DY	LSTC LO*	K_{QCD}	K_{EW}	$K_{QCD \cdot EW}$
200	1050	868	184	212	192	221
250	483	378	104	120	109	125
300	257	196	63.2	72.6	65.8	75.6
350	149	110	39	44.6	40.5	46.4
400	91.9	66.9	25	28.5	25.9	29.5
500	59.5	42.8	16.7	19.0	17.2	19.6
600	39.9	28.4	11.4	12.9	11.7	13.3
800	19.4	13.7	5.68	6.38	5.81	6.53
1000	5.70	4.03	1.66	1.83	1.68	1.85
1500	2.02	1.42	0.603	0.648	0.602	0.647
2000	0.231	0.162	0.0693	0.0684	0.0671	0.0662

7.3 Event Selection

7.3.1 Muon Selection Criteria

The selection criteria used for reconstructed muons in the technicolor analysis were chosen to reduce the backgrounds and ensure the muon tracks are well measured. Events are required to have all the Inner Detector trackers and Muon Spectrometer detectors operating at high efficiency, as checked offline by Data Quality experts. Events analyzed have either a 22 GeV p_T threshold muon trigger, or a 40 GeV p_T threshold trigger if geometrically in the barrel portion of the Muon Spectrometer.

To remove non-prompt and other muon backgrounds such as cosmic muons, beam halo, and muons from decays in flight, we require all events have a primary vertex with at least three tracks within 200 mm of the interaction point in z. In addition each muon track is required to be within 0.2 mm perpendicular to the interaction point, and 1 mm along the z-axis or beam line. A further reduction in non-prompt backgrounds comes from requiring the reconstructed muon have tracks in both the Inner Detector and Muon Spectrometer, and form a combined muon track. The p_T spectrum of non-isolated and non-prompt muons is steeply falling, and a requirement that the p_T be over 25 GeV removes the majority of this contribution. These muons are produced in association with hadronic activity and have a higher multiplicity of particles than muons from the signal process. A requirement that the amount of p_T of tracks in the Inner Detector within a geometric cone around the muon track, called isolation, be low can reduce these backgrounds further. Finally, the muons are required to have opposite charge, as muons produced from QCD are not correlated with each other and should have an equal number of like and opposite charged pairs.

The reconstructed muon tracks have detector specific hit requirements to ensure the muons are well measured. In the Inner Detector the track must have hits in detectors it passed through, and there is a limit to the number of holes on the track or outlier hits not associated with the track. In addition the matched Muon Spectrometer track must have precision hits in all three measurement stations, as well as at least one ϕ measurement from the fast response technologies. Finally, there is a veto on tracks which pass through the complex magnetic field region in the transition from barrel to end-cap, by vetoing tracks with hits in both the barrel and end-cap or any of the transition chambers.[4] All of these hit requirements are summarized in Table 7.3.

Table 7.3: Detailed hit requirement for each reconstructed muon track. The TRT outlier fraction veto when $|\eta| >= 1.9$ is only applied if the number of hits plus outliers is greater than five. If it is not then no requirement or veto is applied.

Detector Technology	**Hit Requirement**	**Veto**
	Inner Detector	
B-Layer	If expected >1	
Pixel	Hits + Dead Sensors >= 2	Pixel Holes + SCT Holes <= 2
SCT	Hits + Dead Sensors >= 6	Pixel Holes + SCT Holes <= 2
TRT $\|\eta\| < 1.9$	Hits + Outliers > 5	Outlier Fraction < 0.9
TRT $\|\eta\| >= 1.9$	If (Hits + Outliers > 5)	Then (Outlier Fraction < 0.9)
	Muon Spectrometer Barrel	
MDT Barrel	Hits > 3 & Layers == 3	BIS78 Hits or MDT End-cap hits
RPC	Hits > 1 & Layers >= 1	
	Muon Spectrometer End-cap	
MDT End-cap	Hits > 3 & Layers >= 2	BEE or EEL Hits or CSC Precision Hits or MDT Barrel Hits
CSC Precision	Hits > 3	MDT Small Wheel Hits
TGC	Hits > 1 & Layers >= 1	
CSC	Hits > 1 & Layers >= 1	

The muons passing all previous selections are required to be isolated from other tracks in the events. Inner Detector tracks of 1 GeV p_T within a cone of radius 0.3 as the quadrature sum in are summed together, and divided by the muon p_T. This scaled track-based isolation must be less than 5%. This helps to reduce the contributions of muons from QCD backgrounds to the dataset, particularly those from heavy flavor jets, and non-prompt pion and kaon decays.

Applying quality criteria results in a 49.5% efficiency for events that passed the

[4] These chambers are the MDT BEE, EE, and BIS78's, which were either not installed, not well aligned, or in regions where the magnetic field was not well understood.

trigger and have two combined 25 GeV p_T muons. This corresponds to a 70.4% selection efficiency for a combined muon with at least 25 GeV p_T. The Inner Detector hit and primary vertex requirements are both over 98% efficiency compared to the previous selection, and the isolation requirement is 95% efficient. The main drop in efficiency comes from the Muon Spectrometer hit requirement which is 76.3% efficient compared to the number of muon tracks passing the Inner Detector requirement.

Due to the geometry of the ATLAS Muon Spectrometer, the three station hit requirement acts as an implicit selection on η. The effect can be seen in looking at the muon eta distribution shown in Figure 7·3. The drop in efficiency at $|\eta| = 1.2$, corresponding to the transition region between the barrel and end-cap. The lower efficiency in this transition region is because the full compliment of chambers have not yet been installed. There is also a veto on tracks with hits in both the barrel and end-cap chambers that effects tracks in this region. In addition there are regions where infinite momentum straight tracks would only pass through two stations or one of those stations would be in the barrel(end-cap) with the other two being in the end-cap(barrel). Furthermore at $\eta \simeq 0$ there is a non-instrumented region in the large sectors for services to pass through the spectrometer.

Table 7.4: Cut flow for signal MC, with absolute efficiency and relative to the previous selection.

Cut Description	Absolute Efficiency (%)	Relative Efficiency (%)
Trigger	94.3	94.3
Primary Vertex	93.9	99.5
2 Combined Muons	77.7	82.7
p_T	76.7	98.7
ID Hits	74.2	96.7
MS Hits	43.0	57.9
d_0	43.0	99.9
z_0	42.9	99.9
Isolation	41.8	97.5
Opposite Sign	41.8	99.9

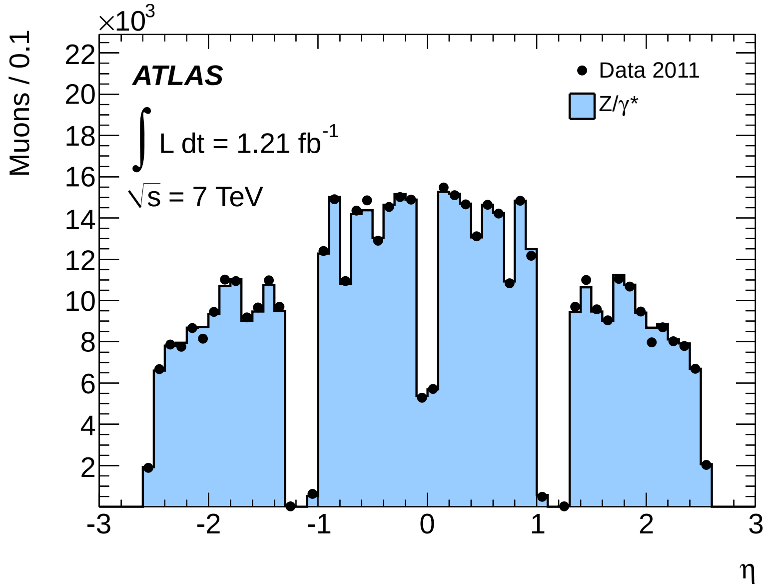

Figure 7·3: Muon pseudo-rapidity after event selection. The points represent ATLAS data and the filled histogram shows the Monte Carlo background, from Ref [5].

The relative and absolute efficiency of each selection is shown in Table 7.4, as determined from a m(ρ_T/ω_T) = 1000 GeV MC sample. While Figure 7·8 the signal efficiency as a function of dimuon invariant mass and is discussed further.

7.3.2 Event Selection

The lowest p_T unprescaled single muon trigger, is used for this analysis to keep efficiency as high as possible. For this data period the trigger required a 22 GeV p_T threshold in the event filter stage, from a combined muon or a "tagged" muon meaning an Inner Detector track matching a calorimeter deposit and a segment in the inner layer of the Muon Spectrometer, or a 40 GeV p_T muon measured in the Muon Spectrometer if in the barrel. This combination of triggers is 94.3% efficient for a 1.5 TeV signal sample. If the analysis were to use a dimuon trigger the efficiency would be the square of the single muon efficiency or 89% this 5% drop in efficiency at the trigger level, can never be recovered in reconstruction as the events are lost. In addition to the trigger requirement there is an explicit requirement that the Inner Detector and Muon Spectrometer be taking high quality data as determined by both online and offline Data Quality experts.

An additional background for dimuon searches are cosmic ray muons. Passing through the detector they reconstruct as two oppositely charged back-to-back tracks. Cosmic muons have no preference to pass through the IP, and geometric selections on d_0 and z_0 remove a large fraction of even the high-$\mathrm{p_T}$ the cosmic events. Finally, true collisions involving protons produce additional tracks from the spectator quarks and not just the interacting partons. In the end muons from cosmics contribute very little to the analysis. The contamination due to cosmics in the final sample was estimated by inverting the selection on the orthogonal variables z_0 and d_0 and extrapolating each into the selection region. This is taken as an upper bound and the number of cosmics passing the final selection is then less than:

$$N_{cosmics} = (1.88 \pm 1.33) \cdot 10^{-2}. \tag{7.1}$$

After the muon object selections are applied, events are split by invariant mass between 70 GeV $< m_{\mu\mu} <$ 110 GeV and $m_{\mu\mu} \geq$ 130 GeV. In Table 7.5 are the expected yields by MC sample and the observed numbers from data. The first mass bin is used to normalize the sum of the MC backgrounds to the observed number of data events. This scaling is then used across all bins, where there is good agreement shown. The uncertainty given for the MC total is the statistical uncertainty on the number of observed data events.

Table 7.5: Expected and observed number of events in the dimuon channel for 1.21 fb^{-1}. The first bin is used to normalize the sum of backgrounds to the data. The uncertainties include both statistical and systematic except on the total background which is given by the square root of the number of observed events, from Ref [5].

$m_{\mu\mu}$[GeV]	70-110	110-130	130-150	150-170	170-200
DY	236318.6 ± 319.7	3132.1 ± 87.5	1073.4 ± 35.9	548.7 ± 21.8	416.3 ± 18.3
$t\bar{t}$	193.1 ± 21.0	70.0 ± 9.1	50.7 ± 7.0	34.2 ± 3.6	37.7 ± 3.9
Diboson	306.7 ± 15.9	24.9 ± 2.2	19.4 ± 2.0	13.3 ± 1.6	11.7 ±1.5
W+jets	1.3 ± 0.7	0.4 ± 0.4	< 0.05	0.2 ± 0.2	< 0.05
QCD	1.3 ± 1.2	0.3 ± 0.2	0.1 ± 0.1	0.1 ± 0.1	< 0.05
Total	236821.0 ± 320.8	3227.8 ± 88.0	1143.7 ± 36.6	596.5 ± 22.2	465.8 ± 18.7
Data	236821	3210	1132	621	443
$m_{\mu\mu}$[GeV]	200-240	240-300	300-400	400-800	800-3000
DY	249.4 ± 13.0	152.9 ± 7.1	80.8 ± 3.9	40.3 ± 2.5	2.0 ± 0.3
$t\bar{t}$	30.5 ± 3.2	20.6 ± 2.2	11.7 ± 1.2	4.2 ± 0.4	0.1 ± 0.0
Diboson	10.1 ± 1.4	8.0 ± 1.1	6.7 ± 1.1	1.7 ± 0.5	< 0.05
W+jets	< 0.05	< 0.05	< 0.5	< 0.05	< 0.05
QCD	< 0.05	< 0.5	< 0.5	< 0.05	< 0.05
Total	290.0 ± 13.5	181.5 ± 7.6	99.3 ± 4.2	46.1 ± 2.6	2.1 ± 0.3
Data	279	195	83	51	5

7.4 Performance

The event and object selection remove as much of reducible backgrounds as possible. Here in Figure 7·4 is a plot of the isolation variable used in the search for high mass dilepton resonances [5]. Summing the p_T of tracks within a δR of 0.3 of the muon track direction, scaled by the p_T of the muon.[5] The signal-like muons from the Drell-Yan process are highly peaked near 0, while the non-isolated muons from QCD are spread evenly. The selection used in this analysis was $\Sigma {p_T}^{trk}/{p_T}^{\mu} \leq 0.5$ and can be seen from Table 7.4 to be 97.5% efficient for a technicolor signal sample.

Figure 7·5 shows the p_T spectrum for muons passing the full high mass dilepton selection. The dimuon invariant mass for events passing all selections is shown in Figure 7·6. The MC samples in this histogram have been scaled so that the sum

[5]Defined as $\delta R = \sqrt{\delta\eta^2 + \delta\phi^2}$

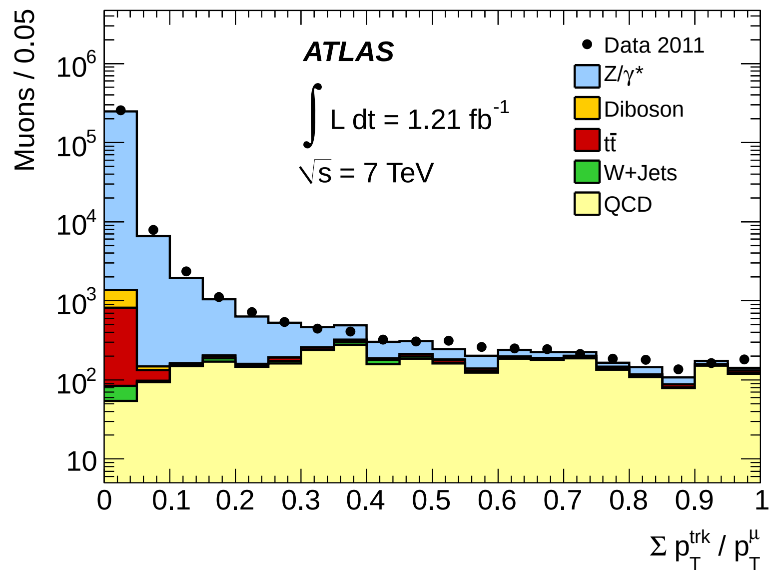

Figure 7·4: Muon isolation variable, sum of p_T of tracks within an angular cone of 0.3, scaled by the muon's p_T. The selection made for this analysis is that this variable be less than 0.5, from Ref. [5].

of the MC backgrounds have the same number of events under the Z peak between 70 GeV – 110 GeV. In addition this distribution has three potential signals included as open histograms.

7.5 Acceptance Studies

The dimuon resolution shown in Figure 6·6 shows that the intrinsic width of a SSM Z' is below the detector resolution which dominates the observation of a resonance. Therefore the narrow spin-1 ρ_T/ω_T should be consistent with the signal templates for the SSM Z'. Signal samples of 100k events were generated using PYTHIA and the kinematic distributions are shown in Figure 7·7. It can be seen from these distributions that in the kinematic regions where the analysis is concerned with there is very good agreement between the SSM Z' and ρ_T/ω_T signal MC. A fit is performed to the fully simulated ρ_T/ω_T samples of varying mass, using the SSM Z'

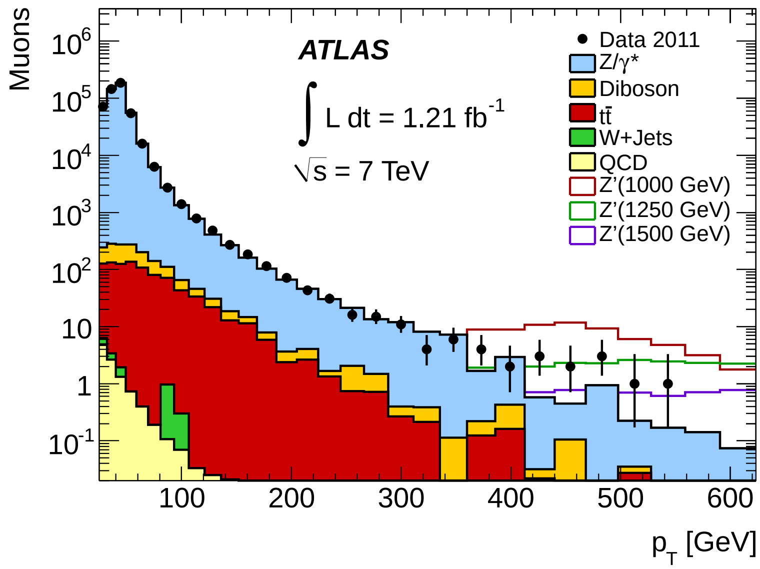

Figure 7·5: Muon p_T distribution for the high mass resonances search [5]. Shown in black are reconstructed muons passing all selections in data, and the filled histograms correspond to the different background processes.

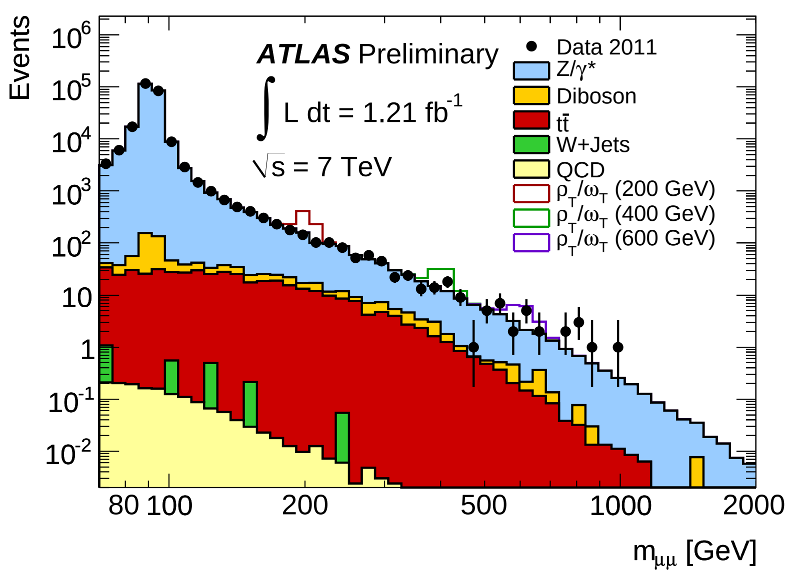

Figure 7·6: Dimuon invariant mass of events passing all selections [6].

fit plus a constant. The result shown in Figure 7·8 shows very good agreement. The fitted value for the efficiency offset is - 0.3% with a fit χ^2/N_{dof} of 0.83. The analysis framework developed for the SSM Z' search [5] is therefore usable for the search for technihadrons.

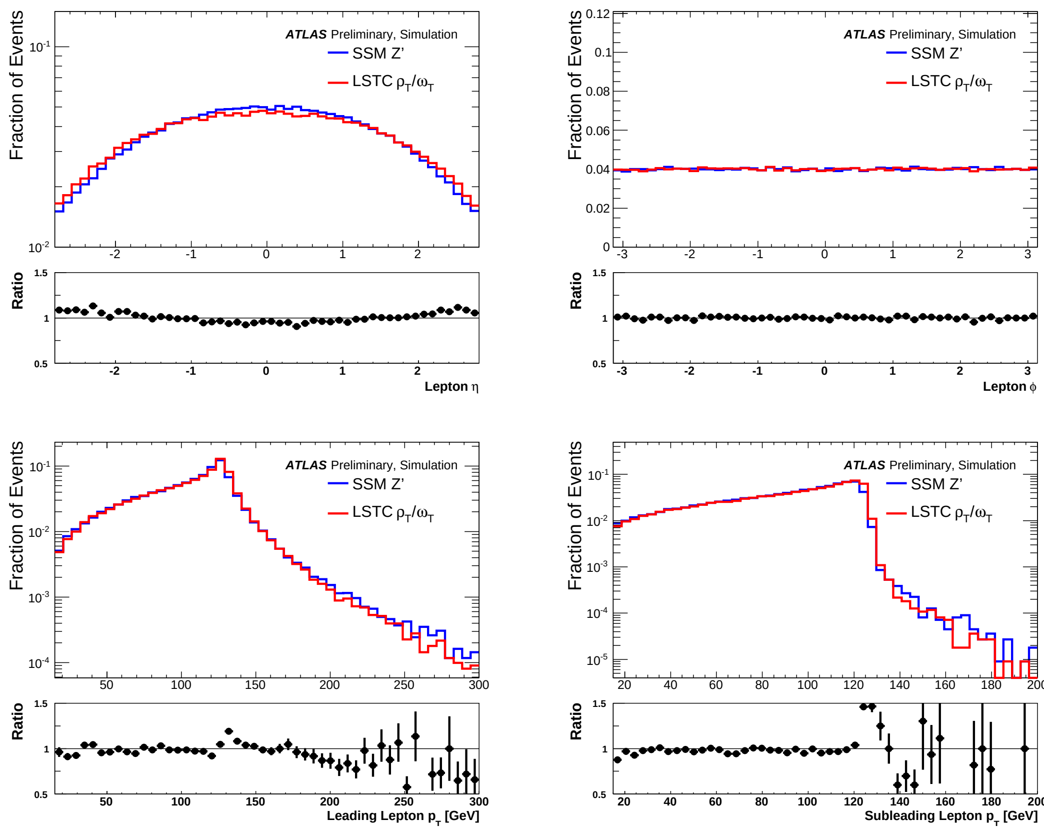

Figure 7·7: Generator distributions of leptons coming from ρ_T/ω_T in red and SSM Z' in blue. The ratios are ρ_T/ω_T to SSM Z', from Ref [6].

7.6 Systematic Uncertainties

By normalizing the sum of the MC datasets to the number of data events observed at the Z peak between 70 - 110 GeV, this analysis is insensitive to the uncertainty on the luminosity and any other mass-independent uncertainties. However, this method

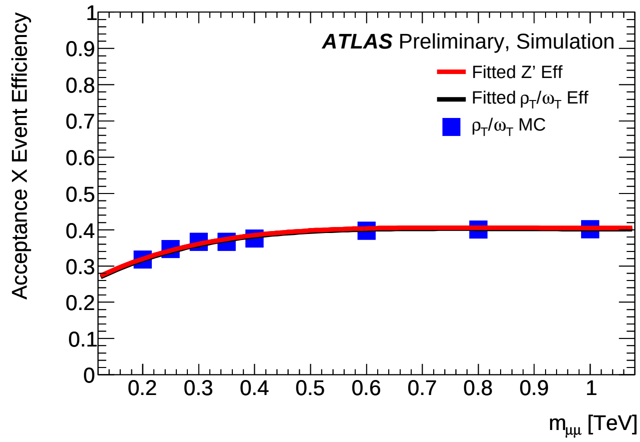

Figure 7·8: Fit of ρ_T/ω_T signal MC acceptance times efficiency using the SSM Z' fitted efficiency function(red) plus a constant(black), from Ref [6].

does introduce a systematic uncertainty of 5% due to the theoretical uncertainty on the Standard Model prediction of the Z cross section σ_Z.

The experimental systematic uncertainties considered for this analysis are data to MC normalization mentioned above, the reconstruction efficiency and resolution. The theoretical uncertainties for this analysis are the PDFs and Electroweak and QCD k-factors. Table 7.6 summarizes the relative contribution of these sources of systematic uncertainty. It is assumed that these uncertainties are correlated between signal and background MC samples with the exception of the Electroweak k-factor that is only applied to the Drell-Yan sample. It is also assumed that these uncertainties are correlated across all bins in the search region. In general due to the normalization to the Z peak the systematics are small at dilepton masses near the Z peak and grow larger at high invariant mass.

Table 7.6: Summary of systematic uncertainties on the expected numbers of events, from Ref [5].

Source	Signal Samples	Background Samples
Normalization	5%	5%
PDFs	10%	10%
QCD K-factor	3%	3%
Weak K-factor	NA	4.5%
Efficiency	4.5%	4.5%
Resolution	1.5%	NA
Total	13%	14%

7.6.1 Theoretical Systematic Uncertainties

The largest systematic uncertainty is that associated with the PDFs central value based on measurements used to evaluate the uncertainty. Each PDF uses a unique parameterization of a complete set of orthogonal eigenvectors. Each eigenvector has an uncertainty associated with it. To determine the systematic associated with the PDF each eigenvector is varied within its uncertainty while the other eigenvectors are held at their central value. For each variation on the eigenvectors the signal cross section is calculated [77]. The asymmetric uncertainty as a function of mass is:

$$\begin{aligned} \Delta\sigma^{+} &= \sqrt{\sum_{i=1}^{n}(max(\sigma_i^{+} - \sigma_0, \sigma_i^{-} - \sigma_0, 0))^2} \\ \Delta\sigma^{-} &= \sqrt{\sum_{i=1}^{n}(max(\sigma_0 - \sigma_i^{+}, \sigma_0 - \sigma_i^{-}, 0))^2} \end{aligned} \tag{7.2}$$

In this equation the σ_i^+/σ_i^-'s correspond to the cross section as calculated when the ith PDF eigenvector is varied up or down, relative to the nominal value σ_0. The largest difference is taken and summed in quadrature with the results of the same procedure for the other eigenvectors. For the Drell-Yan and signal MC, as shown in Table 7.1, the PDF used was a LOmod PDF [72] using both Leading Order and

Next to Leading Order information. This is done to improve on performance of either pure LO or NLO PDFs with LO generators. However, the uncertainty on the MRST07LO* PDF at high mass represents the largest uncertainty on the measurement. This search remains statistics limited, and increasing luminosity would improve the result faster than decreasing the systematic uncertainties.

In correcting our LO MC for higher order affects, there is an implicit assumption that only the weight of cross section changes and not the kinematics or event properties. For example if the cross section increases the η distribution remains constant. The Drell-Yan cross section has been calculated at NNLO with various PDF sets using the program PHOZR [78]. The NNLO cross sections are calculated in bins of dilepton invariant mass. These cross sections have been used to correct the PYTHIA and MRSTLO* LO cross sections. The values of these corrections can be seen in Figure 7.2.2. The uncertainty on this k-factor correction comes from studies of the Drell-Yan cross section and spectrum [79]. For the QCD k-factor the uncertainty is calculated by comparing the cross sections measured of like order PDFs by fluctuating the PDF sets up by 25% between m_{ll} 10-400 GeV. The result has a modest dependence on m_{ll} which was estimated to be 3%.

In addition to the QCD k-factor discussed above the EW k-factor also shown in Figure 7.2.2 has been taken into account using the NNLO event generator HORACE [80]. This correction takes into account the initial and final state radiation of a photon, or Z, EW loops, and the photon contribution to the proton structure, but not radiation of a W or Z boson. The uncertainty of 4.5% on the Drell-Yan cross section is estimated from the running of the fine structure constant, and corrections $\mathcal{O}(\alpha\alpha_s)$, which are neglected. In the end this correction is only applied to the Drell-Yan background sample, and this uncertainty is only on the number of expected Drell-Yan events.

7.6.2 Systematic Uncertainties on Muons

There are two systematic uncertainties associated specifically with the muon channel of the analysis and not the dielectron. These are uncertainties on the number of events that will be observed and the invariant mass resolution. The uncertainty associated with the acceptance and efficiency affects both signal and background yields. While the systematic associated with the resolution just broadens the shape of the observed signal template and has limited impact on sensitivity. The p_T scale was calibrated, by fitting the Z peak in data, to better than 0.1% and is neglected. The remaining systematics associated with the resolution parameters are determined by shifting the smearing parameters within the constraints from the alignment studies discussed in Chapter 6. This is determined to have a 1.5% impact on a 1.5 TeV SSM Z' signal. As the analysis is searching for a peak above a smoothly falling background, it is insensitive to any resolution systematic on the backgrounds, and only a dilution of the signal will affect the final result. Therefore the systematic associated with the resolution is applied only to the signal MC.

The muon trigger and reconstruction efficiencies were determined using a "tag-and-probe" method on $Z \rightarrow \mu\mu$ events. Events are selected with one "tag" muon passing all selection criteria, and an isolated Inner Detector track from the same vertex. Then requiring the invariant mass of the combination of the tag and probe to be within 20 GeV of the Z peak. Furthermore there is a requirement that the tracks be back-to-back by selecting $|\Delta\phi(tag - probe)|$ be greater than 2.0. This method is most accurate for muons with p_T below 100 GeV. For the trigger efficiency, the uncertainty was determined by varying the matching criteria between a reconstructed track and trigger object.

For the reconstruction systematic uncertainty the p_T threshold of the tag muon was varied, as well as the invariant mass window around the Z peak, and the

$|\Delta\phi(tag - probe)|$ requirement. The systematics associated with the variation of these selections were shown to be uncorrelated, and the total systematic calculated by summing over the contributions in quadrature. The end result of the "tag-and-probe" analysis is shown in Table 7.7 and the systematic associated with the trigger reconstruction efficiency extrapolated to 1.5 TeV, is 4.5%.

Table 7.7: Average reconstruction efficiency for muons with p_T above 25 GeV, as determined using the "tag-and-probe" method on data and MC, from Ref [5].

	Tag-and-Probe results
Average Efficiency (data)	$73.553 \pm 0.134^{+0.019}_{-0.105}$ %
Average Efficiency (MC)	74.90 ± 0.10 %

7.7 Statistical Methods

7.7.1 Discovery Statistics

To test the consistency of a background only hypothesis with the observed data a p-value is used. Defined as the probability of observing an outcome at least as signal-like as the one observed in the data assuming the background only hypothesis correctly models the the data. The convention for 3σ observation and 5σ discovery correspond to p-values of 1.35x10^{-3} and 2.87x10^{-7} respectively. These values correspond to the one sided integral of a Gaussian distribution from 3σ and 5σ to $-\infty$ normalized to the integral of the full range $-\infty$ to ∞.

As the mass and cross section of the potential signal is not known as scan of mass verses cross section is performed. The results are ranked based on their log-likelihood-ratio [81]:

$$LLR = -2\ln\frac{L(S+B)}{L(B)} \tag{7.3}$$

where the likelihood function, $L()$ determines the likelihood of the background only and signal plus background hypotheses. This log-likelihood-ratio is based on a template shape fitting technique, that is the product of the single bin Poisson likelihoods. The template shape fitting technique finds the most likely signal as determined by the data. The most probable signal is then used to calculate the p-value to test how discrepant the signal is with the observed data. For the dimuon channel the most likely signal gives a p-value of 24% with the observed data. In the dielectron channel the p-value is 54%. There is no significant excess and 95% confidence level limits are set.

7.7.2 Limit Setting

Given the absence of signal an upper limit on the cross section times branching ratio is determined at the 95% confidence level using a Bayesian approach [82]. The invariant mass distribution is compared to SSM Z' signal and SM only background templates over the search region from 130 GeV up to 2500 GeV. As in the discovery statistics a likelihood function is defined as the product of the Poisson probabilities over all mass bins in the search region. In each bin the Poisson probability is evaluated for the observed number of data events given the prediction from MC. A uniform prior is used for each template mass, as there is no motivation to favor one mass over another.

Using the acceptances of the signal sample and Z sample the limit on the number of events is converted to a limit on the ratio of cross sections between the Z' signal template, and the observed Z cross section. Producing a mass dependent cross section which has been ruled out at the 95% confidence level. Systematic uncertainties are included as mass dependent nuisance parameters in the likelihood function that are integrated over in the calculation of the likelihood function. The systematic uncertainty nuisance parameters can be correlated across bins and samples.

To determine the expected limit, pseudo-experiments are used. The number of observed data events are selected from the Standard Model background only MC at random. These samples are then treated the same as the data samples, and a limit is produced. The limits from 10,000 pseudo-experiments produces a distribution of limit cross section, versus signal mass, the central value is taken as the expected limit, and the one and two sigma bands from the Gaussian width. These one and two sigma bands do not include the theoretical uncertainty.

As the predicted resonances decay to both electrons and muons the two orthogonal decay channels provide a mostly independent measurement of the limit. To calculate a combined limit the likelihood functions for each channel are multiplied together bin by bin, and then treated the same way. There are some systematic uncertainties that are correlated with both samples, such as the systematic uncertainty due to PDF.

7.8 Low-Scale Technicolor Limits

Given the absence of a technicolor signal, limits are set on the m(ρ_T/ω_T) in the context of Low-scale technicolor discussed in Chapter 2. The upper limit on the number of signal events is a limit on the cross section as a function of m(ρ_T/ω_T) above the Standard Model background prediction. This limit is set on a LSTC model with the parameter choice that m(π_T) = m(ρ_T/ω_T) -100 GeV. This limit is also then interpreted as a contour on m(ρ_T/ω_T) vs m(π_T) vs σ_T. The choice of one standard set of parameters allows this measurement to be compared to previous measurements and particle searches.

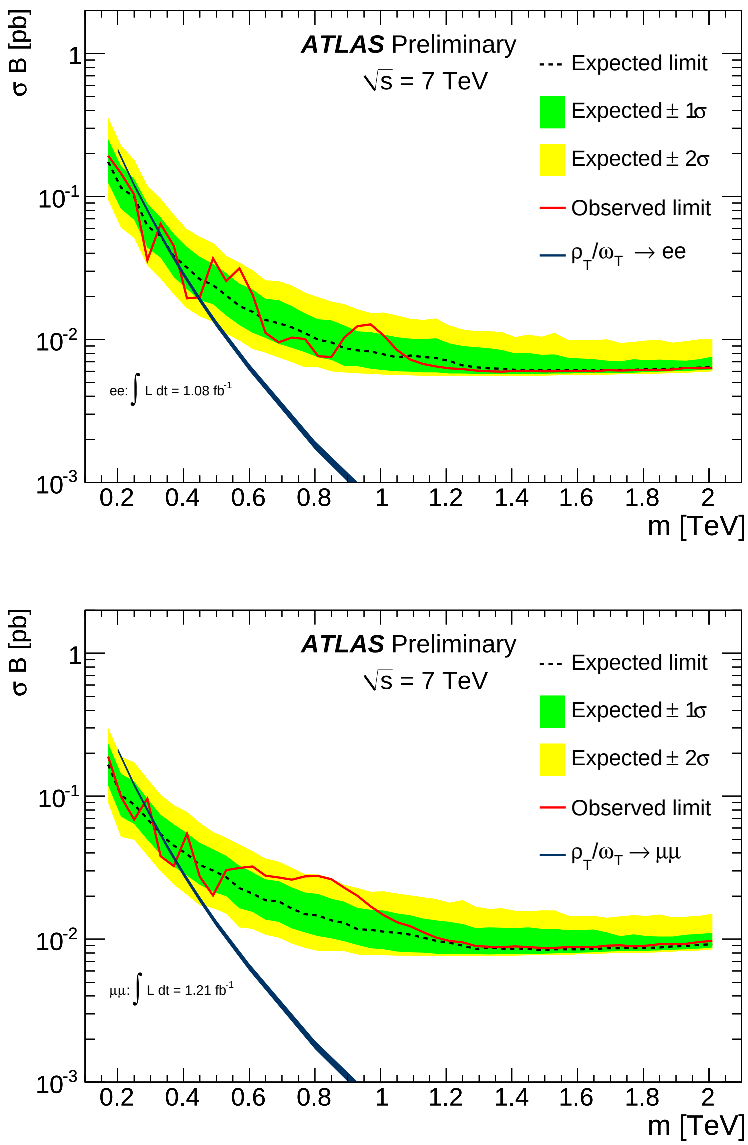

Figure 7·9: Dielectron and dimuon 95% Bayesian upper limit the intersection of the red and dark blue lines give the mass limits, from Ref [6].

7.8.1 Benchmark Parameter Limits

In the dimuon channel, shown in Figure 7·9, there is a gap in the coverage and masses below 376 GeV are excluded with the exception of masses between 280 - 304 GeV. In the dielectron channel, shown in Figure 7·9, there is a gap in the coverage and masses of ρ_T/ω_T are excluded below 445 GeV with the exception of masses between 322 - 386 GeV. When combined the electron and muon channel exclusion region is all masses of ρ_T/ω_T below 470 GeV. The expected exclusion region was m(ρ_T/ω_T) $\leq$ 442 GeV, the measurement is said to be "lucky" as a larger than expected region was excluded. To obtain the strictest limit and have a continuous exclusion curve it is necessary to combine the channels, Shown in Figure 7·10 is the combined 95% confidence level limit derived from the combination of the dielectron and dimuon channels.

Table 7.8: Excluded ranges of ρ_T/ω_T mass at 95% C.L. from the dielectron, dimuon and dilepton channels, assuming $m(\pi_T) = m(\rho_T/\omega_T) - 100\,\text{GeV}$, from Ref [6].

Channel	Observed mass exclusion [GeV]	Expected mass exclusion [GeV]
$\rho_T/\omega_T \to e^+e^-$	$m < 323$ and $386 < m < 445$	$m < 345$
$\rho_T/\omega_T \to \mu^+\mu^-$	$m < 280$ and $304 < m < 376$	$m < 330$
$\rho_T/\omega_T \to \ell^+\ell^-$	$m < 470$	$m < 442$

7.8.2 Limits on m(ρ_T/ω_T) vs m(π_T)

At each value of m(ρ_T/ω_T) we find the intersection of the 95 % confidence level cross section measurement with the theoretically predicted σ_T. This intersection along with the constraint that m(ρ_T/ω_T) $\geq$ m(π_T) defines an excluded region in the parameters space m(ρ_T/ω_T) vs m(π_T). Limits are quoted as an exclusion range for m(ρ_T/ω_T) given a range of m(π_T). To perform the search as a function of m(π_T) vs

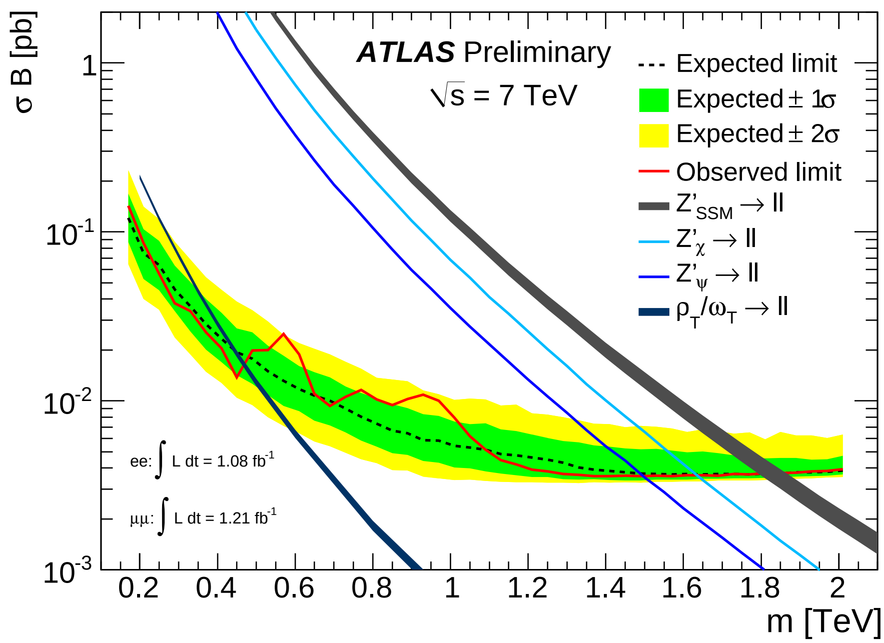

Figure 7·10: The combined 95% C.L. with the, LSTC theory curve shown in dark blue. Also included are three Sequential Standard Model Z' models. The dashed line corresponds to the expected exclusion curve, with the green and yellow bands the $\pm$ $1\sigma/2\sigma$ regions respectively, from Ref [6].

m(ρ_T/ω_T) 833 cross sections were simulated with at most 25 GeV spacing to provide good coverage of the phase-space. Figure 2·5 shows the ρ_T/ω_T cross section as a function of m(π_T) for three values of m(ρ_T/ω_T).

The combined limit uses the 1.21 fb^{-1} in the dimuon channel combined with the 1.08 fb^{-1} in the dielectron channel. Using the procedure described above the measured exclusion cross section of Figure 7·10 are interpreted as an exclusion on the m(ρ_T/ω_T) vs m(π_T) vs σ_T surface. Masses of ρ_T/ω_T are excluded below 130 - 480 GeV for m(π_T) between 50 - 480 GeV. Figure 7·11 shows the exclusion region in red. Over the majority of the phase space the limit parallels the $\rho_T/\omega_T \rightarrow \pi_T, W^{\pm}/Z$ threshold, where the LSTC cross section times branching ratio to dileptons is falling steeply.

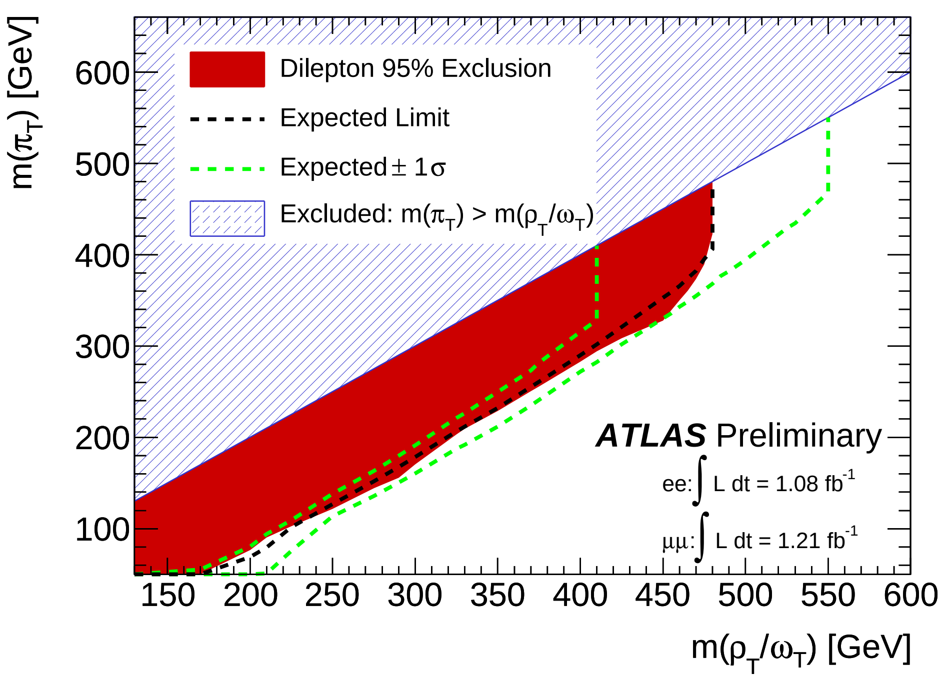

Figure 7·11: The 95% C.L. excluded region as a function of the assumed $\pi_T$and ρ_T/ω_T masses is shown in red. The dashed line shows the expected limit with the green dashed lines showing the $\pm 1\sigma$ bands, from Ref [6].

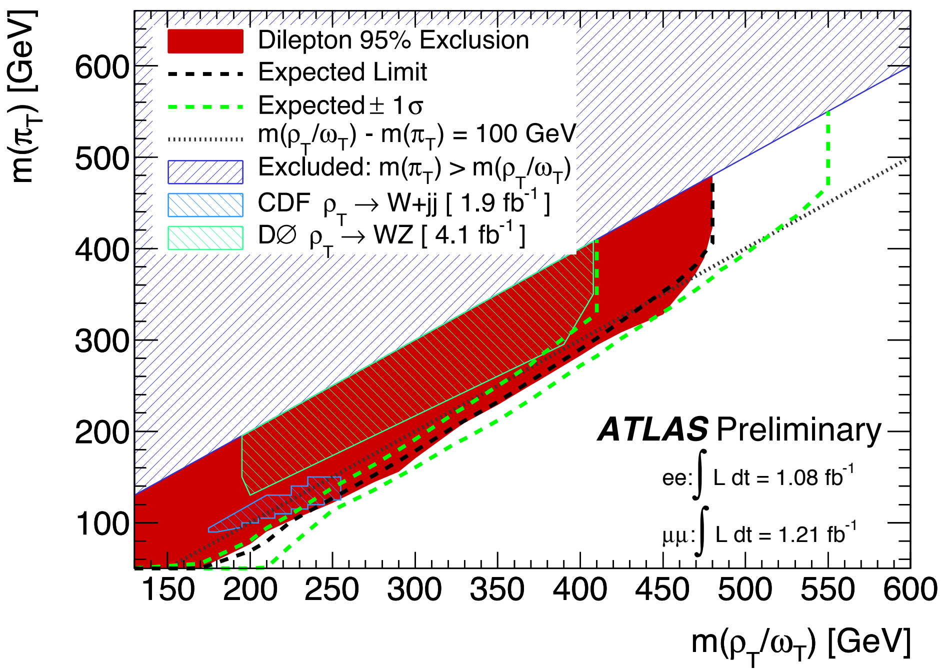

Figure 7·12: The 95% C.L. excluded region as a function of the assumed $\pi_T$and ρ_T/ω_T masses is shown in red. The dashed line shows the expected limit with the green dashed lines showing the $\pm 1\sigma$ bands, from Ref [6].

This analysis is the first to set limits on m(ρ_T/ω_T) vs m(π_T) in the dilepton channel. The previous experimental limits on the m(ρ_T/ω_T) vs m(π_T) come for charged $\rho_T^{\pm}$ decaying to a W and two jets [11], and the $\rho_T^{\pm}$ decaying to a W and a Z in the three lepton final state [10]. The limits from the CDF and D0 searches can be seen overlayed on the two dimensional exclusion plot, Figure 7·12 [6]. The exclusion curve from this analysis contains the excluded region of the previous limits, making this limit the current world's best limit on the Low-scale technicolor theory.

Chapter 8

Summary and Conclusions

8.1 Summary

This thesis presented a search for spin-1 technihadrons in the dimuon final state using 1.21 fb^{-1} of proton-proton collisions at $\sqrt{s} = 7$ TeV collected with the ATLAS detector. This search is an extension of the ATLAS Search for High Mass Dilepton Resonances [5], and uses the same event selection and statistical search strategy. As the data collected was inconsistent with a new narrow resonance the measurement is interpreted as a 95% confidence level limit on the mass of ρ_T/ω_T. Combining the dimuon channel with the result from the dielectron channel, gives the best limit. For the dilepton combined limit in the Low-scale technicolor model, masses of ρ_T/ω_T below 480 GeV are excluded for m(π_T) between 50 - 480 GeV. This measurement is the current world's best limit on the Low-scale technicolor model.

8.2 Outlook

Work is already on going by the ATLAS collaboration to improve on this measurement. Large gains in sensitivity are possible by using dedicated technicolor signal templates, increasing the muon efficiency by including additional chambers and relaxing the quality requirements. Furthermore the ATLAS detector has recorded over 5.2 fb^{-1} of luminosity during the 2011 physics run. The full 2011 dataset not only represents an increase on the analyzed dataset by a factor of 5, but also a great improvement on the understanding of the detector. These advances should improve the resolution, and efficiency of the analysis. Further improvements on this analysis will also allow the axial vector a_T to be included in the analysis increasing the sensitivity. The a_T is a second narrow resonance that would increase the sensitivity of a dedicated search.

Work is on going for searches in other channels besides dileptons and for different theoretical technicolor models. But if technicolor is the correct mechanism of Electroweak symmetry breaking the experiments at the LHC will find it, as technicolor theories predict the scale of technicolor Λ_T to be $\mathcal{O}(1\,\text{TeV})$. With an expectation of hundreds of fb^{-1} of luminosity over the lifetime of the experiment, and with an increase to $\sqrt{s} = 14$ TeV eventually coming, the limits set will leave very little parameter space for technicolor signals to hide from experimentalists. But hopefully a discovery is around the corner.

List of Journal Abbreviations

ADNDT	....	Atomic Data and Nuclear Data Tables
Ann. der Phys.	....	Annalen der Physik
Cmput. Phys. Commun.	....	Computer Physics Communications
Euro. Phys. J.	....	European Physics Journal
Il Nuo. Cim.	....	Il Nuovo Cimento
J. of Phys.	....	Journal of Physics
J. Phys. G.	....	Journal of Physics G
JHEP	....	Journal of High Energy Physics
JINST	....	Journal of Instrumentation
Nucl. Ins. Meth.	....	Nuclear Instruments and Methods
Nucl. Phys.	....	Nuclear Physics
Phys. Lett.	....	Physical Letters
Phys. Lett. B	....	Physics Letters B
Phys. Rev.	....	Physical Review
Phys. Rev. D	....	Physical Review D
Phys. Rev. Lett.	....	Physical Review Letters
PRSL	....	Proceedings of the Royal Society of London
Rep. Pro. Phys.	....	Reports on Progress in Physics
Rev. Mod. Phys.	....	Review of Modern Physics
RPP	....	Reports on Progress in Physics
RSL	....	Royal Society London
Z. Physik	....	Zeitschrift für Physik

Bibliography

[1] Nakamura,K. *et al.* (Particle Data Group), J. Phys. G. **37** (2011) 075021.

[2] Evans L. *et al.*, JINST **3** (2008) S08001.

[3] The ATLAS Collaboration, JINST **3** (2008) S08003.

[4] Sekhon, K. and Love, J. and Long, A. and Butler, J., ATL-COM-PHYS-2011-760 (2011), ATLAS Internal, http://cdsweb.cern.ch/record/1361631.

[5] The ATLAS Collaboration, arXiv:hep-ex/1108.1582 (2011).

[6] The ATLAS Collaboration, ATL-CONF-2011-760, (2011), http://cdsweb.cern.ch/record/1383787.

[7] Martin A., Stirling W., Thorne R., and Watt G., Euro. Phys. J. **63** (2009) 189–285.

[8] LEPP Electroweak Working Group, Phys. Lett. B **565** (2003) 61 – 75.

[9] The CDF Collaboration, Phys. Rev. Lett. **95** (2005) 252001.

[10] The D0 Collaboration, Phys. Rev. Lett. **104** (2010) 061801.

[11] The CDF Collaboration, Phys. Rev. Lett. **104** (2010) 111802.

[12] The ATLAS Collaboration, ATLAS-CONF-2011-011 (2011), http://cdsweb.cern.ch/record/1334563.

[13] Campbell, J.M., Huston, J.W., and Stirling, W. J., Rep. Pro. Phys. **70** (2007) 89.

[14] ATLAS Collaboration, Detector and Physics Performance Technical Design Report, CERN-LHCC/99-14, 1999.

[15] ATLAS Muon Collaboration, ATLAS Muon Technical Design ReportCERN/LHCC/97-22., CERN/LHCC/97-22, 1997.

[16] Dai T., *Private Correspondence.*

[17] van Kesteren, Z., PhD Thesis Amsterdam U. oai:cds.cern.ch:1255858 (2010).

[18] The ATLAS Collaboration, arXiv:hep-ph/1109.0525 (2011).

[19] Gell-Mann, M., Phys. Rev. **125** (1962) 1067–1084.

[20] Ne'eman, Y., Nucl. Phys. **26** (1961) 222 – 229.

[21] Glashow, S.L., Nucl. Phys. **22** (1961) 579–588.

[22] Weinberg, S., Phys. Rev. Lett. **19** (1967) 1264–1266.

[23] Salam, A. and Ward, J. C., Phys. Lett. **13** (1964) 168–171.

[24] Ting, S. *et al.*, Phys. Rev. Lett. **33** (1974) 1404–1406.

[25] Richter, B. *et al.*, Phys. Rev. Lett. **33** (1974) 1406–1408.

[26] Gross, D.J., and Wilczek, F., Phys. Rev. Lett. **30** (1973) 1343–1346.

[27] Politzer, H.D., Phys. Rev. Lett. **30** (1973) 1346–1349.

[28] Arnison, G. *et al.*, Phys. Lett. **B122** (1983) 103–116.

[29] Arnison, G. *et al.*, Phys. Lett. **B126** (1983) 398–410.

[30] Abe, F. et al, Phys. Rev. Lett. **74** (1995) 2626–2631.

[31] Abachi, S. et al, Phys. Rev. Lett. **74** (1995) 2422–2426.

[32] Higgs, P.W., Phys. Rev. Lett. **13** (1964) 508–509.

[33] Pauli W., Z. Physik **31** (1925) 373.

[34] Halzen, F. and Martin, A., "Quarks and Leptons: An introductory course in modern particle physics", (John Wiley and Sons, New York, USA, 1984).

[35] Gell-Mann, M., Phys. Rev. **125** (1962) 1067–1084.

[36] Nambu, Y. and Jona-Lasinio, G., Phys. Rev. **122** (1961) 345–358.

[37] Susskind, L., Phys. Rev. D **20** (1979) 2619–2625.

[38] Dimopoulos, S., and Susskind, L., Nucl. Phys. **B155** (1979) 237–252.

[39] Eichten, E. and Lane, K.D., Phys. Lett. **B90** (1980) 125–130.

[40] Holdom, R., Phys. Rev. D **24** (1981) 1441–1444.

[41] Holdom, R., Phys. Lett. B **150** (1985) 301 – 305.

[42] Appelquist, T., Karabali, D., and Wijewardhana, L. C. R., Phys. Rev. Lett. **57** (1986) 957–960.

[43] Appelquist, T., and Wijewardhana, L. C. R., Phys. Rev. **D36** (1987) 568.

[44] Yamawaki, K., Bando, M., and Matumoto, K., Phys. Rev. Lett. **56** (1986) 1335–1338.

[45] Akiba, T., and Yanagida, T., Phys. Lett. B **169** (1986) 432 – 435.

[46] Hill, C.T., Phys. Lett. B **345** (1995) 483 – 489.

[47] Lane, K.D. and Mrenna, S., Phys. Rev. D **67** (2003) 115011.

[48] Drell, S.D., and Yan, T.M., Phys. Rev. Lett. **25** (1970) 902.

[49] T. Sjostrand, S. Mrenna and P. Skands, JHEP **05** (2006) 026.

[50] The ATLAS Collaboration, Euro. Phys. J. **71** (2011) 1–37.

[51] Budagov, Y.A., *et al.*, ATL-TILECAL-97-127, (ATL-L-PN-127) (1997), http://cdsweb.cern.ch/record/683592.

[52] Yamamoto, A., Nucl. Ins. Meth. **453** (2000) 445 – 454.

[53] Blanchot, G., ATL-ELEC-PUB-2007-002, (ATL-COM-ELEC-2007-003) (2007), http://cdsweb.cern.ch/record/1073170.

[54] Hough, P. and Powell, B., Il Nuo. Cim. **18** (1960) 1184–1191.

[55] Cornelissen, T.G. *et al.*, J. of Phys. **119** (2008) 032013.

[56] Frühwirth, R., Nucl. Ins. Meth. **262** (1987) 444–450.

[57] Bethe, H., Ann. der Phys. **397** (1930) 325–400.

[58] Bethe, H. and Heitler, W., PRSL **146** (1934) pp. 83–112.

[59] Lund, E *et al.*, ATL-SOFT-PUB-2008-003, (ATL-COM-SOFT-2008-008) (2008), http://cdsweb.cern.ch/record/1114577.

[60] Groom, D., Mokhov, N., and Striganov, S., ADNDT **78** (2001) 183 – 356.

[61] Virgil L. and Highland,, Nucl. Ins. Meth. **129** (1975) 497 – 499.

[62] Adams, D.L., Mete, A. S., and Viel, S., ATL-COM-PHYS-2011-1309 (2011), http://cdsweb.cern.ch/record/1385916.

[63] Langacker, P., Rev. Mod. Phys. **81** (2009) 1199–1228.

[64] Erler, J., Langacker, P., Munir, S., and Rojas, E., JHEP **2009** (2009) 017.

[65] London, D., and Rosner, J.L., Phys. Rev. D **34** (1986) 1530–1546.

[66] G. Corcella *et al.*, JHEP **2001** (2001) 010.

[67] Corcella, G.*et al.*, arXiv:hep-ph/0210213 (2002).

[68] Agostinelli, S. *et al.*, Nucl. Ins. Meth. **A506** (2003) 250–303.

[69] The ATLAS Collaboration, Euro. Phys. J. **C70** (2010) 823–874.

[70] Golonka, P. *et al.*, Comput. Phys. Commun. **174** (2006) 818–835.

[71] Golonka, P., and Was, Z., Euro. Phys. J. **C45** (2006) 97–107.

[72] Sherstnev, A. and Thorne, R.S., Euro. Phys. J. **C55** (2008) 553–575.

[73] Frixione, S., and Webber, B.R., JHEP **0206** (2002) 029.

[74] Butterworth, J.M., Forshaw, J.R., and Seymour, M.H., Z. Phys. **C72** (1996) 637–646.

[75] J. Pumplin *et al.*, arXiv:hep-ph/0201195 (2002).

[76] Mangano, Michelangelo L. and Moretti, Mauro and Piccinini, Fulvio and Pittau, Roberto and Polosa, Antonio D., JHEP **07** (2003) 001.

[77] Botje, M. *et al.*, arXiv:hep-ph/1101.0538 (2011).

[78] Hamberg, R. and van Neerven, W.L. and Matsuura, T., Nucl. Phys. **B359** (1991) 343–405.

[79] Blair, R. *et al.*, ATLAS Internal (2010), *"ATLAS Standard Model Cross Section recommendations for* 7 TeV *LHC running"*.

[80] Carloni Calame, C.G., Montagna, G., Nicrosini, O., and Vicini, A., JHEP **10** (2007).

[81] Neyman, J. and Pearson, E. S., RSL **231** (1933) 289–337.

[82] Caldwell, A., Kollar, D., and Kroninger, K., Comput. Phys. Commun. **180** (2009) 2197–2209.